Fall 2021

Quantifying and Elucidating the Effect of CO_2 on AEMFCs

Yiwei Zheng

QUANTIFYING AND ELUCIDATING THE EFFECT OF CO_2 ON AEMFCS

by

Yiwei Zheng

Bachelor of Engineering
Tianjin Polytechnic University, 2014

Master of Science
Israel Institute of Technology - Technion, 2017

Submitted in Partial Fulfillment of the Requirements

For the Degree of Doctor of Philosophy in

Chemical Engineering

College of Engineering and Computing

University of South Carolina

2021

Accepted by:

William E. Mustain, Major Professor

Sirivatch Shimpalee, Committee Member

Chang Liu, Committee Member

Kevin Huang, Committee Member

Melissa Moss, Committee Member

Tracey L. Weldon, Interim Vice Provost and Dean of the Graduate School

ACKNOWLEDGEMENTS

My life during Ph.D. is full of struggles delighted by shades of happiness when the academic achievements become real. I am immersed in my work partially because my anxiety release at working. I am deeply grateful towards Dr. William Mustain. He makes the Ph.D. path less worried, as he always try his best to create a pleasant environment for research. He is always there helping, advising and supporting students. I appreciate his big pictured mind, critical eye and deep brain. He is the most important role in my success except myself.

Next, I want to thank my Committee members Kevin Huang, Chang Liu and Sirivatch Shimpalee for their continuous support, critical thinking, and guidance along this journey. And finally, I have to give a special thanks to all my friends and colleagues that were monumental in my success (Travis Omasta, Xiong Peng, Ehsan Faegh, Benjamin Ng, Xinyi Zhao, Hori Adabi Firouzjaie, Noor Ul Hassan, Lyzmarie Colon, Hanna Soucie, Saheed Lateef, Golareh Jalilvand).

Lastly, I would thank my parents who support me in every aspects.

ABSTRACT

Anion exchange membrane fuel cells (AEMFCs) have recently received significant attention as a future high efficiency, environmentally friendly energy conversion device. This attention is due to the potential advantages that AEMFCs can offer compared the much more common, and commercialized, proton exchange membrane fuel cells (PEMFCs) – most notably lower cost. However, there are several remaining roadblocks for the AEMFC technology to be widely adopted, such as: i) the stability of the anion exchange membranes (AEMs) and anion exchange ionomer (AEIs); ii) the development of highly active catalysts with either low platinum group metal (PGM) loading or catalysts that are completely PGM-free; iii) the discovery of water management strategies to prevent electrodes from flooding or drying out; and iv) reducing the negative effect of CO_2 on performance.

This last issue, CO_2 poisoning in AEMFCs, is considered by many to be the most serious hurdle to overcome. In an AEMFC operating on ambient air, CO_2 reacts with the OH^- anions created from the oxygen reduction reaction at the cathode, forming HCO_3^- and CO_3^{2-}. These carbonates are transported from the cathode to the anode during operation. As shown in Chapter 1 of this thesis, the presence of carbonate anions has multiple impacts on the operating AEMFC; carbonates decrease the conductivity and water uptake of AEM, introduce additional charge transfer resistance at the hydrogen oxidation anode and change the anode pH (resulting in a thermodynamic decrease in the cell operating voltage). In

total, the CO_2-related overpotential can be up to 400 mV, which is unacceptable from a practical perspective.

This work will present an extensive array of experiments that deconvolutes the fundamental electrochemical mechanism for carbonate "poisoning" in AEMFCs. The dynamics of CO_2 uptake and removal and dynamics in these systems – with a particular focus on the impact of CO_2 concentration in the reacting gas, gas flowrates, backpressure, fuel cell hydration level and temperature, AEM thickness and AEM chemistry, which are the focus of Chapters 2 - 4. With this new understanding strategies to reduce the CO_2 related overpotential below 100 mV will be shown. Finally, as shown in Chapter 5, the chemical mechanisms for how carbonation leads to voltage loss in operating AEMFCs have even been used to design systems that minimize the exposure of operating AEMFCs to CO_2. Such a device can be called an anion exchange CO_2 separator (AECS) which i) is able to generate power; and ii) takes advantage of the carbonation phenomena that harms AEMFCs. In this work, the effectiveness of an AECS in lowering the CO_2 concentration of an incoming stream of 400ppm air is investigated. In addition to showing significant CO_2 removal, an AECS that operates with a stable output for over 150 h is shown. AEMFC operation on AECS-purified industrial air is successfully demonstrated.

Chapters 6 is a summary of all the fundamental findings in this work. Lastly, Chapter 7 of this thesis is meant to provide some perspective on the state of the technology and where it is going. It also proposes future work that can be done to achieve a AEMFCs with high CO_2 resistance in the near future.

TABLE OF CONTENTS

LIST OF TABLES

LIST OF FIGURES

LIST OF SYMBOLS

i_o	Exchange current density
α	Effective transfer coefficient
F	Faraday's constant
R	Ideal gas constant
E	Electrode potential
$E^{o'}$	Formal potential
i	Total current
i_c	Component of the total charge carried by CO_3^{2-}
P_i	Partial pressure of each gas
ε	Average charge per CO_2
n	Number of electrons transferred in the ORR
K_{b2}	Equilibrium constant

LIST OF ABBREVIATION

AEI……..……..……..Anion Exchange Ionomer

AEM …….…….....…..…Anion Exchange Membrane

AEMFC…….Anion Exchange Membrane Fuel Cell

AFC…….…….……...…….……Alkaline Fuel Cell

ASR…….....……Area-Specific Resistance

DOC.....…...Degree of Carbonation

ETFE-BTMA…….……Ethylene Tetrafluoroethylene-Benzyltrimethylammonium

GDE……...……...……..Gas Diffusion Electrode

HOR……...…….…….……..Hydrogen Oxidation Reaction

LDPE…….....…….…….……Low Density Polyethylene

MEA….....…….……...…….Membrane Electrode Assembly

OCV…..…….…...……Open-Circuit Voltage

ORR……...…….……Oxygen Reduction Reaction

PEM……..…..…….…… Proton Exchange Membrane

PEMFC……...…..…… Proton Exchange Membrane Fuel Cell

RH……...…….…….….. Relative Humidity

CHAPTER 1: INTRODUCTION TO ANION EXCHANGE MEMBRANE FUEL CELLS

Proton-exchange membrane fuel cells (PEMFCs), illustrated in Figure 1.1a, have long been considered to be a promising technology for clean and efficient power generation in the twenty-first century. The proton exchange membrane (PEM) is the key component in this fuel cell system. The PEM in the PEMFC is typically a sulfonic acid functionalized, perfluorinated, Teflon-like film that is used to conduct protons between two porous electrodes. Researchers have aimed to prepare PEMs with high proton conductivity, low electronic conductivity, low fuel permeability, low electroosmotic drag coefficient, good chemical/thermal stability, good mechanical properties and low cost. The operating temperature of PEMFCs are typically around 90 °C. The low operating temperature makes the technology competitive in transportation and commercial applications.[1]

Nafion^{TM}, which is a typical PEM, has a structure of a copolymer that consists of a Teflon backbone, which gives the backbone a hydrophobic character, and sulfonic acid groups (HSO_3^-) grafted into backbone, which give the head groups a hydrophilic character. These two tend to phase separate and the hydrophilic domains provide the ability for the membrane to be ionically conductive and uptake the water needed to hydrate the polymer.

For decades, the PEMFC has dominated the research space for low temperature polymer electrolyte fuel cells. The advantages of the PEMFC are its higher power density and quick start up for automotive vehicles. Though significant advances have been made regarding the performance and stability of PEMFCs over the years, the major drawback

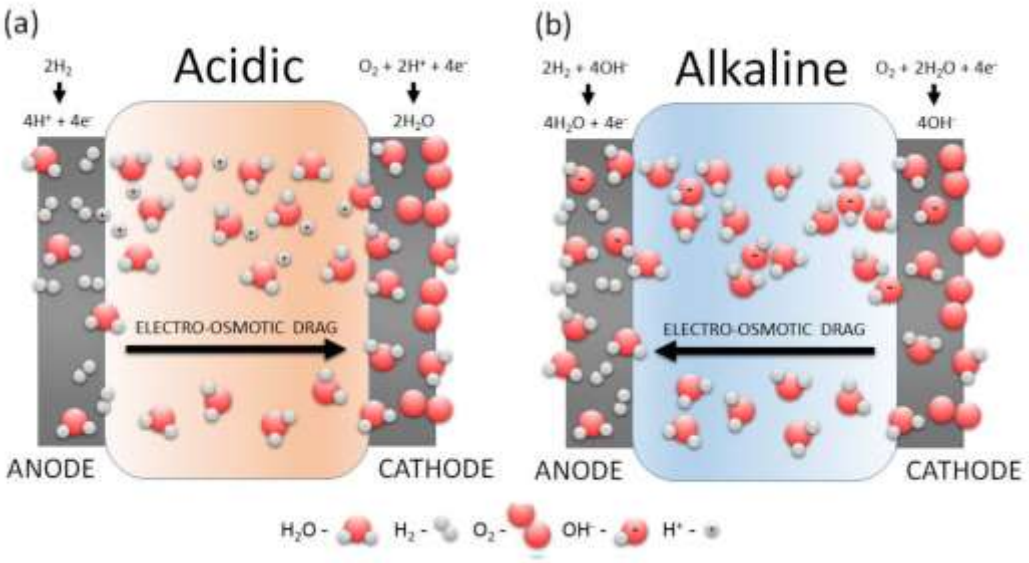

Figure 1.1 Operating principles for (a) acidic fuel cell (PEMFC) and (b) alkaline fuel cell (AEMFC) showing reactions, as well as ion and water movement. [2]

of the PEMFC is its high cost. Two of the drivers of the high cost are the membranes and the use of expensive platinum catalysts[3], as shown in Figure 1.2, where experts believe that high Pt group metal loading is the most significant barrier to reducing cost. A lot of research and development funding has been allocated to "catalysts and electrodes," followed in decreasing amount by "fuel cell performance and durability".[4]

It has been broadly suggested in recent years that a change of electrolyte to a solid alkaline polymer electrolyte might be able to significantly reduce the cost of polymer-based fuel cell systems [5] because the alkaline environment would allow for the deployment of a broader range of noble metal free catalysts as well as less expensive materials to be used for other cell components such as the membrane and bipolar plates.

Therefore, alkaline fuel cells (AFCs), which were very popular in the early-to-mid 20th century, have some advantages over the more modern PEMFCs. AFCs operate between 200 °C – 240 °C to improve the ionic conductivity of the electrolyte as well as the electrode kinetics. The fast kinetics and high electrical efficiency allows the use of a lower quantity of a noble metal catalyst or non-noble metal electro-catalysts like nickel, silver, etc.[6] Most importantly, the liquid KOH electrolyte used in the AFC is much cheaper than the polymer electrolyte commonly used in PEMFC, which needs an appropriate hydration level for good performance and proper functioning. That is to say, water management is not a major issue for AFCs as liquid electrolyte was used, thus allowing simple design and fabrication. Therefore, considering the cost and the simplicity of operation, AFCs are advantageous over other types of fuel cells and promising on the commercialization of fuel cells. AFC Energy (located in Surrey, UK) is a producer of alkaline fuel cells which has developed a scalable AFC system.

	Ranking (from list)		
	1st	2nd	3rd
Cost of Pt due to high PGM total loading	26	4	2
Cost of BPPs	4	7	12
Cost of membrane	1	14	8
Cost of air compression system	1	7	3
Cost of GDLs	1	3	5
Cost of heat exchangers	1		1
Cost of cathode humidifier		1	2

Figure 1.2 Experts' rankings of barriers to reducing automotive PEMFC system cost. The number of experts who selected each barrier is indicated (darker cells indicate more experts). The barriers shown were selected from a list.[4]

AFCs operating with H_2/air have better prospects than PEMFCS for developing the lowest cost devices. Unfortunately, AFCs have a significant fundamental problem: the aqueous KOH electrolyte reacts with CO_2 from ambient air to form carbonates,[7–9] which lowers the performance and stability of the fuel cell because: 1) large carbonate crystals, K_2CO_3, precipitate in the electrodes due to their low solubility; and 2) the concentration of OH^- in the electrolyte is reduced. The latter decreases the number of hydroxyl ions available for reaction at the anode, leading to sluggish anode kinetics. Additionally, CO_2 poisoning modifies the composition of the electrolyte and thus reduces its ionic conductivity, increasing the Ohmic polarization and leading to lower cell efficiency. Therefore, strategies have been proposed to solve the CO_2 poisoning problem. Cifrain and Kordesch[10] found that the negative effects of CO_2 poisoning can be partly reduced by circulating the electrolyte. Nowadays, most of the current strategies for solving the CO_2 poisoning issue in AFCs are still in their early stages and inadequate for commercialization.

Anion exchange membranes (AEMs) are gaining popularity for use in alkaline fuel cell technologies to replace traditional AFCs, creating so-called anion exchange membrane fuel cells (AEMFCs). However, there are many challenges to be addressed before AEMs and AEMFCs become mainstream, including performance, stability and mechanical strength.

Generally, AEMs offer several advantages over liquid-based alkaline systems, such as decreased gas crossover, which in operating AEMFCs means a higher open circuit voltage (OCV) and increased efficiency[11]. Additionally, it is thought that AEMs will have better CO_2 tolerance thank KOH as there is no possibility for K_2CO_3 to form and precipitation to occur, even if carbonates are formed during operation. The cations in

AEMFCs are stationary, meaning that the carbonate anions should be freely transported through the AEM when they are formed. Moreover, for AFCs the problem of flooding and "weeping" is also largely avoided due to the solid-state electrolyte.

In AEMFCs, illustrated in Figure 1.1b, hydrogen reacts with hydroxide anions in the electrolyte to create water and electrons (Equation 1.1). The electrons move through the external circuit to cathode where they react with oxygen and water to create the OH^- (Equation 1.2). The latter is supplied through the electrolyte to the anode by migration.

$$2H_2 + 4OH^- \rightarrow 4H_2O + 4e^- \quad (1.1)$$

$$O_2 + 2H_2O + 4e^- \rightarrow 4OH^- \quad (1.2)$$

Researchers have aimed to prepare AEMs with high anion (hydroxide) conductivity, long-term stability in alkaline media at fuel cell operating temperature, robust mechanical properties for overcoming in-use pressure differences, as well as proper water uptake and swelling, which facilitate ion transport within the electrodes and membrane. Early development of AEMFCs was hindered by AEMs with very poor alkaline stability [12] and very poor performance, with typical peak power densities well below 0.5 W cm^{-2}. The combination of low achievable power and limited durability[13,14] made AEMFCs uncompetitive with PEMFCs for years. Another issue with the AEMs in the first years of their development was that their anion conductivities were very low (5–20 mS cm^{-1}) compared to the H^+ conductivity in their PEM counterparts (~100 mS cm^{-1}). In these early days, the resulting AEMFC performance was also low. Varcoe et al.[15] reported the peak power density of ~130 mW cm^{-2} at 50 °C for a cell using a 51-μm thick radiation-grafted poly(ethylene-*co*-tetrafluoroethylene) (ETFE) AEM (conductivity of 27 mS cm^{-1} at 20 °C). Gu et al.[16] reported 260 mW cm^{-2} peak power density for an AEMFC using a

phosphonium-functionalized polysulfone AEM. The improved performance was explained by enhanced mechanical stability allowing the use of backpressure and to operate at 70 °C, and increased conductivity to 46 mS cm^{-1}. Kim et al.[17] obtained 580 mW cm^{-2} peak power density at 80 °C under 30 psig backpressure using a 50-μm thick quaternized poly(phenylene) AEM. PEMFCs typically achieve peak power densities > 2-3 W/cm^2 when operating with O_2 and H_2 reacting gases.

Over the past several years, there has been significant advances with AEMs. There have been several reports of AEMs with hydroxide conductivity of over 100 mS/cm (60°C to 80°C)[18–20] and recent reports of AEMs with conductivity over 200 mS/cm (at 80°C).[21] From these advances, there are several commercially available AEMs for AEMFCs. Commercial products include: Ionomr (Canada - AFN-HNN8-50-X, AFN-HNN8-25-X, etc.), FuMA-Tech (Germany - FAA, FAB, FAD, etc.) and the US companies Xergy (Xion Durion™, Pention™), Orion (Orion™) and Dioxide Materials (Sustainion®). However, even as AEMs were developed with higher conductivities (comparable to or exceeding PEMs), AEMFC performance and durability still remained quite low. This was confusing to the field as each of the individual components of the cell (membrane, catalyst, etc.) now showed very strong ex-situ performance.

What was discovered was that the reason for the lower performance in an operating cell than would be expected from the component-level properties was poor control over water in the cell and electrodes. Therefore, Omasta et al. [22] has focused on improving operational protocols including controlling temperature, pressure, reacting gas dew points, etc. to manipulate the cell-level water dynamics. They have also focused on component fabrication techniques, most notably tight control over the ionomer:carbon:catalyst

loading[23,24] and hydrophilicity/hydrophobicity of the anode and cathode electrodes. This allowed them to routinely achieve high AEMFC performance (> 2 W/cm^2 peak power densities) and long life (> 1000 h with minimal loss in operating voltage at 600 mA/cm^2).[20,21] State-of-the-art AEMFCs even have the ability to achieve peak power densities over 3 W cm^{-2} operating on H_2/O_2 gas feeds[20]. Huang et.al reported AEMs consisting of composite poly(norbornene) with record high hydroxide conductivity, 198 mS/cm, and very high peak power density in a hydrogen/oxygen fuel cell, 3.4 W/cm^2 at 80°C.[21]

Also, the performance stability of AEMFCs has improved dramatically during this time, with multiple groups reporting 500+ hour stability at low degradation rates (5 – 10%)[23,25–27]. Few long-term (>1000 h) AEMFC degradation rates have been reported. A half-cell (ORR) AEMFC was utilized to measure the stability of commercial 40 wt% Pt/C, where a degradation rate of 29 μV/h was reported after 1500 h at 0.31V_{SHE}[28]. Ul Hassan[29] showed an AEMFC utilizing a PNB-type AEM operated for 2000 h with a very small voltage loss where the AEMFC degradation rate is almost half of that measured in 2011 (employing Tokuyama materials) [30], 15 μV/hr.

More facile kinetics of the oxygen reduction reaction (ORR) in alkaline media than in acidic media allows the replacement of expensive and scarce Pt-based electrocatalyst in AEMFC with a class of non-precious metal including transition metal oxides. Peng et al. reported that nitrogen-doped carbon–CoO_x has high intrinsic activity and achieved 1.05 W cm^{-2} peak power density used as AEMFC cathode. The N-C-CoO_x cathode even showed good stability over 100 hours of operation with a voltage decay of only 15 % at 600 mA cm^{-2} under H_2/air (CO_2-free) reacting gas feeds.[31]

Now that AEMFC performance and stability has been enhanced to the point where their future deployment in real applications can be seriously contemplated, it is now an important time in AEMFC development to begin to answer some of the other lingering issues that have to date been mostly put aside in the literature, such as operating on real air, which contains CO_2. Though AEMs are able to freely transport carbonates, and do avoid the salting that plagued AFCs, it is unknown to what the extent carbonation might occur in operating cells or if carbonation will lead to performance losses.

When CO_2-containing air is fed to the AEMFC cathode, the OH^- anions that are produced from ORR, Equation 1.2, react with CO_2 to produce carbonate and/or bicarbonate anions, Equations 1.3-1.4.

$$CO_2 + OH^- \rightleftharpoons HCO_3^- \quad (1.3)$$

$$HCO_3^- + OH^- \rightleftharpoons CO_3^{2-} + H_2O \quad (1.4)$$

As (bi)carbonate anions are produced, they are transported towards the anode by migration, resulting in a "carbonation" of the AEM and the ionomer in the electrodes (especially the anode). The presence of carbonate anions decreases the conductivity of the AEM and therefore the AEMFC performance. It is because they have a larger ionic radius than that of OH^-, and therefore, have lower diffusion coefficients and lower mobility. In aqueous solutions, OH^-, CO_3^{2-} and HCO_3^- have ionic mobilities of 20.64, 7.46, and 4.61 $*10^8$ $m^2s^{-1}V^{-1}$ respectively.[32] Though, the ratio between diffusion coefficients of different anions in AEM should be the same as the ratio between their mobilities (directly proportional to each other), there may be some deviations from their values in aqueous media due to the chemical interactions between ions and the polymer framework, such as ions associating with the cationic moieties in the AEM, morphological arrangement at the

water-involved regions. For example, Amel et al. [33] found that the diffusion coefficient of HCO_3^- in an AEM is 90 % lower than that of its value in an aqueous solution.

There are several mechanisms for transporting anions through the membrane, including diffusion, migration, convection and the Grotthuss hopping mechanism.[34] The Grotthuss hopping mechanism only works for OH^- (not HCO_3^- and CO_3^{2-}), and involves the breaking and forming of O−H bonds in the water molecules, rather than physical movement of the anions.[35] The mechanisms available for HCO_3^- and CO_3^{2-} are diffusion, migration and convection, which are dependent on the size and charge of the anion. Therefore, OH^- conductivity is significantly higher HCO_3^- and CO_3^{2-}.

The AEM conductivity with different anions is not dependent on their ionic radius alone, but also on the number of hydration layers. The hydration layer is different for each anion and depends on the surface charge density of the anion. With large ionic charge and small ionic radius, the surface charge density is increased, resulting in the growth of hydration shell and the decreasing of ion mobility. The number of water molecules present in the hydration shell is around 4 for OH^-, 7 for HCO_3^- and 9 for CO_3^{2-}.[34,36] Therefore, HCO_3^- is most likely the biggest contributor to the decrease in AEM conductivity because it has the highest hydration radius and carries a charge of only −1 – as opposed to CO_3^{2-} which is divalent. A mathematical model of the carbonation process developed by Kiss et al.[37] found that CO_3^{2-} contributes the most to the conductivity of the AEM with mixed anions because it has the highest concentration in the membrane and carries more charge.

Another aspect of the effect of HCO_3^-/CO_3^{2-} anions on the effective conductivity of the AEM is the dissociation equilibrium of anions and fixed cationic groups on the AEM. A higher degree of dissociation results in a greater number of ions that are free to serve as

charge carriers through the membrane. In an AEM with OH^- form, about 32 % of the OH^- anions are freely present in the membrane[38,39], whereas in a mixed-form AEM roughly 40 % of OH^- and HCO_3^- anions are dissociated from the cationic groups and only 20 % of CO_3^{2-}.[33,40,41]

In addition to increasing the ionic conductivity, there are two other mechanisms by which carbonates affect the performance of AEMFCs. Though these mechanisms will be more completely discussed in the next chapter, they are summarized here. Both mechanisms are caused by the fact that the (bi)carbonate anions are not able to directly oxidize H_2 in the anode at typical AEMFC anode potentials. This means that the carbonates formed at the cathode are not consumed at the anode by the reaction; hence, they are not immediately released to the anode exhaust. Instead, what happens is that there is a time lag between CO_2 exposure and CO_2 release. During this time lag, the carbonates accumulate at the anode, causing the pH of that electrode to drop[42–44]. As the pH drops and carbonates are accumulated, the decarbonation process eventually occurs. The drop in the anode pH results in a Nerstian increase in the anode potential, reducing the overall cell voltage. The pH gradient reduces the cell voltage, approximated as 70 mV per pH unit over most of the pH range.[45] Therefore, this thermodynamic effect from carbonation can result in a severe reduction in the operating cell voltage [42].The other mechanism related to the inability of (bi)carbonates to react directly with H_2. The anode has a given IEC; therefore, the accumulation of carbonates creates a concentration gradient in the anode, and there are low OH^- concentrations near anode catalyst layer. Combined with the fact that OH^- is no longer the sole charge carrier – (bi)carbonates carry charges as well, the reacting OH^- anions need to be supplied through both migration and diffusion for anode reaction. This forces the

anode current density to be concentrated close to the anode/AEM interface, increasing the effective local current density of the anode and forcing higher reaction overpotentials.

Though it is known that carbonation and its effect on AEMFC performance is very important, unfortunately, there have been few experimental studies to date on AEMFC carbonation. Suzuki et al.[46] found that the flux of CO_2 in the anode exhaust of AEMFCs increased with CO_2 concentration in the cathode and with cell current density. They found that the increasing of Ohmic resistance was noticeable by the supply of CO_2 to the cathode but not obvious when CO_2 was fed to the anode. Watanabe et al.[47] also found that the ion ratio (OH^-, CO_3^{2-} and HCO_3^-) depended on current density. Kimura and Yamazaki [32] measured a decrease in ex-situ conductivity of an AEM exposed to CO_2. Contacting with air containing 38% CO_2 caused the ionic conductivity of AEMs to decrease to 40% of the initial value. Fukuta et al.[48] believed almost all CO_3^{2-} was released at the higher current density by self-purging, and small pH change caused big difference in anode catalytic activity. At high current density, the CO_3^{2-} and HCO_3^- species are expected to be purged through the membrane and released out of the fuel cell in the anode exhaust, the so called 'self-purging' mechanism. However, the extent of self-purging decarbonating FC has not been confirmed experimentally and the carbonation dynamics are poorly understood.

Peng et al.[49], Pandey et al.[50] and Suzuki et al.[46] studied the effect of OH^-, CO_3^{2-} and HCO_3^- anions on water uptake, conductivity and water transport properties of Tokuyama A201 and Fumasep® FAA-3 AEMs where the data were fit to a single exponential decay. Peng et al.[49] measured that the highest conductivity of the OH^- form of a Tokuyama A201 AEM was 0.132 S cm^{-1} at 80 °C, which is about 3–4 times higher than the one in the HCO_3^- form (0.031 S cm^{-1}) and Cl^- form (0.044 S cm^{-1}). In addition, Divekar et al.[51] studied the

carbonation process kinetics in perfluorinated-based AEMs by transient SAXS measurements at 30 °C and 95%RH , they observed that the OH- ion concentration drops within ~15 minutes and then the CO_3^{2-} and HCO_3^- equilibrates over time. The also showed that temperature and CO_2 concentration effect equilibration time as well as the anion composition in the AEM[52]. Researchers have hypothesized that the carbonation of AEMFCs increased the internal resistance and could be self-purged during operation at a current density higher than 1 A/cm^2. However, our group has demonstrated that both of two assertions are not correct[53]. Some of these effects are described below and some are elaborated in later chapters of this thesis. We found that the CO_2 concentration and current density have a significant effect and we quantified the mechanisms that caused CO_2-related voltage loss. During this time, it was found that at the self-purging mechanism is not sufficient to remove all carbonates. Even at a current density of 2.0 A cm^{-2} and 100 ppm CO_2 concentration, the CO_2-related overpotential was significant (167 mV), and the CO_2-related overpotential at 2.0 A cm^{-2} and pseudo-air conditions (400 ppm CO_2) was even higher (259 mV). Even at 5 ppm CO_2, AEMFCs showed a significant loss (30 mV) in operating voltage.[54]

Further, it was proposed to operate AEMFCs at temperatures above 80 °C to avoid the carbonation problem, due to reduced solubility of CO_2 in the membrane as per Henry's law[55]. However, it was found [53] that carbonation is still significant at 80 °C. Later,[54] it was found that reducing the cathode flow reduced the total CO_2-related cell voltage loss and that increasing cell hydration improved cell performance in the presence of CO_2. The effect of AEM chemistry on AEMFC carbonation is studied with selected different AEMs[56]. They found that thicker AEM would cause lower FC voltage loss due to the carbonation and

lower conductivity of AEM is preferred for CO_2-resistant AEMFC. The significantly reduced water content and distribution in an operating AEMFC under CO_2 exposure were studied and presented through Neutron imaging as well.

The strategy of reducing the CO_2 concentrations in AEMFCs is important. Several years ago, CellEra/Elbit Inc, added a regenerative CO_2 filter before the air inlet to reduce the CO_2 concentration from 400 ppm to <5 ppm.[57] However, they found that the additional balance of plant costs to scrub CO_2 could was likely an insurmountable obstacle to light-duty transportation use, even given the generous assumptions on materials cost savings (catalyst, bipolar plates, etc.). Zheng et al.[54] also proposed the possibility of using AEM fuel cells as simultaneous power generators and CO_2 separators due to this pumping effect. Matz et al. demonstrated the ability of an electrochemically-driven CO_2 separator which can be used to remove ambient levels of CO_2 from air upstream for AEMFC, protecting it from CO_2-related performance losses. It could remove CO_2 down to single digit ppm levels at moderate current densities and low anode flow rates. The influence of anode flows, cathode flows, and current density on CO_2 removal performance was investigated. A carbon-ionomer interlayer was introduced at the cathode to improve CO_2 capture. Most importantly, the current optimal CO_2 separator design was able to remove 98% of CO_2 for 100 h at 2.7% of the hydrogen stack demand. Muroyama et al.[58] presented the cell-level dynamics of an AEM-based CO_2 separation process with associated technoeconomic considerations. High faradaic efficiencies, owing to pure HCO_3^- transport, could be reached when high (≥15%) CO_2 concentrations are used.

Because of the limited published experimental work on carbonation, the field has mostly relied on modeling approaches (most often not experimentally validated) to shed light on this phenomena. Most of these models have typically focused on ex-situ/non-operational AEMs, making it hard to fully understand the carbonation and purging processes for an operating AEMFC. Some of the most widely cited models in this area are discussed below.

Grew et al.[59] developed a Dusty Fluid model to account for the morphological properties of AEMs in pure OH^- form, which they then extended to consider the effects of temperature and CO_2 on AEM conductivity. Kiss et al.[37] developed a mathematical model for ion transport in AEMs and calculated that the ion-membrane diffusion coefficient of OH^- was up to 1.3 times higher than that of the CO_3^{2-} coefficient and 1.5 times higher than that of HCO_3^-.

A comprehensive description of HCO_3^- and CO_3^{2-} formation in an ex-situ AEM exposed to CO_2 was presented by Myles et al.[60] through an ion exchange model. They modelled the concentration profile of all of the anionic species for both Tokuyama A201 and radiation-grafted ETFE AEMs. The authors suggested that the drop in conductivity occurs for two reasons: hydroxide depletion and carbonate–bicarbonate exchange. It can be noticed that the A201 approaches equilibrium in ~30 min whereas the ETFE takes ~50 min. The different times are attributed to the difference in the hydration, morphology and chemical composition of the polymers.

The theoretical models listed above describe the behavior of isolated AEMs in the absence of polarization and electrochemical reactions. The polarization induced by the electrodes provides an extra driving force for transport across the membrane, while the

Faradaic ORR and hydrogen oxidation reaction (HOR) reduce and oxidize ions at the membrane boundaries. These reactions affect the concentrations of ionic species inside the membrane. Therefore, it is important to model the entire the AEMFC, not just the AEM to fully describe the carbonation behavior of these cells.

Theoretical studies on the carbonation of an operating AEMFC have been presented with varying degrees of simplification. Siroma et al.[61] developed a transport model that assumes that only OH^- & CO_3^{2-} or HCO_3^- & CO_3^{2-} ions can exist in the membrane at one time for steady state operation. Their model also prescribes that the flux of HCO_3^- and CO_3^{2-} through the membrane is negligible (zero), and that the OH^- concentration is fixed at zero at the anode. Under these assumptions they were able to predict the carbonate ion ratios of their operating fuel cell, although it was suggested that the two-ion assumption limited the accuracy and predictive capabilities of the model.

Shiau et al.[62] found that as the current increases, the flux of CO_2 from the anode outlet increases, which means that less CO_2 might be accumulated in the AEM; suggesting that carbonate buildup will be minimized as the current density is increased. If taken to the extreme, their results suggest that at high enough current, there would be very few carbonates in the cell. This purging effect has become known as the self-purging mechanism. However, detailed validation was not presented. Also, the association/dissociation reactions with fixed cationic groups were not considered.

Krewer et al.[43] developed a carbonation model for an operating AEMFC that investigated species transport and reactions through several AEMFC components, including flow channels, gas diffusion layers (GDLs), catalyst layers (CLs) and AEM. They failed to consider the difference between chemical and electrochemical purging

models, even the fact that in both cases identical amounts of carbon dioxide and electrons would be produced at the anode. The ionic species fluxes in their model have a type of outflow boundary condition, in which any species reaching the anode/membrane interface are immediately consumed. This somewhat akin to the electrochemical mechanism, but does not account for varying reaction rates due to kinetics and concentration effects, which can result in both local consumption and accumulation. This means that their model incorrectly predicts that the self-purging mechanism can eliminate essentially all carbonate at a current density of only 1.0 A/cm^2.

In summary, none of the models mentioned above truly captured the real behavior inside of AEMFCs. It is necessary to employ the correct mechanism in order to predict accurate electrode potentials and cell voltages. In this regard, Gerhardt et al.[44] used a so-called 1+2D model to demonstrate downstream effects of humidification and carbon dioxide contamination in AEMFCs as both are expected to change under normal flowrates. To make the 1+2D model more realistic, under realistic stoichiometric flow conditions and air input they used a 2D cross-sectional model of an AEMFC which is computed iteratively with updated boundary conditions to simulate sweeping along a flow channel. It could approximate a 3D simulation of a large-scale AEMFC, while preventing the problem from becoming too complex or computationally demanding. This allowed them to demonstrate how increasing the gas pressure at the boundary between the channel and GDL in the 2D model can approximate the effects of 3D mass transport at the bends in a serpentine flow field. The result was that their model was able to capture all three major mechanisms in operating AEMFCs. Their model is able to predict losses for operation cells that are on

par with experimental results. It also does not lead to the false prediction that self-purging occurs and that CO_2 will inevitably have a limited effect on operating AEMFCs.

The literature work discussed above suggests that there are many parameters that will affect the carbonation of AEMFCs and influence their behavior during operation. These include: current density, CO_2 concentration, temperature, flow rate, reacting gas dew points, etc. Though theoretical studies have tried to shed some light on this phenomena[43,63], unfortunately, essentially all of these models have not been validated by any experimental work or none that show the dynamics of carbonation. This is likely because there exists a very small body of experimental work in the literature quantifying the impact of CO_2 and determining the root causes behind the extensive performance drop for AEMFCs when CO_2 is present. These will be further elaborated upon in Chapter 2.

CHAPTER 2: QUANTIFYING AND ELUCIDATING THE EFFECT OF CO_2 ON THE THERMODYNAMICS, KINETICS AND CHARGE TRANSPORT OF AEMFCS

As discussed in Chapter 1, a characteristic of AEMFCs is their susceptibility to poisoning by ambient atmospheric CO_2, which has been widely shown to decrease performance, though possibly improve chemical stability as carbonates are weaker nucleophiles than hydroxide. In the early days of AEMFC research, it was thought that operating cells would be mostly unaffected by the presence of CO_2, other than the reduced mobility of those anions compared to hydroxide, which would increase the Ohmic losses in the cell[43].

Much work has been devoted to exploring the primary mechanisms for the voltage loss caused by CO_2 poisoning. The first mechanism indeed is related to the mobility of the carbonates. As stated above, Ohmic resistance will be increased as the mobilities of (bi)carbonate are lower than OH^-. The second mechanism is caused by the fact that the (bi)carbonate anions are not able to directly oxidize H_2 in the anode at typical AEMFC anode potentials. This means that the carbonates formed at the cathode are not consumed at the anode by the reaction; hence, they are not immediately released to the anode exhaust. Instead, what happens is that there is a time lag between CO_2 exposure and CO_2 release. During this time lag, the carbonates accumulate at the anode, causing the pH of that electrode to drop[42–44]. As the pH drops and carbonates are accumulated, the

decarbonation process eventually occurs. The drop in the anode pH results in a Nerstian increase in the anode potential, reducing the overall cell voltage. The third mechanism is also related to the inability of (bi)carbonates to react directly with H_2. The anode has a given IEC; therefore, the accumulation of carbonates creates a concentration gradient in the anode, and there are low OH^- concentrations near anode catalyst layer. Combined with the fact that OH^- is no longer the sole charge carrier – (bi)carbonates carry charges as well, the reacting OH^- anions need to be supplied through both migration and diffusion for anode reaction. This forces the anode current density to be concentrated close to the anode/AEM interface, increasing the effective local current density of the anode and forcing higher reaction overpotentials.

Therefore, the purpose of this Chapter is to establish a resolute understanding of the influence of CO_2 on the performance of AEMFCs. Herein, the CO_2 concentration in both the cathode and anode are parametrically changed over a wide range of conditions (current density and temperature) that represent reasonable ranges for their practical operation. An extensive collection of carbonation data as a function of current density and CO_2 concentration at the cathode is presented. The level of carbonation is linked to electrochemical performance. Then, this work explores the lower limits of CO_2 exposure to determine whether or not there is a baseline CO_2 tolerance in AEMFCs, which informs the field to what degree oxidant gas scrubbing might be needed. Finally, CO_2 is fed to the anode to simulate fuel impurities or the use of organic fuels. Subsequently, the effect of flowrates and hydration level on carbonation in AEMFC were studied. Finally, the application of AEMFCs operating with carbon dioxide in cathode feed is discussed.

2.1 EXPERIMENTAL

2.1.1 ELECTRODE PREPARATION

The electrodes in this work were prepared using a method that has been detailed in previous publications [23,24]. Briefly, the anode and cathode catalysts were 60 wt% PtRu supported on Vulcan XC-72R (Alfa Aesar HiSPEC 10000, 2:1 ratio of Pt:Ru by mass – Pt nominally 40 wt%, and Ru, nominally 20 wt%) and 40 wt% Pt supported on Vulcan XC-72R (Alfa Aesar HiSPEC 4000, Pt nominally 40 wt%), respectively. Electrode preparation was initiated by placing an ethylene tetrafluoroethylene (ETFE) benzyltrimethylammonium (BTMA) solid powder anion exchange ionomer (AEI, ion-exchange capacity IEC = 1.24 mmol g^{-1}) [64] into a mortar and grinding it with a pestle by hand for 10 min. The catalyst powder, additional Vulcan carbon (XC-72R, Cabot), and 1 mL of Millipore deionized (DI, Type 1 18.2 MΩ cm resistivity) water were added to the mortar and ground for 10 min. The mass fraction of AEI in the catalyst layer was always 0.20 and the mass fraction of carbon was maintained at 0.48 for both electrodes. Next, the catalyst-AEI slurry was transferred to a centrifuge tube. Isopropyl alcohol was added, and the mixture was sonicated (Fisher Scientific FS30H) for 60 min. The water in the ultrasonic bath was maintained below 5 °C to avoid degrading the supported catalyst and the AEI and to maximize the electrochemically active area by avoiding agglomeration. The ink dispersions were sprayed onto Toray TGP-H-0600 gas diffusion layers with 5% PTFE wetproofing with an Iwata Eclipse HP-CS (feed gas was 15 psig Ultra High Purity N_2) to create gas diffusion electrodes (GDEs). The target catalyst loading on the GDEs was 0.6 ± 0.1 mg_{Pt} cm^{-2}.

2.1.2 AEMFC ASSEMBLY AND BREAK-IN PROCEDURE

Before cell assembly, the GDEs were soaked in 1 M aqueous KOH solutions (made from Fisher Chemical pellets/certified ACS and DI water) for 60 min, exchanging the solution twice during this time. At the same time, the AEM was also soaked in an identical solution. Two different AEMs were used in this work. The first was a 50 μm thick (fully swollen in water) ETFE-BTMA-based radiation-grafted AEM [65], which was used for the CO_2 dosing experiments at 60 °C. The second AEM was a 25 μm thick LDPE-(low density polyethylene)-BTMA-based radiation-grafted AEM [66]. The LDPE-BTMA AEM is more chemically and mechanically stable at elevated temperatures than its ETFE-BTMA counterpart and was used when investigating the influence of elevated temperature on CO_2-related overpotential losses.

After soaking for 1 h, excess KOH was removed from the GDEs and AEMs before cell assembly. The GDEs and AEMs were pressed together in the cell to form the MEA with no prior hot pressing. The MEAs were loaded into 5 cm^2 Scribner hardware between two single pass serpentine flow graphite plates. An 850e Scribner Fuel Cell Test Station was used to control the gas stream dew points, cell temperature, gas flowrates and the operating current density.

Before CO_2 measurements were made, all cells underwent a break-in procedure. First, the cell was brought to its operating temperature under N_2 flow on both sides of the cell at 100% relative humidity (RH). Then, the feed gases were switched to Ultra High Purity H_2 and O_2 (Airgas) at the anode and cathode, respectively. Then, the cell was operated chronoamperometrically stepwise from 0.7 V to 0.3 V (0.1 V steps, held for a minimum of 30 min at each step) as the reacting gas dew points were optimized per the standard

procedure [23]. The optimized reacting gas dew points were very repeatable from cell-to-cell, typically 52°C at the anode and 54°C at the cathode for an AEMFC operating at 60°C. Following the optimization of the reacting gas dew points, the cells were operated galvanostatically at the current density of interest (0.2, 0.5, 1.0 or 2.0 A cm^{-2}) and allowed to equilibrate for at least 30 min before CO_2 exposure was initiated. Multiple cells (no less than three) were constructed and tested for each measurement.

2.1.3 AEMFC CARBON DIOXIDE MEASUREMENTS

Following the break-in procedure and 30 min equilibration, the cell current was held constant and CO_2 was parametrically added to the Ultra High Purity O_2 cathode stream. CO_2 was added to O_2 instead of air in order to simplify observations and isolate the effects of CO_2 on performance, since air has additional O_2 mass transport impact (*e.g.* N_2 dilution) during cell operation, which is largely eliminated by utilizing O_2 as the reacting gas. The flowrate for O_2 and H_2 in all experiments was 1 L min^{-1}. CO_2 cathode concentrations as low as 2 ppm and as high as 3200 ppm were tested. Typically, after CO_2 addition the cell was operated for 30 min, which was much longer than the time required to reach quasi-steady-state operation (typically < 5 min, though lower CO_2 concentrations took longer to reach steady-state). After 30 min operation at constant current, CO_2 was removed from the gas stream and the cell was allowed to decarbonate for an initial 30 min. After this, the cell was further decarbonated through self-purging by one of two approaches: i) the cell was allowed to operate at the same current density until the voltage reached its pre-CO_2 level and no CO_2 emission was measured at the anode (shown in Figure 2.1); or ii) more typically, to reduce the time between CO_2 trials, the cell potential was pulsed down to 0.1 V for 1 min (Figure 2.2), after which no CO_2 emission was measured in the anode stream.

When CO_2 was fed to the cathode, the concentration of CO_2 being emitted from the anode and cathode were both constantly monitored in real time using a PP Systems WMA-5 non-dispersive infrared CO_2 gas analyzer (a water trap was placed in-line before the WMA-5 in order to preserve the unit and its calibration).

A second set of experiments were done where CO_2 at concentrations between 2 and 400 ppm was added to the anode instead of the cathode. This was meant to simulate two possible scenarios: i) CO_2 accumulation in the anode; and ii) CO_2 exposure at the anode from the oxidation of carbonaceous fuels (through reforming or direct alcohol oxidation). When CO_2 was fed to the anode, the concentration of CO_2 being emitted from the anode and cathode was constantly monitored in real time using the WMA-5. The cathode data is not shown since CO_2 concentration was always below the detection limit during operation (though a very small amount of CO_2 was observed in the cathode exhaust when the cell current was turned off due to diffusion across the AEM, which is shown).

The third set of experiments investigated the effects of temperature on CO_2-related voltage losses. CO_2 was fed separately to both the cathode and anode at 400 ppm. The cell setup and operation were identical to the previous description with one exception: the AEM used for these temperature studies was LDPE-BTMA (IEC = 2.5 mmol g^{-1}), and not ETFE-BTMA (IEC = 2.05 ± 0.05 mmol g^{-1}), because of its superior thermomechanical stability.

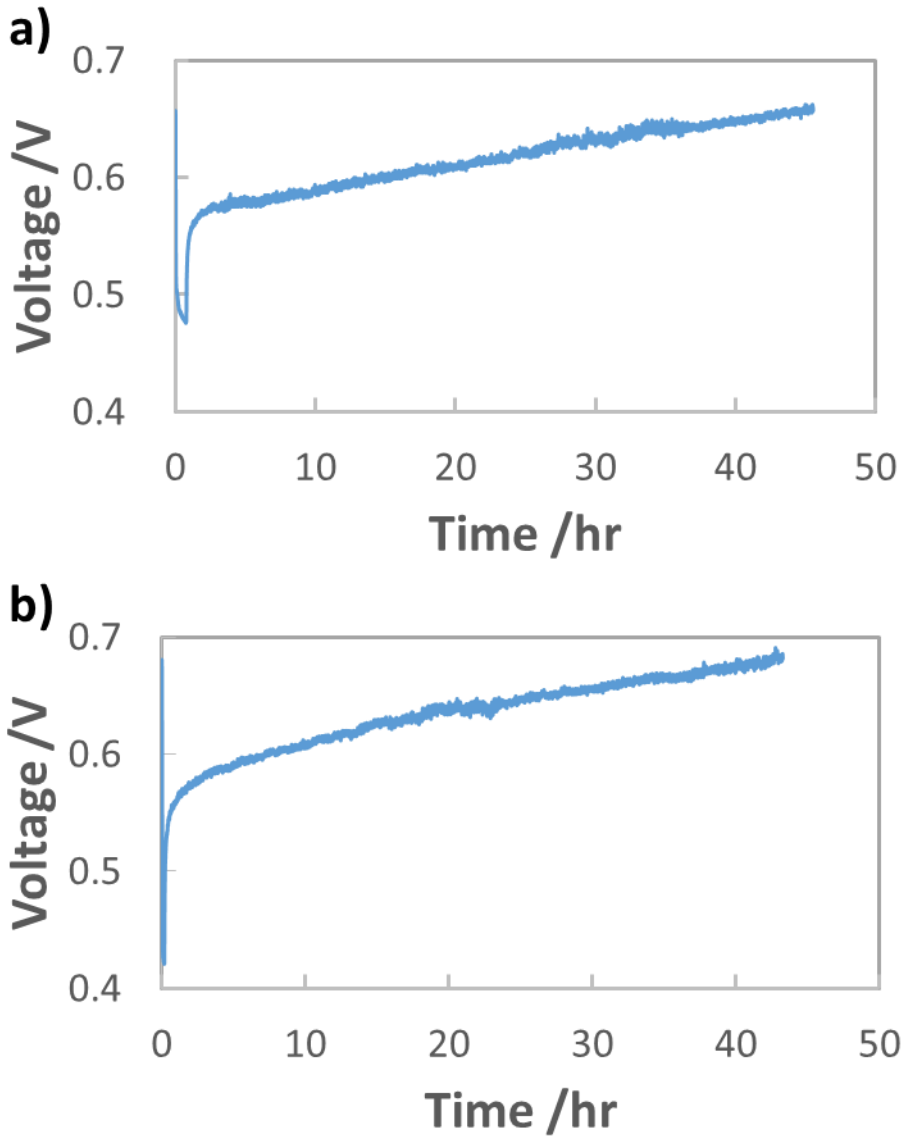

Figure 2.1 Voltage recovery from 400 ppm CO_2 exposure when fed to a) anode b) cathode under constant current operation at 1 A cm^{-2}.

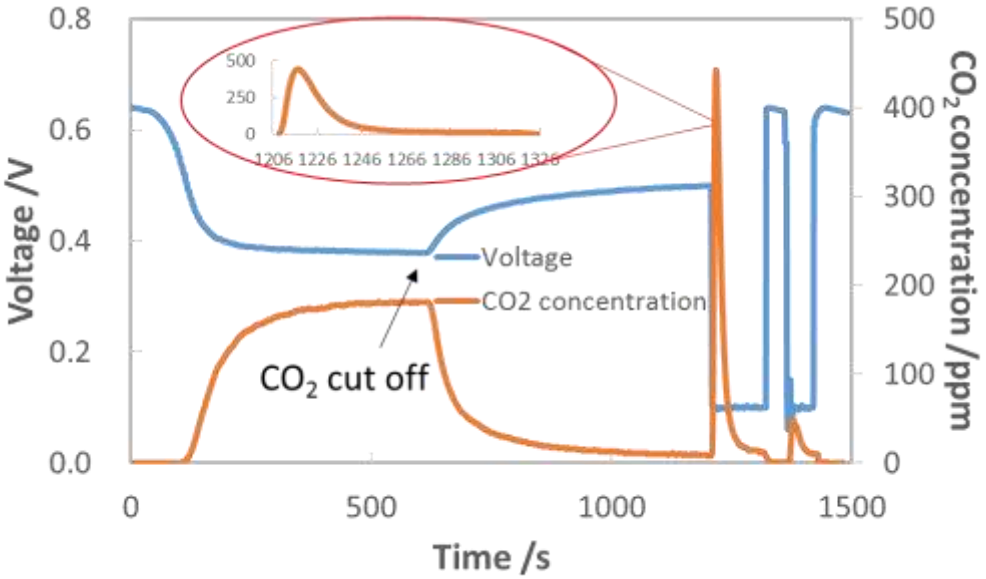

Figure 2.2 Rapid recovery of AEMFC performance through forced decarbonation by pulsing the operating voltage to 0.1V for 2 min. The concentration of the carbonate that was in the AEMFC can be calculated from the measured transient CO_2 concentration in the anode effluent during the pulse (not shown).

2.2 RESULTS AND DISSCUSSION

In a typical analysis of fuel cell performance, it is often assumed that the cell voltage (V_{cell}) can be represented by Equation 2.1:

$$V_{cell} = V_{OCV} - i\left(R_{\Omega,} + R_{ct} + R_{mt}\right) \quad (2.1)$$

where V_{OCV} is the open-circuit voltage, i is the cell current, R_{Ω} is the Ohmic resistance to ion transport, R_{ct} is the charge transfer resistance and R_{mt} is the mass transport resistance. In PEMFCs, it is typically assumed that R_{ct} is dominated by the ORR, but this is likely a poor assumption in AEMFCs where the kinetics for the HOR are slower in alkaline *vs.* acid electrolyte and the HOR overpotential can be significant[67]. Therefore, discussion regarding charge transfer resistance should take into consideration both the ORR and HOR, which can be denoted as R_{ctORR} and R_{ctHOR}, respectively. PEMFCs also assume that R_{mt} is dominated by oxygen diffusion, which is likely to hold in AEMFCs as well (can be denoted as R_{mtORR}), though this can often be neglected with high stoichiometry pure O_2 flows). However, the presence of CO_2 and carbonate anions complicates this type of analysis.

The electrochemical production of hydroxide anions in the presence of CO_2 and their subsequent equilibrium reactions were summarized in Equations 1.2-1.4. It should be noted here that $OH^-/CO_3^{2-}/HCO_3^-$ equilibrium constants exist such that OH^- and HCO_3^- can never exist together in large quantities. However, CO_3^{2-} can exist in high concentrations with either OH^- or HCO_3^-. During cell operation at practical current densities, a significant amount of OH^- is produced and CO_2 is purged from the cell. Therefore, the two ions that dominate under operating conditions are OH^- and CO_3^{2-} , which has been confirmed through theoretical modeling[43]. For this reason, the remainder of the discussion in this work will only consider the presence of "carbonate" as CO_3^{2-}, although it is recognized that

bicarbonate is often present in highly carbonated AEMs and AEMFCs before significant levels of electrochemical ORR have occurred at the cathode.

After their formation at the cathode, the CO_3^{2-} anions are transported through the AEM to the anode by migration, resulting in the "carbonation" of the AEM and the catalyst layer ionomers (Figure 2.3). This carbonation reduces the AEM conductivity since CO_3^{2-} has a lower intrinsic mobility than OH^- [33,68,69], which increases the area-specific resistance (ASR) relative to OH^--only operation (ΔASR). However, this effect should not be overstated as it is only able to account for a small fraction of the performance loss when CO_2 is added to the cathode stream. Definitive experimental evidence will be presented below to support this. Less discussed, though thoughtfully pointed out and modeled by a few studies in the literature[43,61,70], migration is not the only mass transport event that influences the location and distribution of CO_3^{2-}; diffusion also plays a role. The interplay between migration and diffusion results in carbonate concentration profiles that impact performance in two primary ways beyond Ohmic considerations, one pH-based (Nernstian) and the other electrocatalytic.

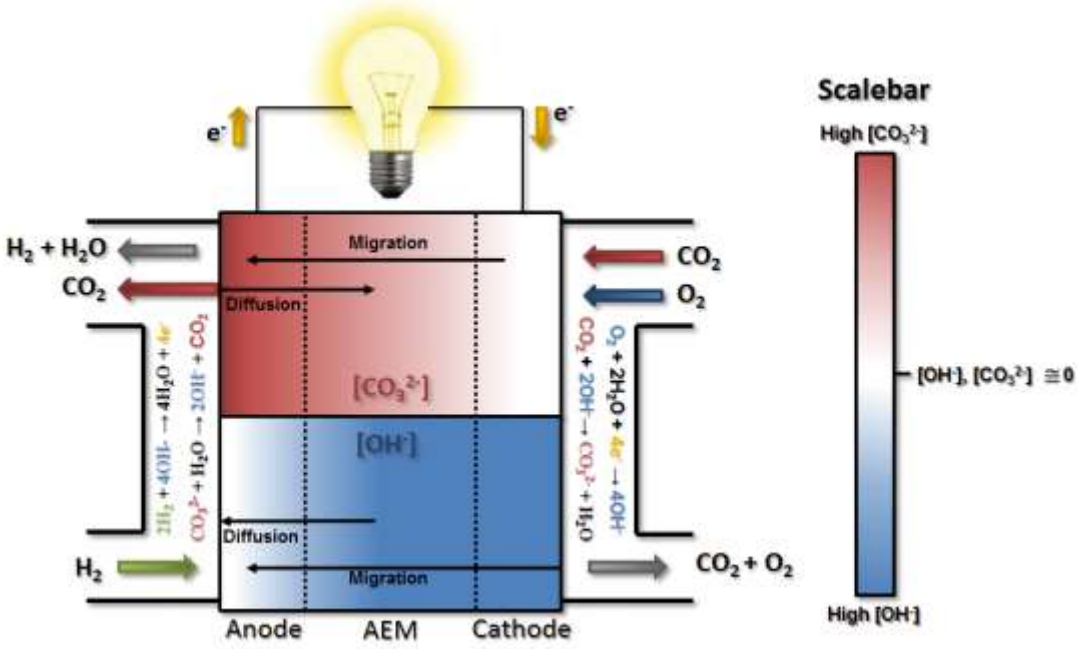

Figure 2.3 Illustration of the carbonate and hydroxide transport and distribution in operating AEMFCs with CO_2 present in the cathode reacting gas. The top section of the diagram isolates the CO_3^{2-} behavior in operating cells, with the color gradient representing the concentration gradient. The top section of the diagram shows the OH^- concentration gradient, as well as the directionality for hydroxide migration and diffusion.

The first CO_2-related effect is pH related and due to a concentration gradient, that builds up across the cell, as discussed in Chapter 1. Under typical operating currents, net migration of ions across the AEM is very fast (on the order of 1 s at relevant current densities and AEM thicknesses). This ionic flux towards the anode leads to lower concentrations of CO_3^{2-} in the AEM and cathode compared to the anode (though the extent will depend on factors including membrane thickness, current density and the CO_2 concentration in the cathode stream). The resulting CO_3^{2-} concentration gradient provides a driving force for back-diffusion of CO_3^{2-} anions from the anode towards the cathode – setting up a steady-state concentration gradient where there is significant carbonate accumulation within the anode [43,61], although the absolute and variation of the carbonate level within the anode has yet to be determined directly. The presence of carbonate in the anode decreases the local pH, leading to an increase in the anode potential (ΔV_{Nernst}) according to the Nernst equation during operation, which has been theoretically estimated to be as high as 180 – 350 mV [43,71].

The second effect arises from the reduced migrational supply and reduced local concentration of reacting OH^- anions as CO_3^{2-} carries charge from the cathode to the anode and accumulates there. Previous work (and the data in Figure 2.2 for cell pulsing to 0.1 V) has shown evidence that at high anode overpotentials that CO_2 is quickly removed from operating AEMFCs – suggesting that carbonate may directly react with H_2 at those overpotentials to produce water and CO_2 thereby significantly accelerating decarbonization (also supported by data on slide 17 in Ref. [72]). However, the long timescales needed to completely decarbonate AEMFCs at typical operating current and higher cell voltages (lower anode overpotentials), such as Figure 2.1, strongly suggests that such direct reaction

does not appreciably occur at conditions of practical interest. Hence, it can be assumed in this work that essentially the entirety of the steady-state electrochemical current is generated through OH^--based HOR and ORR reactions (Equations 1.1 and 1.2, respectively). Therefore, when CO_3^{2-} anions carry charge through the AEM, the balance of reacting OH^- that is no longer supplied by migration (due to CO_3^{2-} carbonate conduction) must be compensated for by diffusion, which is an intrinsically slower process.

Therefore, CO_3^{2-} in the anode effectively shuts off catalyst sites with high local CO_3^{2-} concentration due to reduced access to OH^- ions – increasing the effective current density on OH^- accessible anode catalysts. This means that although the presence of carbonate species does not negatively impact the intrinsic HOR electrocatalysis [73], the high CO_3^{2-} concentration in the anode does cause an increase in the kinetic resistance, inducing polarization losses that lower the operating cell voltage (denoted as ΔR_{ctHOR}).

These new resistances lead to a more complex equation for the operating cell voltage, though one that is insightful for the analysis of AEMFCs that have been carbonated:

$$V_{cell} = V_{OCV} - i\left(R_{\Omega,OH} + R_{ctORR} + R_{mtORR} + R_{ctHOR}\right) - \Delta V_{Nernst} - i(\Delta ASR + \Delta R_{ctHOR}) \quad (2.2)$$

The assignment of all of the new kinetic overpotential to the anode is supported by experimental work by Matsui *et al.* [74] who found, using a three-electrode AEMFC configuration with a reversible hydrogen reference electrode, that the cathode overpotential was hardly changed by the presence of CO_2, while the overpotential of the anode increased considerably.

The above-discussed behavior of carbonated AEMFCs is very similar to cation-contaminated PEMFCs [75–78], though some critical differences do exist. Most important, in

this case the "contaminant", CO_3^{2-}, is continuously created at the cathode, moved to the anode, and removed from the anode gas stream. Similar processes do not exist for cation-contaminated PEMFCs with the exception of the NH_3/NH_4^+ couple [79]. For CO_2 containing AEMFCs, CO_3^{2-} can be removed during operation by introducing a CO_2-free oxidant, activating a "self-purging" mechanism, which has been discussed in Chapter 1[42]. For reasons discussed above, under normal operating conditions this self-purging is not a result of direct electrochemical reaction of carbonates, but rather thermodynamic equilibrium. Under pseudo steady-state conditions, the CO_2 uptake rates at the cathode equal the release rates at the anode and a static concentration polarization exists across the anode, AEM, and cathode based on balancing between migration and diffusion of OH^- and CO_3^{2-}, illustrated in Figure 2.3.

In order to minimize the effect of CO_2 and carbonation on operating AEMFCs, it is important for the field to better understand how CO_2 uptake, membrane carbonation, and CO_2 release occur. There are both transient and steady-state concerns with little experimental data to provide insight or support modeling validation. The results presented here quantify the uptake and release rates of CO_2, quantify the amount of CO_2 within the MEA under different steady-state conditions, and provide data as to the performance and high frequency resistance of AEMFCs under specific CO_2 conditions. This first of its kind data provides significant insight into the performance losses and ultimate potential of AEMFCs when exposed to CO_2. This work provides direct evidence regarding the extent to which the CO_2 fed to the cathode becomes integrated into the AEMFC, directly correlates carbonation with AEMFC performance, and provides critical data needed to

validate modeling efforts that try to quantify rates of CO_2 uptake and release, as well as the negative effects of CO_2 on performance.

2.2.1 DYNAMIC OBSERVATION OF CO_2 UPTAKE AND TRANSPORT IN OPERATING AEMFCS

To probe the uptake and release of CO_2 in AEMFCs, CO_2 (100, 200, 400, 800, 1600 and 3200 ppm) was added to cells at open circuit conditions as well as cells operated at 0.2, 0.5, 1.0 and 2.0 A cm^{-2}. For the entire data set, the concentration of CO_2 leaving both the anode and cathode was measured in real time. The results for 400 ppm CO_2 in O_2 are shown in Figures 2.4a and b, and the results for all of the other CO_2 concentrations are shown as Figures 2.5-2.9. The first condition assessed was steady-state at the open-circuit voltage (labeled as 0.0 A cm^{-2}), which allows the diffusional dynamics of ionomer and membrane carbonation to be observed since there is no current driving the movement of CO_3^{2-} from the cathode to the anode. Though the OCV did not change, in agreement with the work by Inaba *et al.* [80], it was clear during the experiment that the AEM and AEI were being converted to the carbonate form since the amount of CO_2 leaving the cathode was far below the 400 ppm feed, Figure 2.4b, especially over the first 300 s.

After the CO_2 was added to the cathode at OCV, the concentration initially rose from zero to *ca.* 130 ppm as two things were occurring: absorption of CO_2 into the AEM and ionomer and the increase in the CO_2 partial pressure in the gas stream (the humidifier and cell lag in the CO_2 concentration is denoted as "blank" in Figure 2.4b - determined in a cell containing a Teflon membrane, which does not uptake CO_2 and form CO_3^{2-} anions). Comparing the "blank" and 0.0 A cm^{-2} (black dotted line) plots in Figure 2.4b, it was clear that there was rapid CO_2 uptake into the AEM because the concentration of CO_2 leaving

the AEM-containing cell was always lower than with the ”blank”. By 600 s, the concentration of CO_2 in the cathode rose to the inlet concentration, suggesting that the AEM was extensively carbonated after 10 min, which is in good agreement with previous studies on AEM carbonation in the presence of gas-phase CO_2 [42,52,81].

When CO_2 was added to the cathode of a fully broken-in cell operating at a constant current density, the cell response was very different. In all cases (from 0.2 A cm^{-2} to 2.0 A cm^{-2}), after a brief time lag, the cell operating voltage precipitously declined, the ASR increased, and CO_2 was emitted at the anode; this is shown in Figures 2.4a and b. What changed with current density were the magnitude and timing of these phenomena. At the highest current density that was tested, 2.0 A cm^{-2}, it took approximately 31 s for CO_2 to be measured in the anode stream (from the time that the reacting gas CO_2 concentration increased). It took another 96 s after CO_2 was initially measured in the anode gas before a quasi-steady-state was achieved. When the current was halved to 1.0 A cm^{-2}, the time for CO_2 break-through to the anode was approximately doubled (65 *vs.* 31 s), though the time to reach equilibration was very similar (90 *vs.* 96 s). This trend continued for 0.5 A cm^{-2} and 0.2 A cm^{-2}.

The CO_2 breakthrough time increasing with decreasing current density is intuitive as the rate of ion movement through the AEM is slower at lower current density. The timescale for CO_2 breakthrough was much longer than the amount of time it would take for an ion to travel between the cathode and anode. At current densities of 2.0 A cm^{-2}, 1.0 A cm^{-2}, 0.5 A cm^{-2}, and 0.2 A cm^{-2}, the average time for a net single-charged anion to travel through the AEM is 410 ms, 820 ms, 1.6 s and 4.1 s, respectively (The ETFE-BTMA AEM has an IEC of 2.05 ± 0.05 mmol g^{-1} with *ca.* 43 μmol of charge-carrying, covalently-bound

positively-charged, groups in the 5 cm^2 membrane active area). The fact that the breakthrough time for CO_2 is much longer than the average time it takes for an anion to move from the cathode to the anode directly supports the idea that CO_2 is not emitted as part of a direct electrochemical process during normal operation and needs time to reach a critical concentration in the anode that allows it to be released into the anode exhaust (through the equilibrium reactions of Equations 1.3-1.4). This explains the lag in the CO_2 release as well as provides an explanation as to why breakthrough occurs earlier at higher currents since CO_3^{2-} back-diffusion is less effective resulting in critical anode concentrations being reached sooner. At steady-state, the rate of CO_3^{2-} formation at the cathode will equal the rate of carbonate release (CO_2 emission) at the anode; the transient and steady-state fluxes for CO_3^{2-} reaction and CO_2 emission at several current densities and CO_2 concentrations to the cathode are given in Figure 2.4c.

From the difference in the response of the AEM and "blank", it was possible to calculate that essentially all of the charge carrying groups in the AEM and AEI were carbonated during this time and at steady-state contained a mixture of HCO_3^- and CO_3^{2-} (see as Figure 2.10).

Hence, the quantity of CO_2 that has been taken up into the cell by the AEM and AEI is the integrated area between these two plots. From here, the degree of carbonation (DOC, % of charge groups converted to the carbonate form) can be calculated by:

$$DOC = \frac{(Charge\ per\ CO_2)(\mu mol\ CO_2)}{(Charge\ per\ group)(\mu mol\ AEM\ groups + \mu mol\ AEI\ groups)} = \frac{(2)(38.2)}{(1)(42.8+25.5)} = 1.11 = 111\%$$

This number being higher than 100% validates literature data on membranes that were carbonated outside of operating cells with no current flowing where the balance in the membrane is a mixture of both carbonate and bicarbonate. The data above could be used

to make a rough calculation of the ratio of carbonate to bicarbonate since bicarbonate cannot exist with significant quantities of OH^- and CO_3^{2-} due to the equilibrium constraints.

If it is assumed that the ionomeric materials are completely carbonated, then the average charge per CO_2, ε, can be found by:

$$\frac{(\varepsilon)(38.2)}{(42.8+25.5)} = 1.00$$

Here, ε = 1.79, meaning that 79% of the charge groups are in the CO_3^{2-} form and 21% are in the HCO_3^- form at open circuit.

From the transient flux data, the amount of carbonate in the system at steady-state, as well as the degree of carbonation, could be calculated (Table 3.1). To calculate the quantity of carbonate anions in the operating cell at steady state for any operating condition, the number of CO_2 molecules taken up by the cell were quantified. The data in Figure 2.4c and Figures 2.5c-2.9c provide a pathway to do this because it gives the molar flux of CO_2 that is entering the cell when no uptake occurs ("blank"). It also provides the CO_2 flux that is leaving from both the anode and cathode with time until the cell reaches steady state. From this data, the three curves ("blank" vs. time, anode exhaust vs. time, and cathode exhaust vs. time) can be integrated and the total number of moles of CO_2 (N_{CO2}), and hence CO_3^{2-}, can be calculated by:

$$N_{CO2} = \int \text{"blank"}(t)\, dt - \int \text{"anode exhaust"}(t)\, dt - \int \text{"cathode exhaust"}(t)\, dt \quad (2.3)$$

From here, the DOC was also calculated from the equation above.

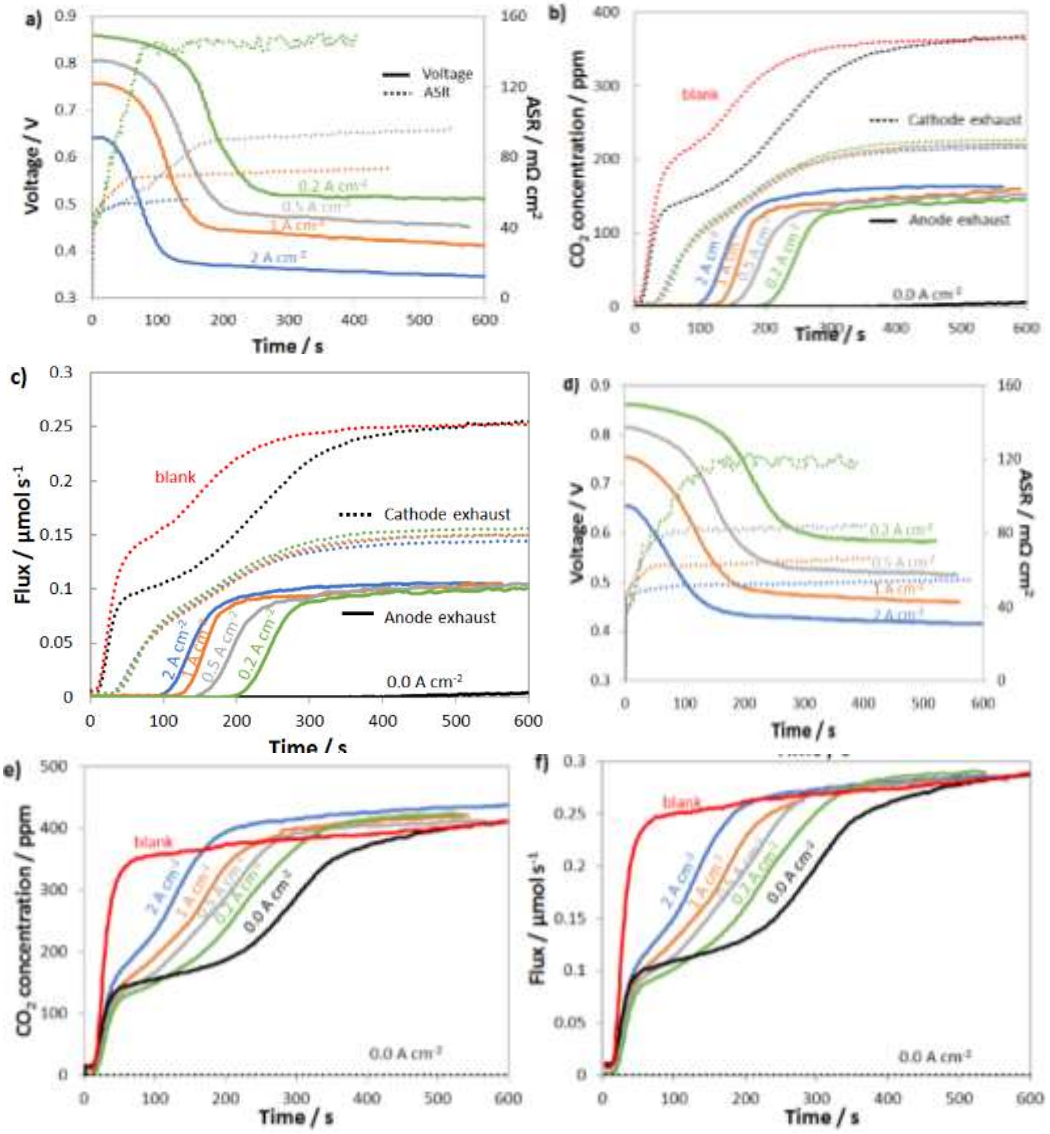

Figure 2.4 Uptake of 400 ppm CO_2 fed to both the anode and cathode of H_2/O_2 AEMFCs operating at 60°C and discharging at 0.00 (load off), 0.20, 0.50, 1.0 and 2.0 A cm^{-2} current densities. a) voltage decrease and ASR increase upon introduction of CO_2 into the cathode reacting gas; b) CO_2 emission from the anode (solid lines) and cathode (dotted lines) when 400 ppm CO_2 is fed to the cathode; c) CO_2 flux fed to the cell and released from the anode (solid lines) and cathode (dotted lines) when 400 ppm CO_2 is fed to the cathode; d) voltage decrease and ASR increase upon introduction of CO_2 into the anode reacting gas; e) CO_2 emission from the anode (solid lines) and cathode (dashed line) when 400 ppm CO_2 is fed to the anode; f) CO_2 molar flux fed to the cell and released from the anode (solid lines) and cathode (dashed line) when 400 ppm CO_2 is fed to the anode. AEM used was an ETFE-TMA (IEC = 2.05 mmol g^{-1}).

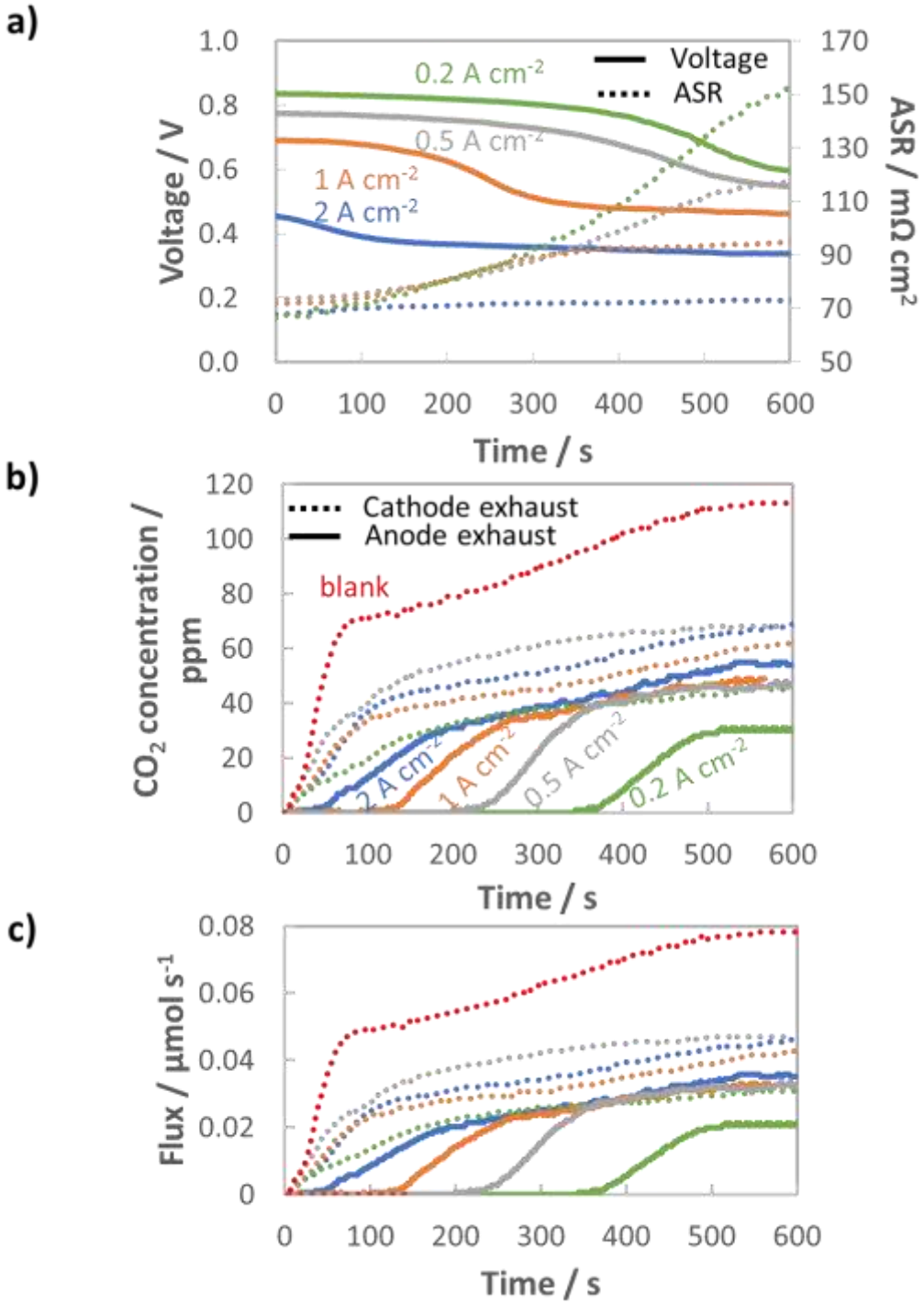

Figure 2.5 Uptake of 100 ppm CO_2 fed to the cathode of H_2/O_2 AEMFCs operating at 60°C and discharging at 0 (load off), 0.20, 0.50, 1.0 and 2.0 A cm^{-2} current densities. a) voltage decrease and ASR increase upon introduction of CO_2 into the cathode reacting gas; b) CO_2 emission from the anode (solid lines) and cathode (dotted lines) when 100 ppm CO_2 is fed to the cathode; c) CO_2 flux fed to the cell and released from the anode (solid lines) and cathode (dotted lines) when 100 ppm CO_2 is fed to the cathode.

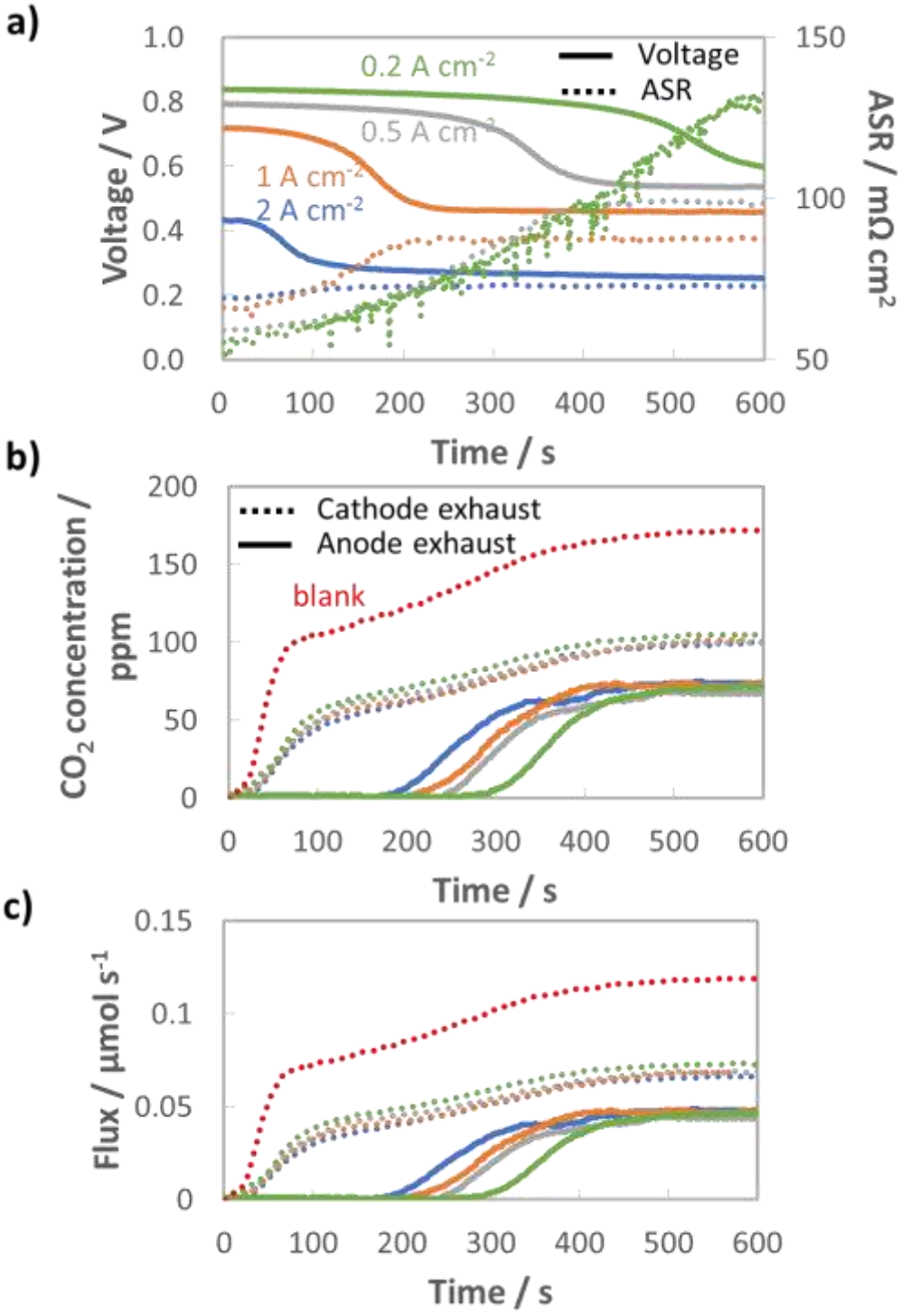

Figure 2.6 Uptake of 200 ppm CO_2 fed to the cathode of H_2/O_2 AEMFCs operating at 60°C and discharging at 0 (load off), 0.20, 0.50, 1.0 and 2.0 A cm^{-2} current densities. a) voltage decrease and ASR increase upon introduction of CO_2 into the cathode reacting gas; b) CO_2 emission from the anode (solid lines) and cathode (dotted lines) when 200 ppm CO_2 is fed to the cathode; c) CO_2 flux fed to the cell and released from the anode (solid lines) and cathode (dotted lines) when 200 ppm CO_2 is fed to the cathode.

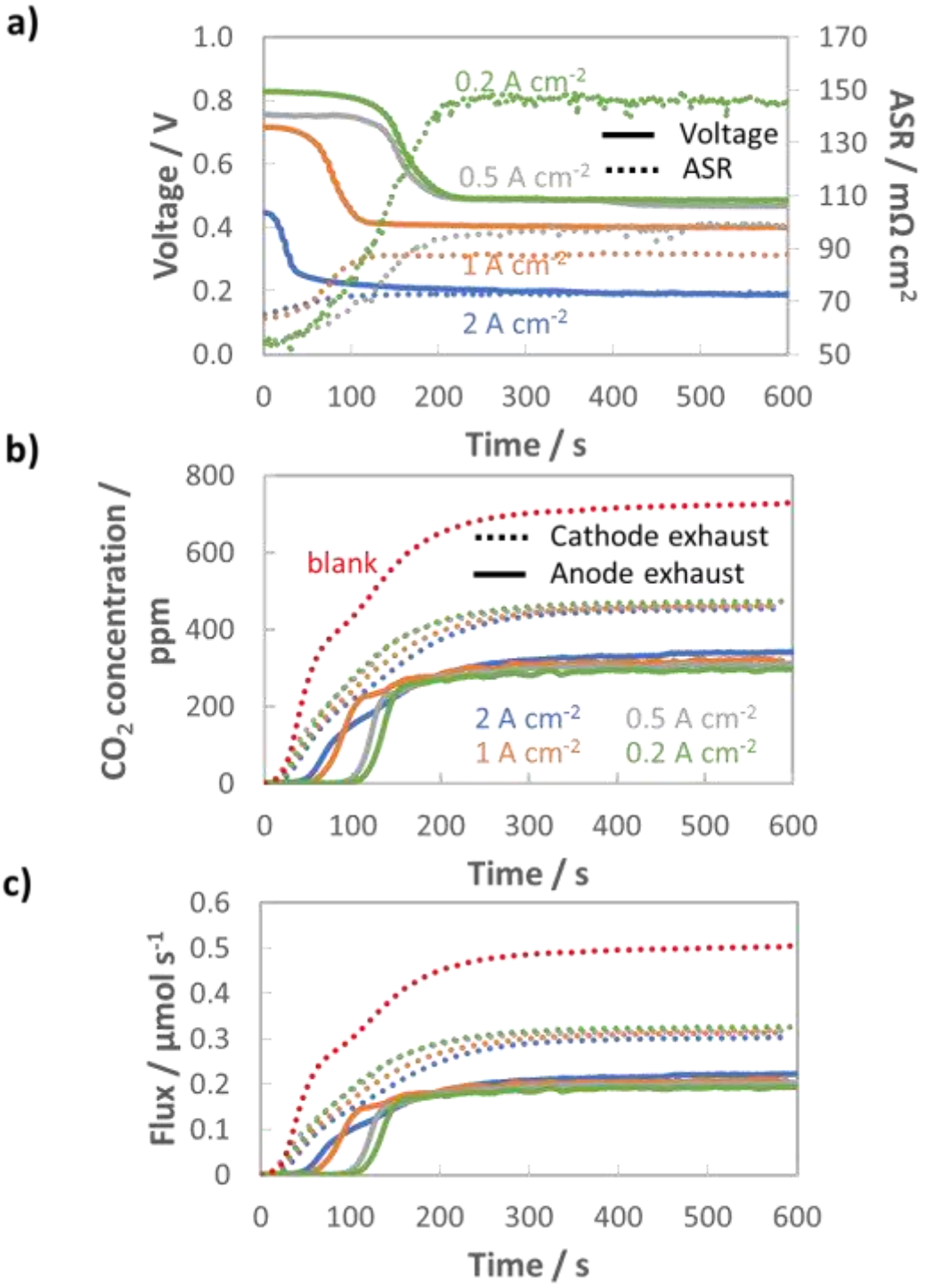

Figure 2.7 Uptake of 800 ppm CO_2 fed to the cathode of H_2/O_2 AEMFCs operating at 60°C and discharging at 0 (load off), 0.20, 0.50, 1.0 and 2.0 A cm^{-2} current densities. a) voltage decrease and ASR increase upon introduction of CO_2 into the cathode reacting gas; b) CO_2 emission from the anode (solid lines) and cathode (dotted lines) when 800 ppm CO_2 is fed to the cathode; c) CO_2 flux fed to the cell and released from the anode (solid lines) and cathode (dotted lines) when 800 ppm CO_2 is fed to the cathode.

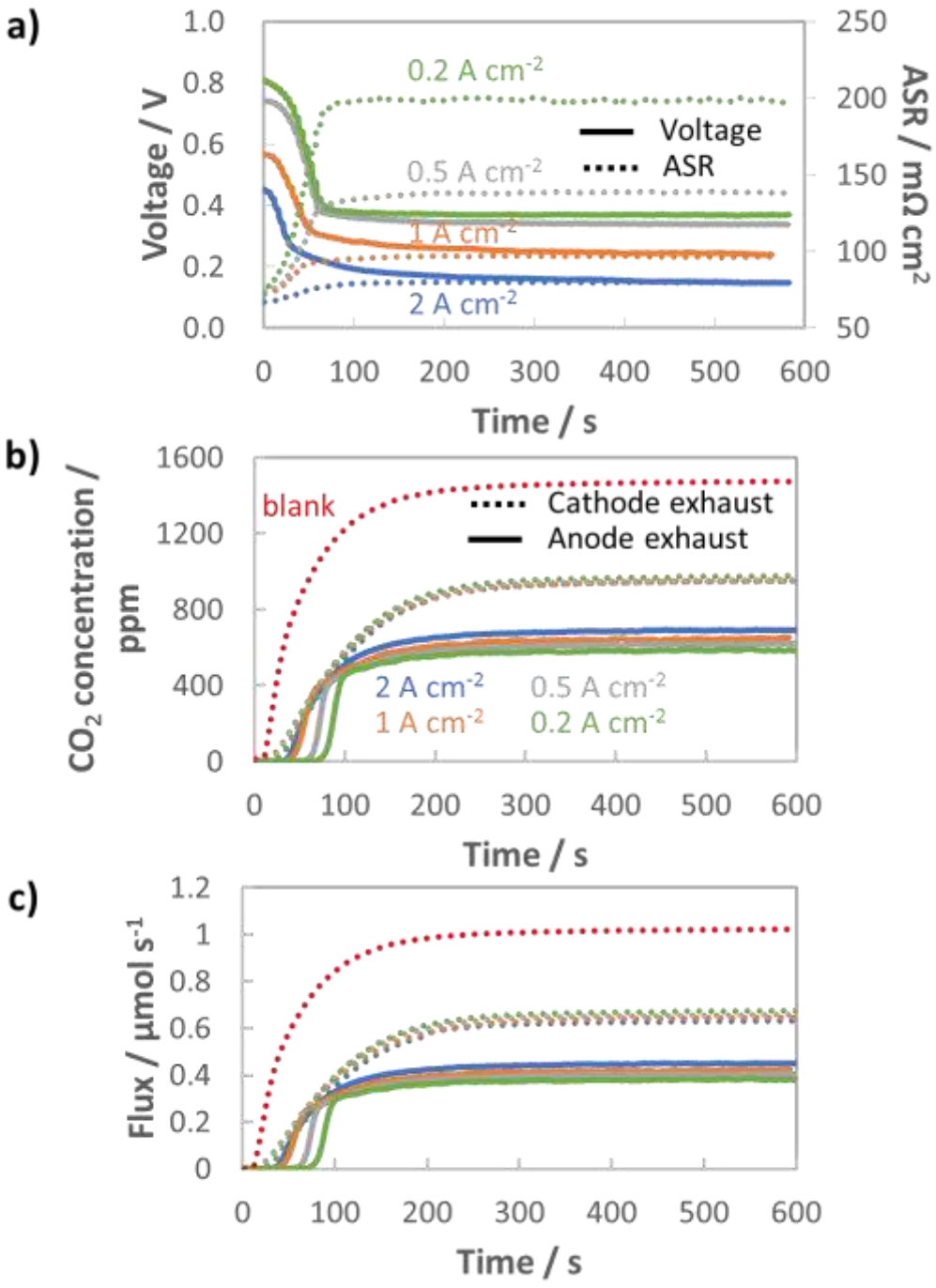

Figure 2.8 Uptake of 1600 ppm CO_2 fed to the cathode of H_2/O_2 AEMFCs operating at 60°C and discharging at 0 (load off), 0.20, 0.50, 1.0 and 2.0 A cm^{-2} current densities. a) voltage decrease and ASR increase upon introduction of CO_2 into the cathode reacting gas; b) CO_2 emission from the anode (solid lines) and cathode (dotted lines) when 1600 ppm CO_2 is fed to the cathode; c) CO_2 flux fed to the cell and released from the anode (solid lines) and cathode (dotted lines) when 1600 ppm CO_2 is fed to the cathode.

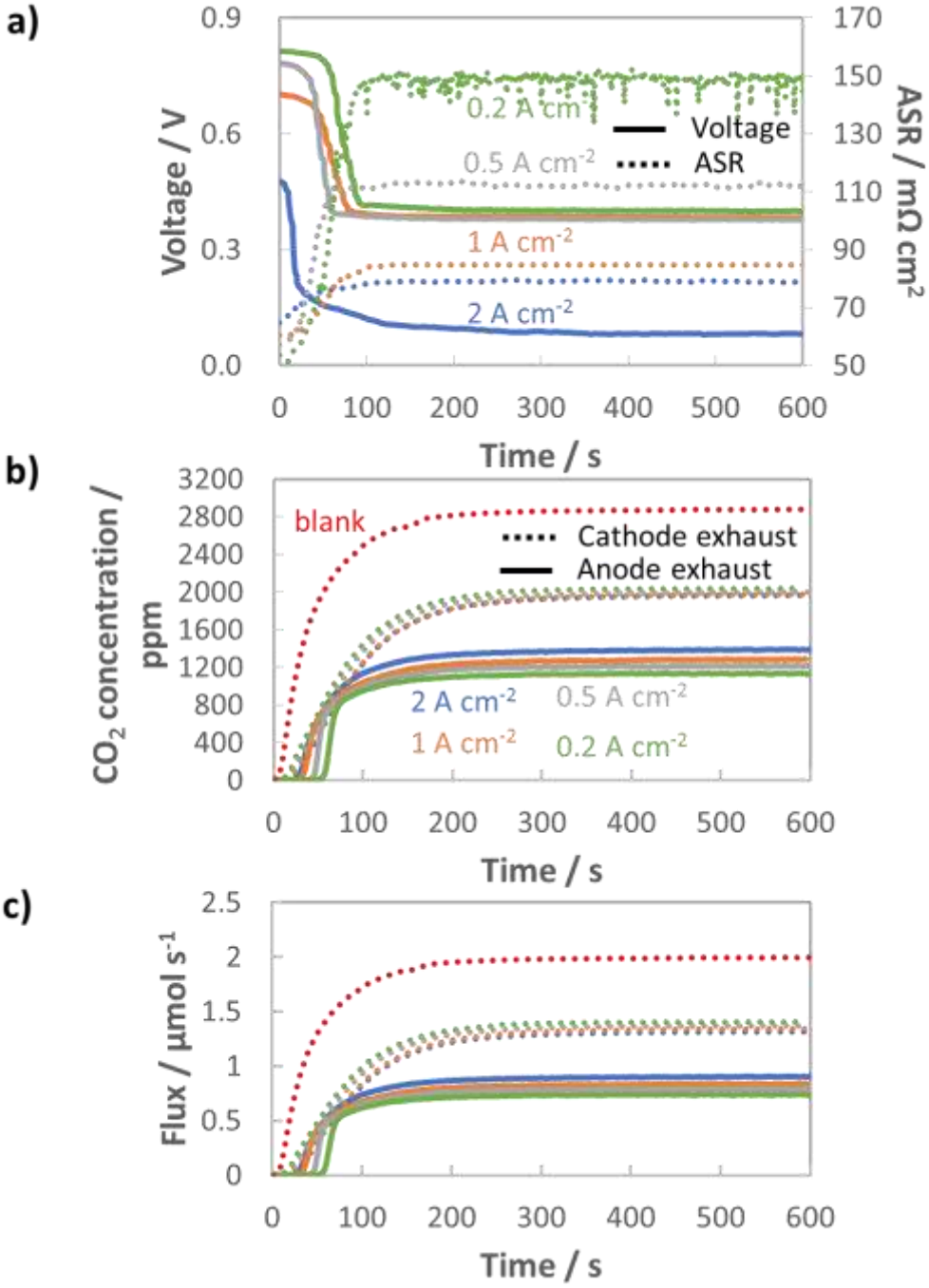

Figure 2.9 Uptake of 3200 ppm CO_2 fed to the cathode of H_2/O_2 AEMFCs operating at 60°C and discharging at 0 (load off), 0.20, 0.50, 1.0 and 2.0 A cm^{-2} current densities. a) voltage decrease and ASR increase upon introduction of CO_2 into the cathode reacting gas; b) CO_2 emission from the anode (solid lines) and cathode (dotted lines) when 3200 ppm CO_2 is fed to the cathode; c) CO_2 flux fed to the cell and released from the anode (solid lines) and cathode (dotted lines) when 3200 ppm CO_2 is fed to the cathode.

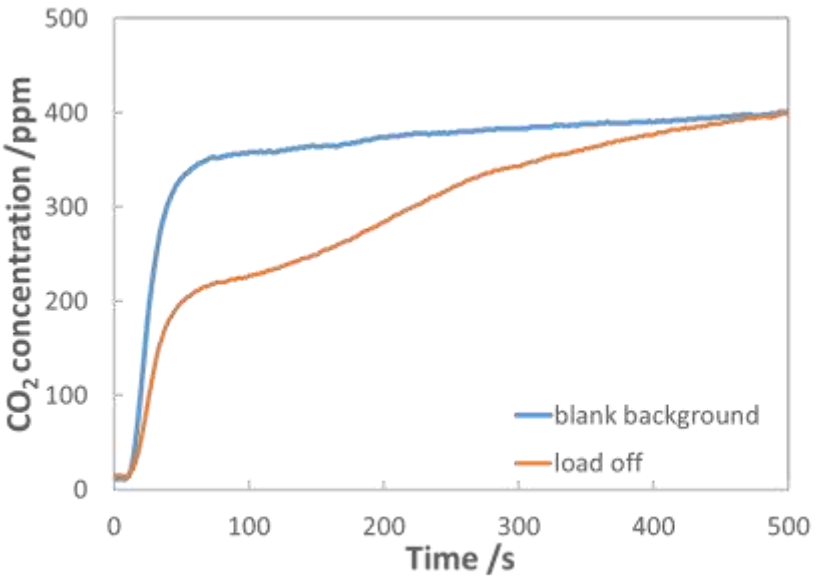

Figure 2.10 Comparison of CO_2 concentration leaving the AEMFC (fed at 400 PPM) when an AEMFC MEA is present and when Teflon is placed between the flowfields with no electrodes.

As expected, there was a greater amount of CO_3^{2-} present in the system with higher concentrations of CO_2 in the cathode stream. It was also found that the total amount of CO_3^{2-} in the system decreased with increasing current density. The change in the total number of CO_3^{2-} anions in the system with current density and cathode CO_2 concentration clearly explains the trends in the ASR.

Another interesting point in the dataset where it would be informative to know how much carbonate was in the system is after the CO_2 was removed from the cathode and the cell has reached the new quasi steady state. Figure 2.12a showed a set of typical carbonation + decarbonation experiments, where the cell was exposed to a known amount of CO_2 for 30 min and then the CO_2 was removed from the cathode gas stream. Cell decarbonation happened in 2 stages. The first stage was when the cell was operated for 30 min at the same current density. The second stage occurred after this 30 min of operation, when the cell voltage was pulsed down to 0.1 V. Here, the CO_2 coming out of the anode came out in a large slug that quickly decayed over 1-2 minutes. After that, the cell voltage was allowed to come back to steady state at the initial operating current and "complete" decarbonation was assumed if the steady state voltage was equal to the pre-CO_2 exposed operating voltage. The amount of carbonate left after the ~10 min new quasi steady state can be found by integrating the area under the slug of CO_2 that was measured with time at 0.1V. This calculation was also done for every current density and cathode CO_2 concentration and the resulting values are tabulated in Table 2.1. From here, the DOC was calculated from the equation above.

However, one interesting observation was that a plot of the total carbonate in the system vs. the change in the ASR (Figure 2.11) did not yield a single straight line for all conditions,

but there were trends as a function of current density and CO_2 concentration. To understand this, it should be noted that the high frequency resistance (HFR) measurement by the fuel cell test station is only measuring the two closest points separated by the ionomer; in other words, it is essentially a measurement of the membrane resistance. Therefore, the fact that the ASR is lower at a higher current density, even under conditions where the total amount of CO_3^{2-} in the cell is nearly identical to a lower current density, suggests that there is less carbonate in the AEM and more carbonate in the anode electrode as the current density is increased.

In summary, there were seven interesting observations when CO_2 was fed to the AEMFC cathode: 1) the CO_2 concentration leaving the cathode was only very modestly affected by the current density (Figure 2.4b), at least at the high flowrates investigated in this work; 2) the decrease in the cell voltage (Figure 2.4a) started to occur before CO_2 was measured in the anode exhaust; 3) the ASR increased immediately when CO_2 was added to the cell (Figure 2.4a); 4) the steady-state ASR was realized before the steady-state voltage was achieved and CO_2 was measured in the anode effluent (Figure 2.4a and b); 5) the steady-state ASR increased with decreasing current density (Figure 2.4a); 6) increasing current density decreased the amount of CO_3^{2-} present in the system at steady-state (Table 2.1); and 7) even at the highest current density and lowest CO_2 concentration (2.0 A cm^{-2} and 100 ppm, respectively) the CO_2-related overpotential was significant (167 mV), and the CO_2-related overpotential at 2.0 A cm^{-2} and 400 ppm CO_2 was even higher (259 mV). Combined, these observations suggest that: i) CO_3^{2-} formation at the cathode is very rapid (likely in quasi-equilibrium, which will be discussed more later); ii) initially CO_3^{2-} accumulates in the membrane and release is slow

Table 2.1 Degree of carbonation of operating AEMFCs (AEM+AEI) as a function of current density and CO_2 concentration in the cathode.

Current Density (A cm^{-2})	**PPM CO_2 in Cathode**	**Carbonate in AEMFC (umol) during CO_2 exposure**	**DOC during CO_2 exposure (%)**	**Carbonate remaining in AEMFC (umol) after CO_2 removed, @ new quasi steady state**	**DOC, after CO_2 removed, and new quasi steady state established after ~ 10 min (%)**
2.0	400	13.5	39.5	5.7	16.6
1.0	100	4.7	13.9	7.9	~22
	200	11.1	32.4	8.1	
	400	18.0	52.8	7.2	
	800	28.1	82.2	6.9	
	1600	38.8	113	7.9	
0.5	100	20.7	60.1	10.3	30.0
0.2	100	25.4	74.4	14.4	41.9
0.0 (no current)	400	38.2	111	N/A	N/A

until a critical concentration is reached; and iii) higher current densities increase the amount of CO_3^{2-} in the anode electrode.

To further study the dynamics of CO_2 uptake and CO_3^{2-} formation in the AEMFC system, as well as to simulate CO_2 that would build up in the anode or could be formed as an oxidative product of an alcohol fuel, CO_2 was also directly fed to the anode. For comparison sake, the CO_2 concentration in the anode H_2 reacting gas was also 400 ppm. The results of these experiments are shown in Figures 2.4e and f. The first thing that should be noted is that while current was flowing, no measurable CO_2 was ever found leaving the cathode, which can be attributed to the high net anionic flux relative to typical diffusion rates. Simply, CO_3^{2-} cannot diffuse and accumulate to a critical concentration at the cathode faster than migration pushes it to the anode under the conditions tested. Therefore, Figure 2.4e only shows the CO_2 concentration of the anode effluent and Figure 2.4f only shows the anode CO_2 flux. Like the cathode, there was approximately a 45 s lag between the time that CO_2 was turned on and its measurement (Figure 2.5). In this set of experiments, the dynamic CO_2 concentration in the effluent (before steady-state) increased with increasing current density, suggesting lower CO_2 uptake and CO_3^{2-} formation at higher currents. Also, the overall voltage decrease and ASR increase were both lower (but only slightly so) when CO_2 was fed to the anode *vs.* the cathode, most likely because of reduced carbonation stemming from the direction of ion transport.

2.2.2 RELATIONSHIP BETWEEN ANODE-EVOLVED CO_2 AND THE CO_2 CONCENTRATION IN THE CATHODE

At practical fuel cell current densities, the vast majority of the charge is carried by OH^-, not CO_3^{2-}, even at very high levels of carbonation. Therefore, a metric relating the amount

of charge carried by CO_3^{2-} (measured by the flux of CO_2 leaving the anode) at various current densities and CO_2 levels in the cathode (e^-/CO_2) would be useful – not only for fuel cells, but also for potential applications such as AEM-based electrochemical CO_2 capture [82].

Relating this ratio to the partial pressure of CO_2 in the cathode starts by defining the metric:

$$\log\left(\frac{e^-}{CO_2}\right) = log\left(\frac{i}{i_c}\right) = \log i - \log i_c \tag{2.4}$$

where i is the total current and i_c is the component of the total charge carried by CO_3^{2-}. This is an acceptable definition because at steady-state, when the net accumulation of CO_2/CO_3^{2-} in the membrane is zero, the amount of CO_3^{2-} formed in the cathode and carried through the AEM by is balanced by current through the external circuit. An expression for i_c can be obtained by assuming Butler-Volmer-type kinetics (assuming that the ORR at the cathode, where the CO_3^{2-} is formed, is irreversible), and correcting the directionality of the current:

$$i_c = -i_o exp\left[\frac{-\alpha F}{RT}\left(E - E^{o'}\right)\right] \tag{2.5}$$

where i_o is the exchange current density, α is the effective transfer coefficient, F is Faraday's constant, R is the ideal gas constant, E is the electrode potential and $E^{o'}$ is the formal potential. Rearranging:

$$E - E^{o'} = \frac{RT}{\alpha F} ln\ i_o - \frac{RT}{\alpha F}\ln i_c = \frac{2.303RT}{\alpha F} log\ i_c - \frac{2.303RT}{\alpha F}\log i_o \tag{2.6}$$

It has been noted in the literature [42], and suggested by the data in Figure 2.4, that carbonation during the ORR is very fast, and, therefore, it can be assumed that the CO_2 in the cathode gas stream is always in quasi-equilibrium with the generated anions. This Nernstian process can be represented by the Nernst equation, combining the reactions in

Equations 1.1 and 1.2, where the equilibrium potential is replaced by the actual electrode potential:

$$E - E^{o\prime} = \frac{RT}{nF}\ln\frac{P_{O2}P_{H2O}^2P_{CO2}^4}{[HCO_3^-]^4} = \frac{2.303RT}{nF}\log\frac{P_{O2}P_{H2O}^2}{[HCO_3^-]^4} + \frac{2.303RT}{nF}\log P_{CO2}^4 \qquad (2.7)$$

where P_i is the partial pressure of each gas, $[HCO_3^-]$ is the concentration of HCO_3^- in the AEM, and n is the number of electrons transferred in the ORR (n=4). It has been shown [43] and is generally accepted in the field (and assumed above) that the dominant anion in the operating AEMFC is CO_3^{2-}, not HCO_3^-. Therefore, it is important to express the Nernstian process relative to CO_3^{2-}, not HCO_3^-. Inserting the equilibrium expression between the CO_3^{2-} and HCO_3^- (Equation 2.8) into Equation 2.7:

$$[HCO_3^-] = \frac{[CO_3^{2-}]P_{H2O}}{[OH^-]K_{b2}} \qquad (2.8)$$

$$E - E^{o\prime} = \frac{RT}{nF}\ln\frac{P_{O2}P_{CO2}^4[OH^-]^4K_{b2}^4}{P_{H2O}^2[CO_3^{2-}]^4} = \frac{2.303RT}{nF}\log\frac{P_{O2}[OH^-]^4K_{b2}^4}{P_{H2O}^2[CO_3^{2-}]^4} + \frac{2.303RT}{nF}\log P_{CO2}^4 \qquad (2.9)$$

where $[CO_3^{2-}]$ is the concentration of carbonate in the AEM and K_{b2} is the equilibrium constant for the reaction in Equation 1.4. Combining Equations 2.6 and 2.9, i_c can be found as a function of the partial pressure of CO_2 in the cathode.

$$log\ i_c = \log i_o - \frac{\alpha}{n}\log\frac{P_{O2}[OH^-]^4K_{b2}^4}{P_{H2O}^2[CO_3^{2-}]^4} + \alpha\log P_{CO2} \qquad (2.10)$$

This result suggests that the CO_3^{2-} current should increase with the partial pressure of CO_2 in the cathode, which is logical. The final step in the derivation, relating the number of electrons transferred to the CO_2 partial pressure, combines equations 2.4 and 2.10.

$$\log\left(\frac{e^-}{CO_2}\right) = \left[\log i - \log i_o + \frac{\alpha}{n}\log\frac{P_{O2}[OH^-]^4K_{b2}^4}{P_{H2O}^2[CO_3^{2-}]^4}\right] - \alpha\log P_{CO2} \qquad (2.11)$$

Equation 2.11 makes two predictions, both of which are confirmed experimentally in Figure 2.11, which shows the results of steady-state measurements of CO_2 emission at

various current densities and concentrations. First, at any one current density (where everything in the brackets in Equation 2.11 is constant), there is a linear relationship between the log e^-/CO_2 and log P_{CO2} with a negative slope equal to the effective ORR transfer coefficient. The slope in Figure 2.11 is approximately -1, which is consistent with measurements of the effective transfer coefficient for the ORR in operating fuel cells [83,84]. Second, this equation predicts that lines at other current densities should be parallel as long as the mechanism is unchanged, and that higher current densities will yield a lower portion of CO_3^{2-} carrying the charge (increasing log e^-/CO_2). In fact, Figure 2.11 shows that charge is overwhelmingly carried by OH^- in these systems – even when the degree of carbonation at steady-state (Table 2.1) is high. Only at very high CO_2 concentrations (3200 ppm) and low operating current densities (0.2 A cm^{-2}) is the portion of the charge carried by the CO_3^{2-} ion significant (*ca.* 10%), though these are not realistic operating conditions for AEMFCs (whereas 400 ppm is). However, the fact that carbonate does carry charge through the system when CO_2 is present has significant impacts on the operating voltage, which will be discussed later.

The results from Figure 2.4, Figure 2.11 and Table 2.1 show that the large overpotentials experienced by AEMFCs when CO_2 is added to the inlet streams are caused by a relatively small overall CO_3^{2-} population. What is missing from the literature, and the discussion thus far, is a conclusive determination of which of the fundamental drivers (Ohmic, Nernst or anode HOR kinetics) primarily controls the carbonate-related losses. Such an insight could be invaluable in understanding the behavior of (and designing) ambient air-utilizing AEMFC systems.

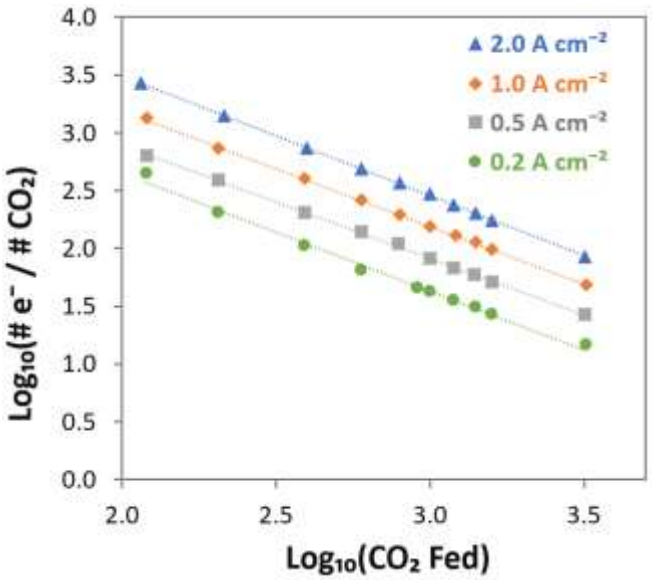

Figure 2.11 Visualizing the steady-state transport of CO_2/CO_3^{2-} from the cathode to the anode in AEMFCs operating at 0.2, 0.5, 1 and 2 A cm^{-2} at over a wide range of CO_2 concentrations. The linear relationship with a slope of -1 verifying the relationship predicted in Equation 2.11 between the cathode CO_2 feed concentration and the portion of the charge that is carried by CO_3^{2-}, showing that CO_2 uptake and CO_3^{2-} incorporation is a Nernstian process and driven by the ORR.

2.2.3 DECONVOLUTION OF CARBONATE-RELATED LOSSES IN OPERATING AEMFCS

Though the previous two Sections have established some basic parameters for the behavior of CO_3^{2-} in operating AEMFCs (*e.g.* it induces polarization losses, is formed in quasi-steady-state with the ORR and its concentration gradient changes with feed concentration and current density), what would be the most helpful from a design and operation perspective is a quantitative deconvolution of the polarization losses. Identifying which of the carbonate-related processes is performance-limiting would allow for solutions to be proposed and evaluated systematically.

The first step in quantifying the carbonate-related losses in operating AEMFCs was to track the performance decline for cells operating at steady-state at several current densities and over a wide range of cathode CO_2 concentrations. The response of a steady-state AEMFC operating at 1 A cm^{-2} to the introduction of 100, 200, 400, 800, 1600, 3200 ppm CO_2 to the cathode reacting gas is shown in Figure 2.4a, and equivalent data for AEMFCs operating at 0.2, 0.5 and 2.0 A cm^{-2} are provided in Figures 2.14a – c. Between each tested CO_2 concentration, the cell was decarbonated as described in the Section 2.1.3. The data shown in Figures 2.13a and 2.14a – c show one hour of AEMFC behavior at each CO_2 concentration – the first 30 min segment shows the carbonation event and the re-establishment of a new steady-state. The second 30 min segment shows the initial response following CO_2 removal (where pure O_2 is again fed).

As discussed earlier, the introduction of CO_2 to operating AEMFCs initiates an interesting series of dynamic events that, in concert, lead to reduced steady-state performance through three mechanisms: increasing the Ohmic resistance (ΔASR),

increasing the anode charge transfer resistance (ΔR_{ctHOR}) and increasing the thermodynamic anode potential (ΔV_{Nernst}). The challenge here is to find a systematic way to use the CO_2 exposure and removal data in Figure 2.13a, 2.14 to quantify the contribution of each of these resistances to the total CO_2-related overpotential. The general approach to extracting these three losses from the data was consistent regardless of the experiment. A representative description for 400 ppm CO_2 at 1.0 A cm^{-2} is given here for illustrative purposes, and then the summary of all the calculated parameters is shown in Figures 2.13b – d.

Before adding any CO_2 to the AEMFC operating at 1.0 A cm^{-2}, steady-state performance was established. The steady-state operating voltage at this condition was 0.72 V. The operating voltage for this cell is given by Equation 2.1. What this means is that the CO_2-free steady-state operating voltage already contains $R_{\Omega,OH}$, R_{ctORR} and R_{mtORR}; hence, the deviation of the operating voltage after adding CO_2 will only come from ΔV_{Nernst}, ΔASR and ΔR_{ctHOR}, as shown in Equation 2.2. After adding 400 ppm CO_2 to the cell, the new steady-state voltage that was reached was 0.44 V – meaning that the total CO_2 overpotential was *ca.* 280 mV. While the stoichiometries used in these experiments were high, leading to high CO_2 dosages, the observed performance losses (in combination with the total CO_2-related overpotential of ~260 mV for a cell operating at 2.0 A cm^{-2} with 400 ppm CO_2) suggest that the "self-purging" mechanism has a relatively modest effect in decarbonating the cell, and reducing CO_2-related voltage losses to an acceptable level during operation on ambient air will be a significant challenge, and may not be possible at all.

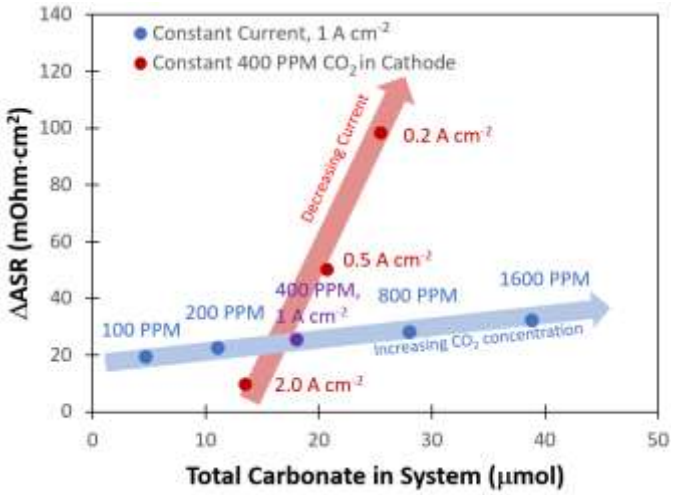

Figure 2.12 ASR changes vs. quantity of carbonate in the cell as a function of current density and cathode CO_2 concentration. As discussed earlier, the fact that these plots do not fall on a single line suggests that more of the carbonates are in the anode electrode than the AEM with increasing current density.

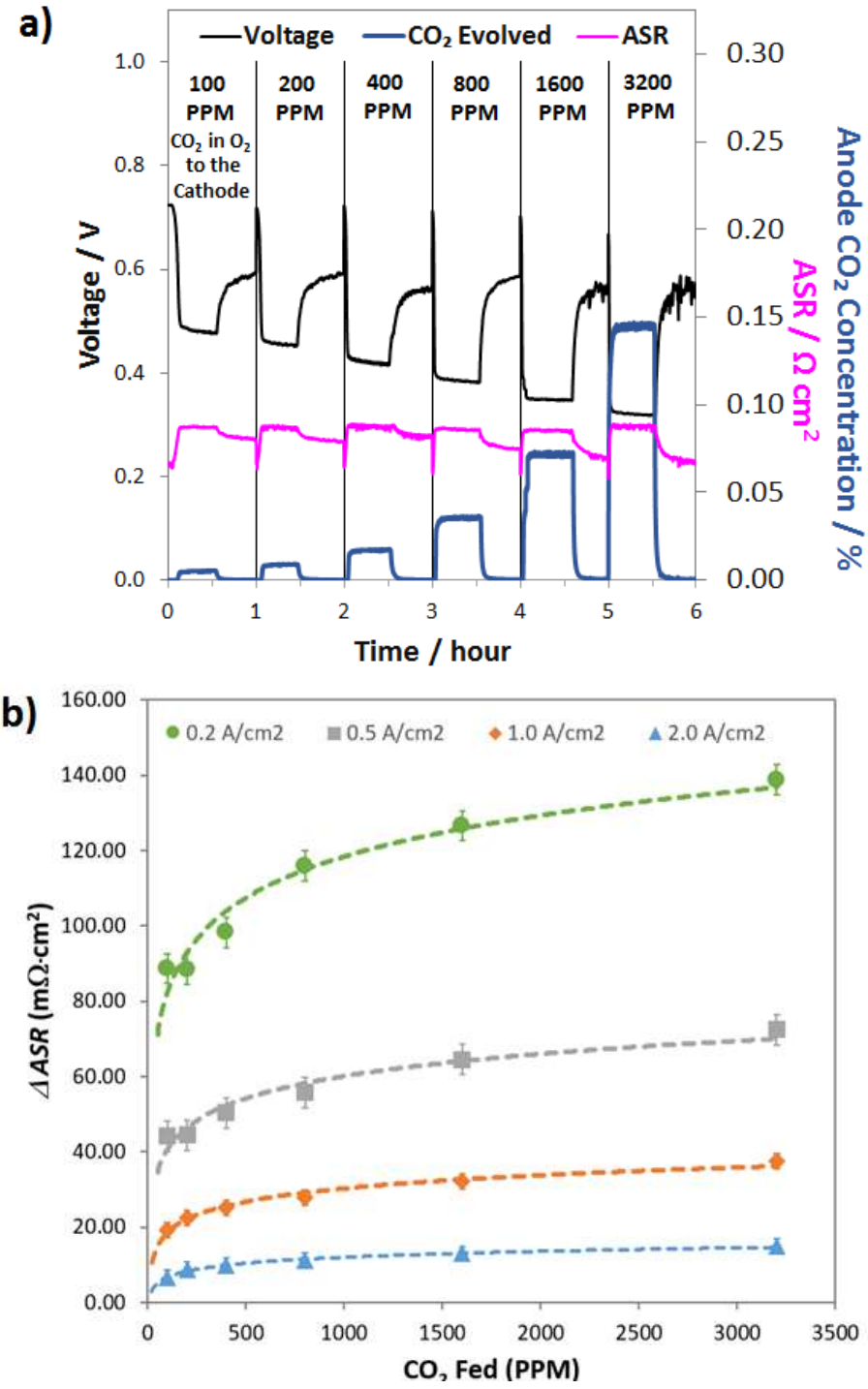
a)
Voltage
CO2 Evolved
ASR
100 PPM
200 PPM
400 PPM
800 PPM
1600 PPM
3200 PPM
CO2 in O2 to the Cathode
Voltage / V
ASR / Ω cm2
Anode CO2 Concentration / %
Time / hour
b)
0.2 A/cm2
0.5 A/cm2
1.0 A/cm2
2.0 A/cm2
ΔASR (mΩ·cm²)
CO2 Fed (PPM)

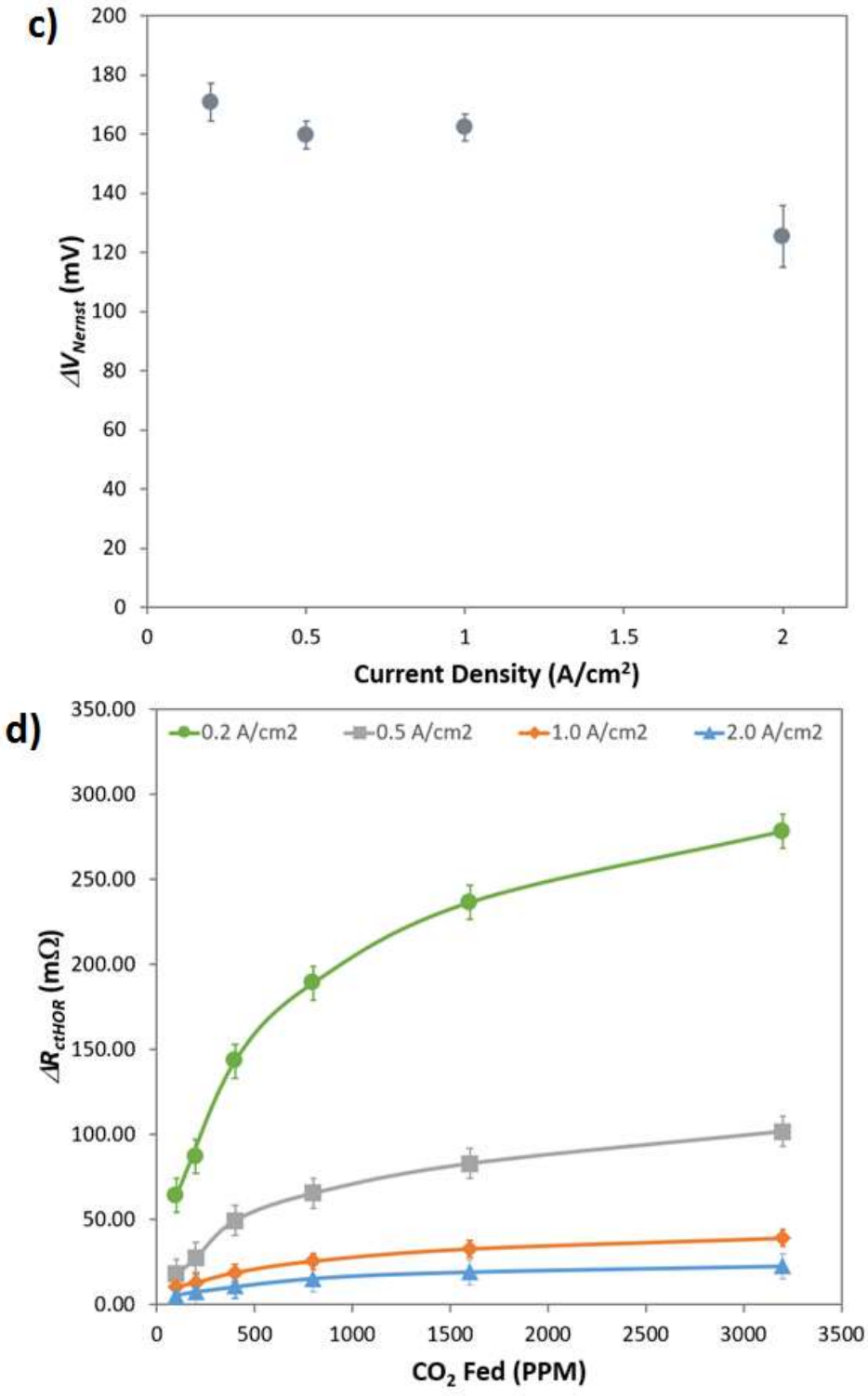

Figure 2.13 Deconvolution of CO_2 overpotential a) Response of an AEMFC operating at 1.0 A cm^{-2} to various concentrations of CO_2 in the cathode reacting gas; b) Summary of the change in the ASR at various current densities and CO_2 concentrations; c) AEMFC anode Nernstian voltage loss as a function of current density; d) Increase in anode charge transfer resistance with increasing CO_2 concentration and decreasing current density. All cells were operated at 60°C with an ETFE-BTMA AEM (IEC = 2.05 ± 0.05 mmol g^{-1}).

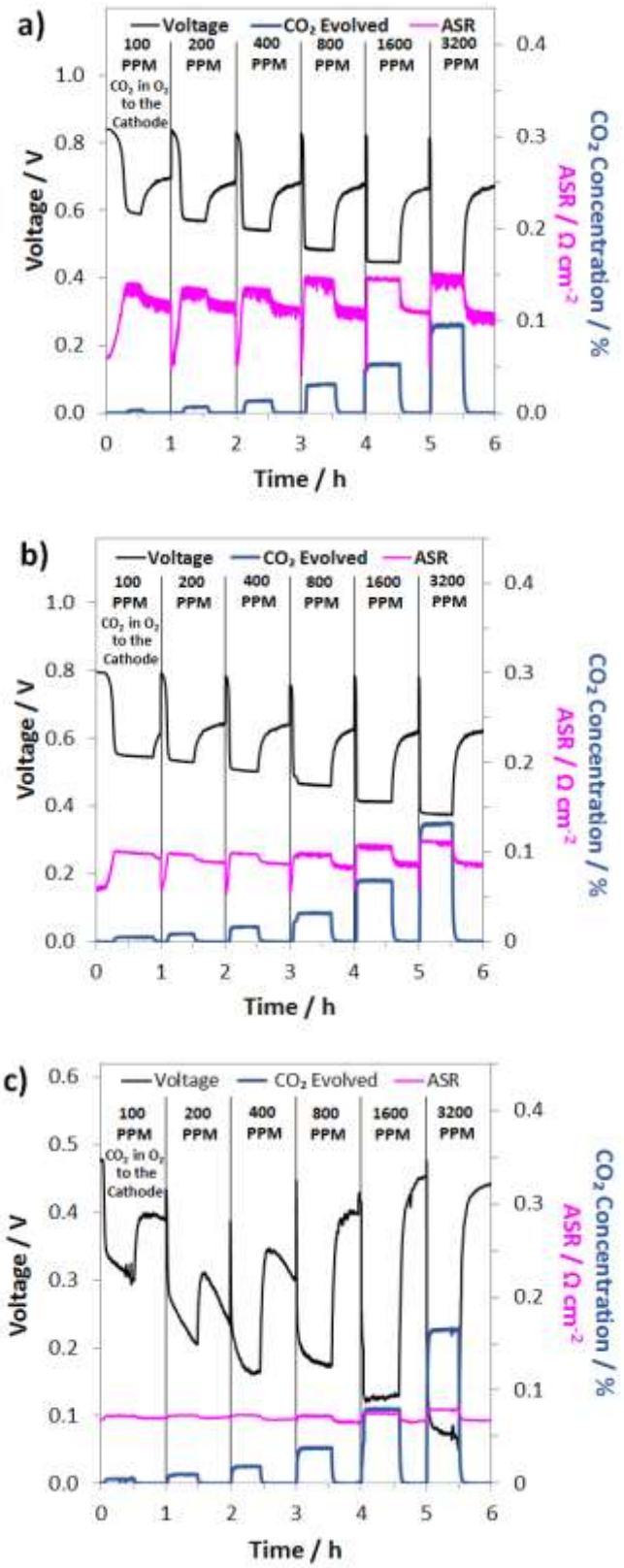

Figure 2.14 Response of an AEMFC operating at a) 0.2, b) 0.5 and c) 2.0 A cm^{-2} to various concentrations of CO_2 in the cathode reacting gas.

The first CO_2-related loss that was calculated was *ΔASR*. The ASR as a function of time is shown in Figure 2.4a, and under this operating condition, *ΔASR* was 25 mΩ cm^2. Assuming this *ΔASR* resulted in proportional Ohmic losses, at 1 A/cm^2 this would result in an Ohmic loss of 25 mV. For completeness, it is acknowledged that the measured ASR values do not yield the exact potential drop related to ion movement through the AEM due to the influence of diffusion [75,76]. However, the value measured here does give an accurate measure of average anion mobility and is presented here as an overestimation of the maximum Ohmic resistance that could be attributed to carbonation which remains a small percentage of total overpotential loss (<10%). Perhaps what is most important is that this observation clearly shows that the ASR change caused by the emergence and transport of CO_3^{2-} through the AEM represents a very small portion of the overall CO_2 overpotential.

For the AEMFC operating at 1.0 A cm^{-2} with 400 ppm CO_2 in the cathode, at minimum, 255 mV of the CO_2-related loss remains to be accounted for. The next stage of the deconvolution comes when CO_2 is removed from the cathode stream. Experimentally, a rapid increase in the cell potential was observed, to *ca.* 0.54 V, though the potential never exactly levels off to reach a new steady-state. That is because the only way that a true steady-state can be re-achieved is for all of the CO_3^{2-} to be removed, either by waiting for many hours (Figure 2.1), or by accelerated decarbonation at 0.1 V (Figure 2.2). However, it is important to consider what is happening phenomenologically in the AEMFC. When CO_2 is removed from the cathode, no new CO_3^{2-} anions are generated at the cathode and the concentration of CO_3^{2-} at that electrode drops towards zero as OH^- continues to be produced and that the CO_3^{2-} that was in the cathode (and the AEM) is progressively pushed toward the anode by migration (recall that the migrational residence time through the AEM

at this current is 820 ms). This suggests that there will be a brief transient period to establish a new quasi steady-state (on the order of ~10 min according to Figure 2.13a) after which essentially all of the migrational charge that is carried from the cathode to the anode is carried by OH^-. If this is the case, at the new quasi steady-state, no OH^- will need to be provided by diffusion in the anode for the HOR to occur.

Therefore, the voltage increase during this 10 min establishment of the new quasi steady-state after CO_2 removed can be mostly attributed to the relaxation of the kinetic limitations described by ΔR_{ctHOR} (though the new ASR acting on charge transport needs to be corrected for as well). At the condition above, 1.0 A cm^{-2} with 400 ppm CO_2 in the cathode, ΔR_{ctHOR} was calculated by Equations 2.4 and 2.5.

$$\Delta V_{ctHOR}(\text{mV}) = [0.544\ \text{V} - 0.443\ \text{V}] \times 1000 - (1.0\ \text{A cm}^{-2})(83.5\ \text{m}\Omega\ \text{cm}^2 - 75.3\ \text{m}\Omega\ \text{cm}^2) = 93.7\ \text{mV} \quad (2.6)$$

$$\Delta R_{ctHOR}(\text{m}\Omega) = \frac{93.7\ \text{mV}}{(1.0\ \text{A cm}^{-2})(5\ \text{cm}^2)} = 18.7\ \text{m}\Omega \quad (2.7)$$

Because not all of the reacting catalyst in the anode can be assumed to be completely void of carbonation effects (because of the balance of carbonate migration and diffusion), the calculations made from Equations 2.4 and 2.5 are likely a lower limit for ΔR_{ctHOR}, though the real value should be close since the rate of carbonate removal after the initial voltage increase is slow.

From here, the Nernst-related loss can be calculated for this case: 162 mV (281 mV - 25mV - 94 mV = 162 mV). Because the estimate for ΔR_{ctHOR} is a lower bound, 162 mV is an upper bound for ΔV_{Nernst}, though it should be close to the true value for the reasons discussed above. Interestingly, the Nernstian and charge-transport losses had a similar effect on the cell performance, and both were far more important in dictating the

performance decline than the Ohmic loss. A short description and visualized calculation of the decoupling process is provided in Figure 2.15.

Conducting the same analysis over the entire range of current densities and CO_2 concentrations can yield values for the total CO_2-related overpotential, ΔASR, ΔR_{ctHOR}, and ΔV_{Nernst} as well as the Ohmic voltage loss (ΔV_{Ohmic}) and the CO_2-related kinetic polarization (ΔV_{ctHOR}) at every condition. All of these values are given in Table 2.2. Performing the data deconvolution over such a wide range of current densities and cathode CO_2 concentrations yielded some very revealing trends and important insight into the behavior of carbonated AEMFCs. Not too surprisingly, the total CO_2-related overpotential was increased with decreasing current density and increasing CO_2 concentration in the cathode (Table 2.2). However, understanding why this happened requires digging into the trends in ΔASR, ΔR_{ctHOR}, and ΔV_{Nernst} more extensively.

Figure 2.13b presents the *ΔASR* values at all conditions. As the concentration of CO_2 in the cathode reacting gas was decreased, there less of a negative impact on the ASR. This makes sense from the transient and steady-state experimental results (Table 2.1) which showed that the total amount of CO_3^{2-} in the AEMFC was lower at lower CO_2 concentration in the cathode and increased current density. As discussed earlier, the overall trends in the ASR with current density and cathode CO_2 concentration (Figure 2.14) led to the conclusion that increasing the current density shifts the CO_3^{2-} concentration gradient toward the anode electrode. Hence, with increasing current density, relatively less and less CO_3^{2-} is present in the AEM (though the total CO_3^{2-} flux is higher, Figure 2.4c), resulting in a lower ASR.

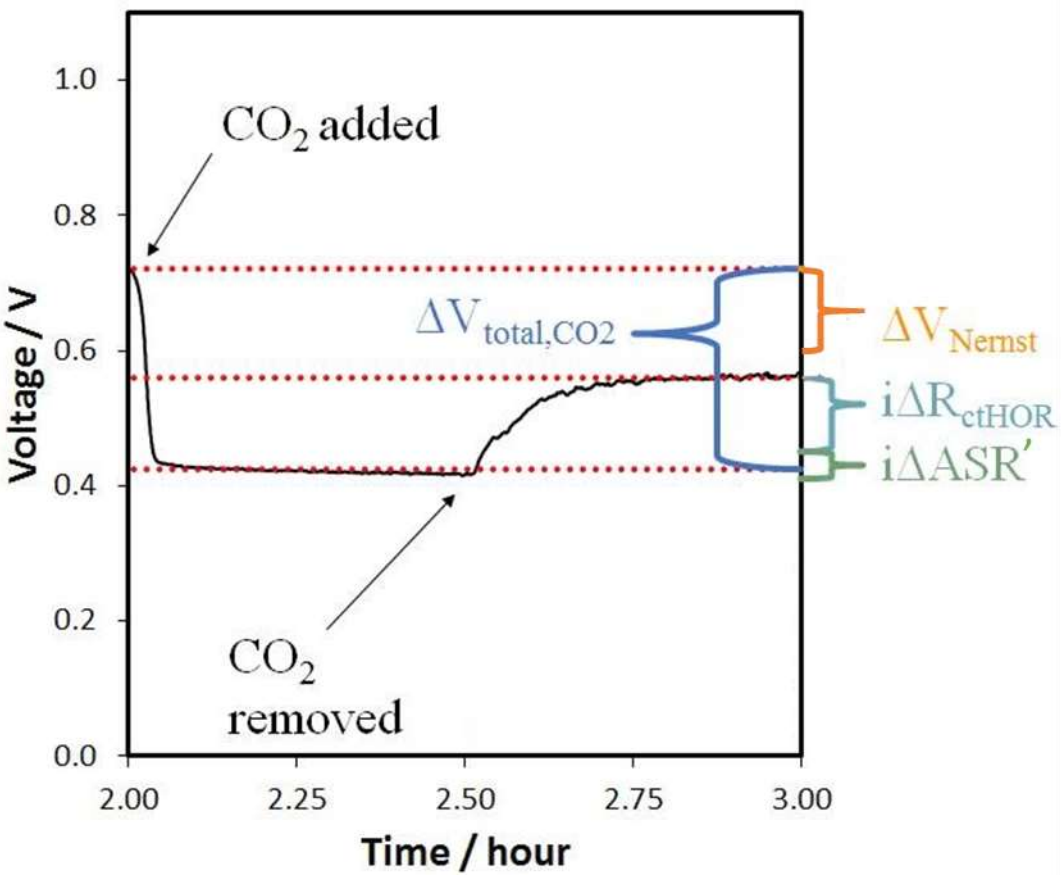

Figure 2.15 Visualized calculation of mechanism deconvolution

The fact that the concentration gradient shifts toward the anode with current density might lead to the assumption that ΔV_{Nernst} (Figure 2.13c) should also increase with current density. However, there are two counter points that require discussion. First, the total quantity of carbonate in the cell is decreasing with increasing current density, which alone might limit the achievable value for ΔV_{Nernst}, particularly at high currents. Second, the anode potential is measured at the outermost portion of the anode at the gas diffusion layer, which is likely the point of the highest CO_3^{2-} concentration, as illustrated in Figure 2.3, and it is possible for that one specific location to be close to saturation over a wide range of conditions. ΔV_{Nernst} appeared to decrease with increasing current density, though the values at current densities ≤ 1.0 A cm^{-2} were very similar. The assertion that the outermost portion of the anode can be close to saturation was supported by the magnitude of ΔV_{Nernst} at the lower current densities, ~165 mV. The effective alkalinity of AEMFC cathode is between pH 13 – 14. It is also known that CO_3^{2-} is overwhelmingly the dominant carbon-based charge carrier and this can only happen in water at pH values > 11. Therefore, the maximum pH shift that could possibly be expected at the anode in an operating cell would be 3, resulting in a $\Delta V_{Nernst,max}$ of 177 mV. The only data point in Figure 2.13c where ΔV_{Nernst} is markedly lower is at very high current, 2.0 A cm^{-2}, where ΔV_{Nernst} is ~125 mV. This lower value can be explained by either the lower overall carbonate concentration in the cell and anode at higher currents, and/or the development of a mixed potential throughout the anode because at high current density there is a significant number of OH^- ions being released throughout the anode as CO_2 is evolved through the reverse of Equations 1.3-1.4, though the root cause for this behavior will likely need to be teased out through computational modeling. It is also noteworthy that the ΔV_{Nernst} was completely

unaffected by the cathode CO_2 concentration, which gives additional support to the arguments above.

One area where the higher carbonate concentration in the anode did have a major impact on the AEMFC behavior is in ΔR_{ctHOR}, Figure 2.13d. At higher overall carbonate content, increased cathode CO_2 concentration and/or lower current density, ΔR_{ctHOR} was also higher, sharply increasing over the entire scale of tested concentrations. At a constant CO_3^{2-} concentration (same ppm CO_2 in the cathode stream), ΔR_{ctHOR} actually decreased with increasing current, even though the total amount of carbonate in the anode electrode was higher at higher current. This observation yields important insight into the location of carbonate in electrodes, suggesting that higher current densities compress the volume occupied by carbonates to the outermost portion of the anode, which effectively allows more catalyst sites to have easy access to reacting OH^-.

2.2.4 AEMFC RESPONSE AT LOW CO_2 CONCENTRATIONS

A practical interpretation of the experiments shown in Figure 2.13 is that the polarization losses from AEMFC carbonation are significant at all current densities and near-ambient CO_2 concentrations, and that AEMFCs will likely require pre-scrubbing of CO_2 from the operating air. Additionally, the dynamics of CO_2 uptake (fast) and release (slow) mean that even if CO_2 could be quickly removed from the anode stream to avoid significant accumulation, losses would still be high. One sensible approach to reducing CO_2-related overpotential is to lower the cathode inlet concentration, which is particularly intriguing for stationary implementations of AEMFCs where the volume and weight of a CO_2 scrubber is less of a concern than it is for mobile or transportation applications. Figure 2.16a explores the response of an AEMFC operating at 1 A cm^{-2} with 5 – 50 ppm CO_2 in

Table 2.2 Summary of the CO_2-related resistances and overpotentials as a function of current density and cathode CO_2 concentration (in O_2). The AEMFC was operated at 60°C with an ETFE-BTMA AEM. Gas flowrates were 1 L min^{-1} at both the cathode and anode (H_2).

Current Density (A/cm^2)	PPM CO_2 in Cathode	Total CO_2-related overpotential (mV)	ΔASR ($m\Omega\ cm^2$)	R_{ctHOR} ($m\Omega$)	ΔV_{Ohmic} (mV)	ΔV_{Nernst} (mV)	ΔV_{ctHOR} (mV)
2.0	100	167	6.7	5.3	13.4	101	53
	200	216	8.6	7.3	17.3	125	73
	400	259	9.9	11.3	19.8	126	113
	800	298	11.2	15.2	22.4	123	152
	1600	338	12.9	19.0	25.9	122	190
	3200	385	14.9	22.5	29.9	130	225
1.0	100	236	19.3	10.7	19.3	163	53
	200	246	22.5	12.8	22.5	159	64
	400	281	25.3	18.7	25.3	162	94
	800	319	27.9	25.6	27.9	163	128
	1600	359	32.1	32.8	32.1	163	164
	3200	406	37.5	39.2	37.5	173	196
0.5	100	227	44.2	18.0	22.1	160	45
	200	260	44.4	27.6	22.2	168	69
	400	306	50.4	49.5	25.2	157	124
	800	351	55.8	65.5	27.9	159	164
	1600	394	64.5	82.9	32.3	155	207
	3200	450	72.4	101.7	36.2	159	254
0.2	100	255	88.6	64.1	17.7	173	64
	200	271	88.4	87.0	17.7	167	87
	400	324	98.3	143.2	19.7	161	143
	800	386	116.0	189.0	23.2	173	189
	1600	433	126.6	236.4	25.3	171	236
	3200	486	138.8	278.3	27.8	180	278

the cathode reacting gas. Though the voltage loss was less than at higher concentrations, even down to 5 – 10 ppm CO_2 in the cathode the CO_2-related polarization was significant, approximately 140 mV.

Figure 2.16b shows the response of an AEMFC operating at 1 A cm^{-2} with 5 – 50 ppm CO_2 added to the anode H_2 reacting gas. The behavior of low-level CO_2 in the anode is very similar to the cathode; at 10 ppm, the total CO_2-related voltage loss was 136 mV. For CO_2 present in both the cathode and anode, Figure 2.16 suggests that if there is a lower threshold below which an operating AEMFC is immune to carbonation, it is very low - below 5 ppm (although it should be noted that dosage is also important and decreasing flow rates could also have a beneficial impact).

2.2.5 INFLUENCE OF TEMPERATURE ON CO_2-RELATED POLARIZATION LOSSES AT 400 PPM

Figure 2.16 showed that simply removing a portion of the CO_2 in ambient air will not be sufficient to eliminate the CO_2-related losses in operating AEMFCs. In fact, the above work demonstrated that even at 5 ppm CO_2 significant performance losses occurred. Therefore, it is important for researchers to identify other fundamental and operational properties of the system that can be manipulated to reduce the AEMFC sensitivity to CO_2. One pathway to reducing the amount of carbonate accumulated in the system is to increase the cell operating temperature. Increasing temperature would have several positive impacts on carbonate: i) CO_2 has lower solubility in water as the temperature is increased;[85] ii) the kinetics for CO_2 release (reverse of Equations 1.3 and 1.4) at the anode will improve; iii) the mass transport rate of evolved gaseous CO_2 from the anode will increase; and iv) the intrinsic kinetics for the ORR and HOR will improve.

Figure 2.17 summarizes the response of AEMFCs with a LDPE-BTMA membrane operating at 0.2, 0.5, 1.0 and 2.0 A cm^{-2} and several temperatures (60, 65, 70, 75, 80 °C) following the introduction of 400 ppm CO_2 to the cathode and anode. Regardless of where the CO_2 was introduced, increasing the temperature simultaneously decreased the total CO_2 overpotential and the ASR (Figures 2.17a – c). This experimental result is in stark contrast to recent modeling results that suggested increasing the cell temperature would not have a beneficial effect on AEMFC operation[43]. One possible explanation for the increased performance is that less CO_2 was apparently taken up into the system. Figure 2.17b shows that the concentration of CO_2 being emitted from the anode side of the cell decreased with increasing temperature. At steady-state, this means that less CO_2 was absorbed at the cathode. Figure 2.17d shows that when CO_2 was fed to the anode, increasing the temperature resulted in lower CO_2 uptake at that electrode as well, which is shown by the increasing concentration of CO_2 in the anode effluent. It should also be noted in Figures 2.17b and d that the values trend upward with increasing current density due to the consumption of the fuel and oxidant gases. Positively, the improved performance at elevated temperatures suggests that increasing temperature is indeed one possible mechanism to improve the CO_2 tolerance of operating AEMFCs; however, the CO_2-related overpotential is still too high for many practical applications. A combination of lower CO_2 concentration, more modest air stoichiometry, and elevated temperature can further reduce the total CO_2 overpotential. For instance, it was observed that an AEMFC operating at 1 A cm^{-2} and 80^{o}C with 10 ppm CO_2 fed to the cathode (the same LDPE-BTMA membrane) had a total CO_2 overpotential of only 90 mV.

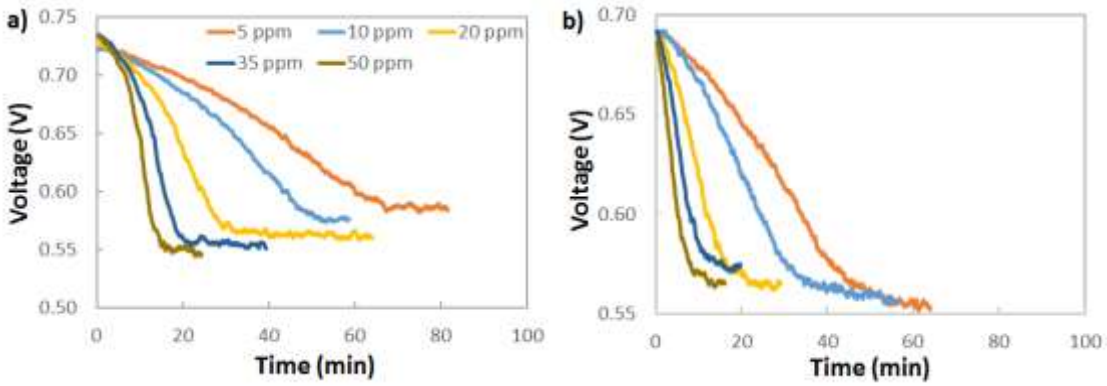

Figure 2.16 Exploring the existence of a lower threshold concentration for CO_2 present in the a) cathode and b) anode compartments. The AEMFCs were operated at an operating current density of 1.0 A cm^{-2} at 60 °C with the ETFE-BTMA AEM.

Deconvoluted data for AEMFCs operating at different temperatures but at a constant current of 1 A cm^{-2} and constant cathode CO_2 concentration of 400 ppm to find ΔASR, ΔV_{Nernst} and ΔR_{ctHOR} can be found in Table 3.3. As expected, the ASR generally decreased with increasing temperature due to the lower quantity of carbonates that were taken up into the membrane. However, the ASR value only varied slightly with increasing temperature, which meant that a similar portion of CO_3^{2-} anions were carrying the charge through the AEM, supported by the results of accelerated decarbonation experiments at 0.1 V as Table 3.4, which led ΔR_{ctHOR} to be fairly constant with temperature as well. Therefore, the primary impact of an overall reduced number of CO_3^{2-} anions in the AEM was that the carbonate accumulation in the anode (and hence the concentration gradient across the cell) was less severe with increased temperature. As a result, ΔV_{Nernst} was the most dependent on temperature, decreasing by nearly 50% from 60 – 80 °C.

In summary, with regards to temperature, it is possible that even higher temperatures (> 90 °C) may help, though no AEMs are currently readily available with stability above 80 °C in highly alkaline media that also have acceptable conductivity and water transport properties, though there is promising work ongoing in this area[86]. What this really points to is that improving the CO_2 tolerance of AEMFCs will require a combination of approaches to achieve success, at least some of which are not known today and will be particularly challenging for dynamic operation.

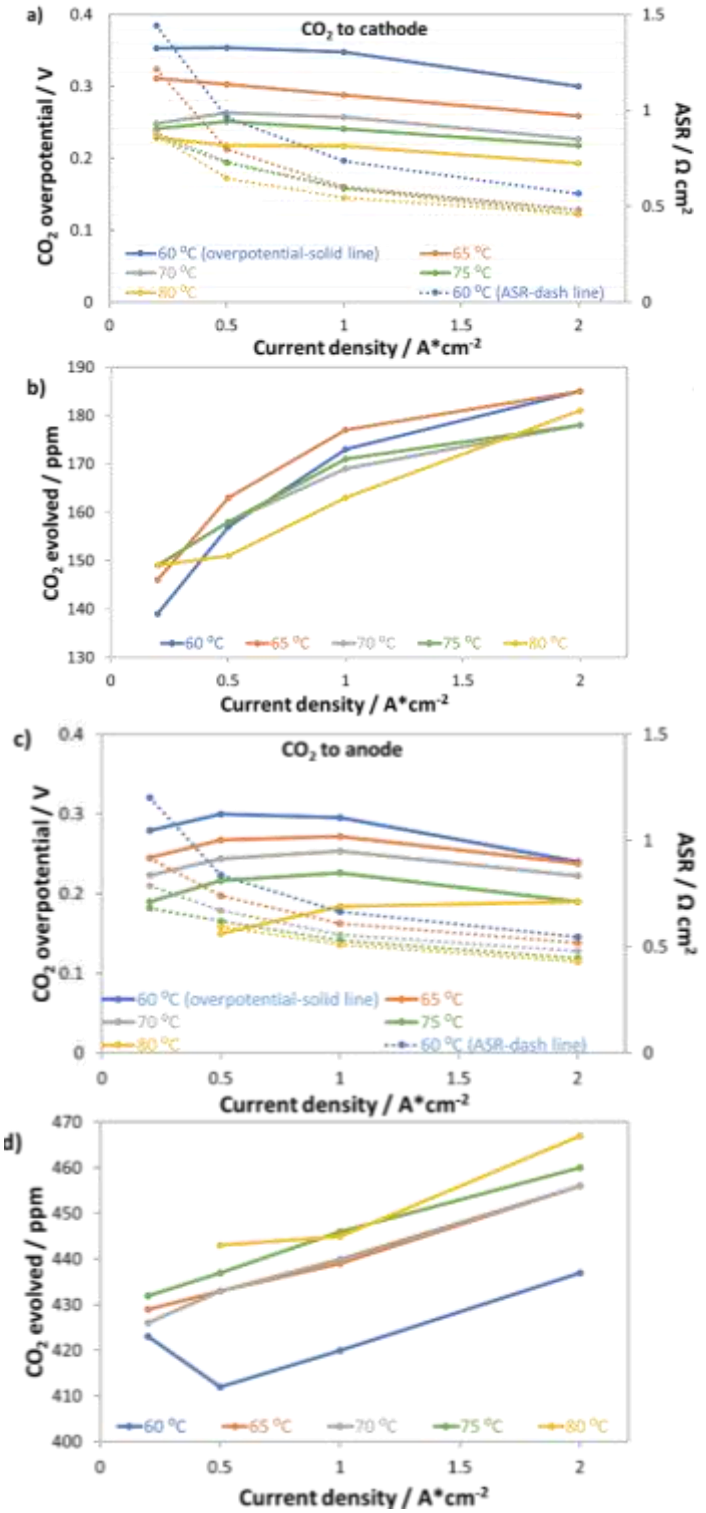

Figure 2.17 Impact of temperature on the total CO_2-related overpotential, HFR and anode CO_2 exhaust with 400 ppm CO_2 fed to the cathode at multiple current densities. Total CO_2 overpotential (solid lines) and ASR (dashed lines) when CO_2 was fed to the a) cathode and c) anode. CO_2 concentration in the anode effluent when CO_2 was fed to the b) cathode and d) anode. An LDPE-BTMA AEM (IEC = 2.5 mmol g^{-1}) was used in these experiments.

Table 2.3 Calculated values for ΔASR, ΔV_{Nernst} and R_{ctHOR} as a function of operating temperature for AEMFCs operating at a constant current of 1 A cm^{-2} and constant cathode CO_2 concentration of 400 PPM. It should be noted that the membrane here was LDPE-BTMA, so the absolute values can't really be compared with Table 3.2, but can be inter-compared to determine the impact of temperature on the behavior.

Temperature (°C)	ΔASR (mΩ cm²)	ΔV_{Ohmic} (mV)	ΔV_{Nernst} (mV)	R_{ctHOR} (Ω)	V_{ctHOR} (mV)
60	22.6	22.6	226	17.0	84.8
65	17.6	17.6	177	18.0	90.2
70	16.9	16.9	150	18.2	91.1
75	18.2	18.2	134	17.7	88.5
80	15.9	15.9	113	17.2	85.9

Table 2.4 Degree of carbonation (AEM+AEI) as a function of temperature for AEMFCs with LDPE AEM operating at 1 A cm^{-2} and constant cathode CO_2 concentration of 400 ppm.

Temperature (^oC)	60	65	70	75	80
Carbonate in AEMFC (µmol)	17.87	12.44	12.41	11.51	11.37
Degree of Carbonation, DOC (%)	33.98	23.66	23.60	21.88	21.61

2.3 SUMMARY

Even in highly performing AEMFCs, the addition of CO_2 has a severe negative impact, where the cell operating voltage is generally decreased by 200 – 500 mV depending on the reaction conditions. Lower CO_2 concentration in the reacting gas, higher current density and higher operating temperature all reduce the voltage penalty, but none have been shown be able to sufficiently minimize the CO_2 impact. This experimental work, the first of its kind to systematically investigate carbonation and to deconvolute the root causes for performance decline, has provided new insight into the dynamics of CO_2 and CO_3^{2-} in operating AEMFCs.

The formation of carbonates in the AEMFC occurs very quickly and in quasi-equilibrium with the reacting gas in the cathode. Decarbonation of the cell does not occur through direct electrochemical reaction under typical operating conditions – and is hence very slow; however, it is likely that carbonates do directly react with H_2 in the anode at very low voltages/very high anode potentials, which can allow for rapid cell decarbonation by pulsing away from typical operating conditions (e.g. 0.1 V or short-circuiting the cell), by diffusion toward the anode reacting gas. Therefore, decarbonation during operation by the so-called "self-purging" mechanism is slow, taking several hours even after onlytransient exposure to CO_2. Hence, "self-purging" cannot be relied upon to decarbonate a real system efficiently. Also, although pulsing to low operating voltages can be used for decarbonation, it most likely cannot be practically applied to engineered fuel cell stacks where some individual cells would experience negative voltages. The dominating loss in operating AEMFCs in the presence of CO_2 is not due to an increase in the Ohmic resistance from electrolyte carbonation. The dominating mechanism for voltage loss is accumulation

of carbonate anions in the anode, which results in two performance-robbing mechanisms: 1) a Nernstian thermodynamic shift in the anode potential from a decrease in the anode pH with carbonates; and 2) an increase in charge transfer resistance due to a lack of availability of reacting OH^- anions. The CO_2 concentration in the cathode and the current density are both determining factors for the quantity of CO_3^{2-} in the system, and the current density appears to play a primary role in dictating the CO_3^{2-} location and distribution. The HOR charge transfer resistance increases markedly with both increased CO_2 concentration and lower current density. Increasing the cell operating temperature appears to have almost no effect on the charge transfer resistance, but a significant effect on the Nernstian loss, meaning that the total CO_2-related overpotential can be reduced by increasing the temperature – or better yet, through a combination of higher current density, lower CO_2 concentration and higher operating temperature.

These new insights can help both modeling groups and experimental researchers to better understand operating AEMFCs, as well as allow them to pose and assess new solutions.

CHAPTER 3: EFFECT OF REACTING GAS FLOWRATES AND HYDRATION ON THE CARBONATION OF ANION EXCHANGE MEMBRANE FUEL CELLS IN THE PRESENCE OF CO_2

Alkaline-based fuel cells can have advantages over their more popular counterpart, the proton exchange membrane fuel cell. For instance, traditional AFCs can be operated with much lower quantities of noble metal catalyst or even with non-noble metal electrocatalysts like nickel, silver, etc.[6] Also, the electrolyte, liquid KOH, is much less expensive than Nafion®. For this reason, AFCs are still being pursued by companies such as AFC Energy PLC in the UK.

However, despite their possible cost advantages, AFCs are not being widely implemented today and the primary reason is that the OH^- anions in the electrolyte react with CO_2 in the ambient air cathode feed to form (bi)carbonates[7–9] (Equations 1.3 and 1.4).

The resulting CO_3^{2-} anions react with the mobile K^+ ions in the electrolyte to form the low solubility compound K_2CO_3, which can precipitate onto the cathode electrode. The salt formation lowers the performance and stability of the AFC. Strategies have been proposed to solve this CO_2 poisoning problem. For example, Cifrain and Kordesch[10] found that the negative effects of CO_2 poisoning can be partly mitigated by circulating the electrolyte. Another possibility is to change the electrolyte from a liquid (aqueous salt solution) to an ion conducting polymer, i.e. by the use of an AEM – creating so-called AEMFCs. AEMFCs avoid salting because the positively charged cations are stationary

(typically covalently bound to the polymer backbone) and not alkaline earth ions, eliminating the possibility for precipitates to form. As a result, the CO_3^{2-} anions are able to be transported through the AEM, and they are able to carry a portion of the charge from the cathode to the anode to complete the electrochemical circuit.[59,87] However, this does not mean that carbonation has a null effect on AEMFC behavior.

Now that AEMFC performance and stability have been enhanced to the point where their future deployment in real applications is realistic, it is now an important time in AEMFC development to begin to answer some of the contemporary issues that have to date been mostly put aside in the literature, including operating on real air, which contains CO_2, leading to the carbonation discussed above. Recently, there have been several experimental [53,61,74,80–82] and modeling [43,44,63,70] studies that have allowed researchers in the field to well-understand how adding CO_2 to high performing AEMFCs influences their behavior.

There are three primary mechanisms for voltage loss. First, as carbonate anions are formed at the AEMFC cathode from Equations 1.3 and 1.4, they migrate through the AEM from the air cathode to the hydrogen anode. Carbonate mobility is lower than hydroxide mobility, which leads to an increase in the area-specific resistance (ΔASR). Second, because hydrogen does not react with the carbonate directly at relevant potentials, carbonates are not immediately released on arrival to the anode as CO_2. Instead, there is a time lag while the carbonates accumulate at the anode and the pH of that electrode drops[45] – forcing the reverse of Equations 1.3 and 1.4 to occur before the CO_2 is eventually released. The drop in the anode pH leads to a thermodynamically-driven increase in the anode potential (ΔV_{Nernst}), reducing the overall cell voltage. This has been successfully modeled by Gerhardt et. al[44], Krewer et. al[43] and Wrubel et. al[88]. Third, the accumulation of

carbonates in the anode causes low local OH^- concentrations throughout the anode, leading to an increase in the anode charge transfer resistance, (ΔR_{ctHOR}). This third effect was captured quite well in the Gerhardt model[44]. Therefore, the operating voltage for an AEMFC with CO_2 in the cathode feed can be described by Equation 2.2[53]:

In total, the voltage loss from these three mechanisms are typically several hundred millivolts under operating conditions of practical interesting. The Nernstian voltage loss (ΔV_{Nernst}) and increase in the charge transfer resistance ($i\Delta R_{ctHOR}$) dominate the CO_2-related performance loss whereas the voltage loss related to the ASR ($i\Delta ASR$) increase is often a minor contributor (< 10% of the total loss) [44,53].

There are several pathways by which the CO_2-related voltage losses can mitigated. The most obvious mitigation strategy is to pre-scrub the air of CO_2 before feeding it to the cathode (and maybe even the H_2 before feeding it to the anode). As remedial measures during AEMFC operation, the presence of CO_2-derived bicarbonate can be reduced at high current densities[42,53] or high operating temperature[42,43,53] to obtain high electrochemical performance. Because decarbonation of AEMFC does not occur through direct electrochemical reaction, the self-purging process requires 40+ hours after contamination[53]. New strategies are expected to mitigate carbonate formation and the influence of CO_2 more efficiently through developments in materials science and fuel cell operation protocols.

In previous work,[53] it was shown that increasing the AEMFC operating current density and increasing the cell temperature can slightly mitigate the negative effects of CO_2. Lowering the CO_2 concentration in the reacting gas below 400 ppm can also help, but at high cathode flowrates, even having 5 ppm CO_2 in the cathode feed has been untenably harmful, resulting in CO_2-related voltage losses of about 100 mV[44,45,53]. Therefore, it is

important to continue to explore the impact of cell operating conditions on the tolerance of AEMFCs to the presence of CO_2 in the cathode feed. In this Chapter, three new variables are investigated: the anode flowrate, the cathode flowrate, and the cell hydration. The cathode reacting gas flowrate is expected to be important because it sets the total dose of CO_2 that is fed to the cell. The anode flowrate can influence the degree of cell carbonation because it will inevitably control the concentration of CO_2 (i.e. via dilution) in the anode stream. The CO_2 in the hydrogen stream, which is usually recirculated, can be taken back up into the cell. Lastly, the level of cell hydration may influence how much CO_2 can be taken up by the cell (i.e. Equations 1.1 and 1.2) as well as its overall concentration.

3.1 EXPERIMENTAL

The flowrate for O_2 or H_2 in experiments was varied from 0.2 to 1 L min^{-1}, meanwhile keeping constant 400 ppm CO_2 concentration in cathode feed and 0 ppm CO_2 in the anode feed. LDPE-BTMA was used. The second set of experiments investigated the effects of hydration level on AEMFC operating with 400 ppm CO_2 in cathode. Here, the dew points of both electrodes were systematically modified in order to change the hydration state of the cell; however, all other variables and operating procedures were identical to the description above. The electrode preparation process and cell assembly and break-in procedure are identical to Section 2.1.

3.2 RESULTS AND DISCUSSION

3.2.1 INFLUENCE OF FLOWRATE ON AEMFC PERFORMANCE WITH 400 PPM CATHODE CO_2

The effect of cathode flowrate (oxygen with 400 ppm CO_2) on the behavior of a carbonated AEMFC is presented in Figure 3.1. As shown in Figure 3.1a, the CO_2-related voltage loss decreased (i.e. improved) approximately linearly with decreasing cathode gas flowrate, showing that the total dose of CO_2 fed to the cell plays an important role in carbonation. Additionally, as shown in Table 3.1, the steady-state carbonation of the AEM and electrode ionomer in the operating cell increased with higher oxidant flowrate. As described in Chapter 2,[53] the carbonate content in the AEMFC can be estimated by first converting the CO_2 concentration vs. time data (Figure 3.1b) from the anode and cathode exhaust into flux vs. time data (Figure 3.1c) and then integrating the area under the flux curves for the anode exhaust, cathode exhaust and a "blank". The blank is a direct measure of the amount of CO_2 added to the cathode, a measurement that is made in the absence of the anionic polymer. Hence, the amount of carbonate/CO_2 in the cell for any operating condition can be calculated (N_{CO2}) by Equation 2.3.

Evidence for the uptake of CO_2 into the cell is also given by the cell's HFR (with ASR $\cong$ HFR $\times$ A where A = geometric cell area), shown in Figure 3.1a. Lower cathode flowrates resulted in a lower HFR. It was also interesting to note that it took a longer time for the cell to reach a stable HFR value and voltage at a lower flowrate. These dynamics also match well with what was observed with the CO_2 concentration in the anode exhaust, Figure 3.1b. Even at the same operating current density (same charge flux through the AEM), the CO_2

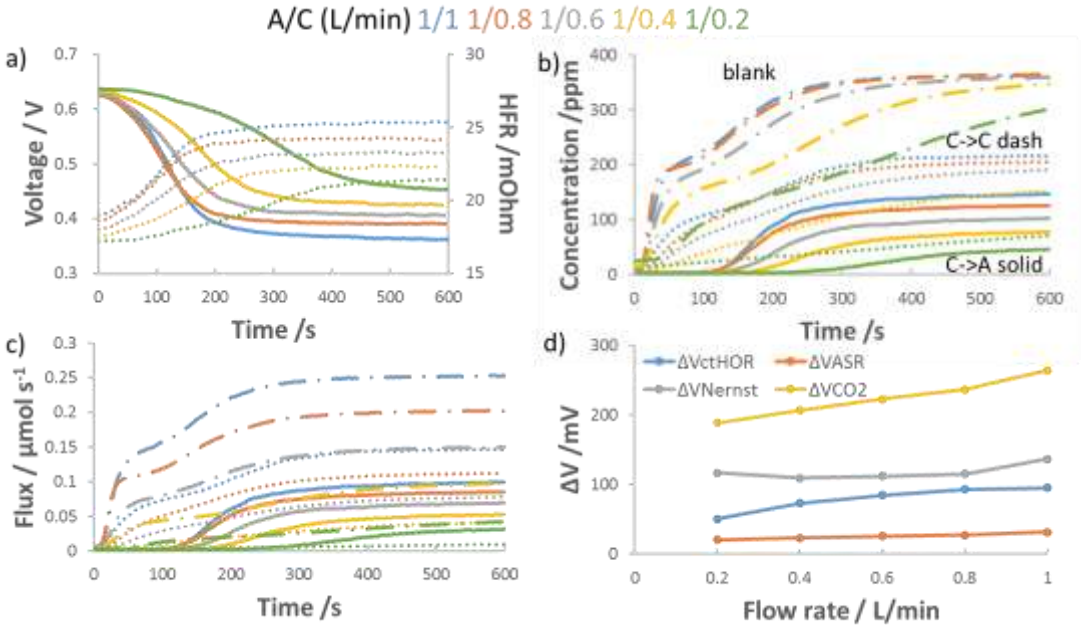

Figure 3.1 Effect of cathode flowrate on the carbonation of an AEMFC operating at 1 A/cm^2 and 60 ^{o}C with the LDPE-BTMA AEM, 400 ppm CO_2 fed to cathode at t = 0 s, 1 L/min anode flowrate, 5cm^2 active area. a) Voltage loss (solid lines) and HFR increase (dotted lines) following the introduction of CO_2 into the cathode; b) Concentration of CO_2 in the anode (solid lines) and cathode (dotted lines) effluent streams; c) CO_2 flux in the anode and cathode effluent; d) deconvoluted CO_2-related voltage losses. In panels a)-c), the results are color-coded based on flowrate, as indicated at the top of the figure. In panels b) and c), the cathode "blank" plots are shown by combination dash-dot lines.

Table 3.1 Degree of steady-state carbonation as function of cathode flowrate feeding with 400 ppm CO_2.

Anode/Cathode Flowrate (L/min)	**1 /1**	**1/0.8**	**1/0.6**	**1/0.4**	**1/0.2**
AEMFC carbonate N_{CO2} / µmol	21 ± 3	17 ± 2	13 ± 2	8 ± 2	4 ± 2
Anode carbonate / µmol	8 ± 2	7 ± 2	7 ± 2	8 ± 2	8 ± 2

breakthrough time in the anode exhaust was longer at lower flowrates. This shows that CO_2 accumulation is slower in the AEMFC anode at lower flowrate, that is the flux of carbonate across the cell is lower. The data also shows that the flux of CO_2 leaving the anode (Figure 3.1c) at steady state is lower at lower flowrate; hence, the rate of CO_2 uptake at the cathode is also less at lower flowrate.

It might be thought that combining the lower rate of anode carbonate accumulation combined with a lower incoming flux would reduce the amount of carbonate in the anode during cell operation. However, the release of CO_2 requires the accumulation carbonates in the anode. Eventually the number of supplied carbonate ions result in a sufficiently high carbonate concentration at the anode such that the reverse of Equations 1.3-1.4 occurs. The speciation shifts from CO_3^{2-} to HCO_3^- and then finally CO_2. Because CO_2 release is always observed at the anode, it is possible that the anode carbonate concentration may not be significantly different across the range of flowrates. To estimate the total amount of carbonate in the anode electrode, the CO_2 was removed from the cathode feed until the cell reached a new steady state. The resulting cell was then pulsed to 0.1 V and the amount of CO_2 in the anode exhaust was measured versus time. The integral of the CO_2 concentration vs. time can be used as an estimate total amount of carbonate left in the cell, which, after the new steady state, should overwhelmingly be in the anode.[53] These values are also reported in Table 1 where it was found that the total amount of anode carbonate was nearly unchanged with cathode flowrate. This effect of AEMFC N_{CO2} vs. total amount of anode carbonate also has implications on the individual contributions to the CO_2-related voltage loss, discussed above. However, before deconvoluting the effect of the cathode flowrate on the root causes for cell voltage loss, it is important to point out from Figure 3.1b that

AEM-like devices can also act as CO_2-separators which can simultaneously generate energy, unlike traditional approaches which consume energy.

Though Figure 3.1a is informative, data following the release of CO_2 is needed in order to deconvolute the CO_2-related voltage loss into its fundamental constituents: ΔASR, ΔV_{Nernst} and ΔR_{ctHOR}. That raw data is shown in Figures 3.3 – 3.7 and the quantified values for ΔASR, ΔV_{Nernst} and ΔR_{ctHOR} are presented in Table 3.2. Figure 3.1d graphically display the results of the deconvolution. In Figure 3.1d, ΔASR increased almost linearly with the cathode flowrate, and the total amount of carbonate in the cell shown in Table 3.1. ΔR_{ctHOR} increased with flowrate as the amount of carbonate in the cell increased, with the smallest increase at the lowest flowrates. Figure 3.1d presents ΔV_{Nernst} as a function of cathode flowrate as well as the voltage loss caused by the other two mechanisms, allowing ΔV_{Nernst}, ΔV_{ASR} ($\Delta V_{ASR}=i\Delta ASR$) and ΔV_{ctHOR} ($\Delta V_{ctHOR}=i\Delta R_{ctHOR}$) to be compared. Here, the overall voltage loss was dominated by the Nernstian loss and the increase in the charge transfer resistance. It should be noted that the Nernstian loss was the most significant, and was nearly constant regardless of the flowrate, which agrees well with the anode carbonation state in Table 3.1. This suggests that the outermost part of the anode, where the potential is measured experimentally, remains firmly dominated by the bicarbonate/CO_2 equilibrium at all flowrates. The next largest contributor to the cell performance loss was the charge transfer resistance. It was also the most affected by flowrate. For completeness, Figure 3.8 and Table 3.5 show the cathode flowrate effect with a GT-64-15 AEM as well, which showed the same behavior.

Next, the effect of lowering the anode reacting gas flowrate was investigated and the results are shown in Figure 3.2. In general, the anode flowrate did not have a significant

impact on the CO_2-related overpotential. Figure 3.2a shows that the CO_2 overpotential only very slightly increased with decreasing H_2 flowrate. This was not due to a significant increase in the amount of carbonate in the system, as evidenced by the similar HFR for all cases and the total cell carbonation being similar (Table 3.2). This suggests that the main reason for increased polarization is increased carbonate concentration in the anode, particularly right at the anode/GDL interface, which is evidenced by larger Nernstian and charge transfer losses at lower flowrates as well as the semi-quantitative measurement of anode CO_2 content (using the procedure described above for the cathode) as summarized in Table 3.2.

It was observed that as the anode flowrate was decreased, the CO_2 concentration in the anode exhaust increased, which is shown in Figure 3.2b. In fact, it was possible for the concentration of CO_2 in the anode exhaust to be significantly higher than the CO_2 concentration in the cathode feed, showing that these devices can act as CO_2 concentrators. It was also observed that the cathode exhaust nearly always contains 200 ppm CO_2 regardless of the H_2 flowrate, showing that the extent of carbonation near the cathode was very low, and suggesting that the cathode likely sees minimal resistance to CO_2 uptake and carbonate formation. The carbonate uptake and flux across the cell was essentially independent of anode flowrate (Figure 3.2c) because of the rapid reaction between carbon dioxide and hydroxide. Finally, as described above, the polarization losses were deconvoluted from the data where CO_2 was supplied and removed from the cathode (Figure 3.10 - 14). As shown in Figure 3.2d, none of the three major contributors to the CO_2-related overpotential changed significantly as the anode flowrate was changed.

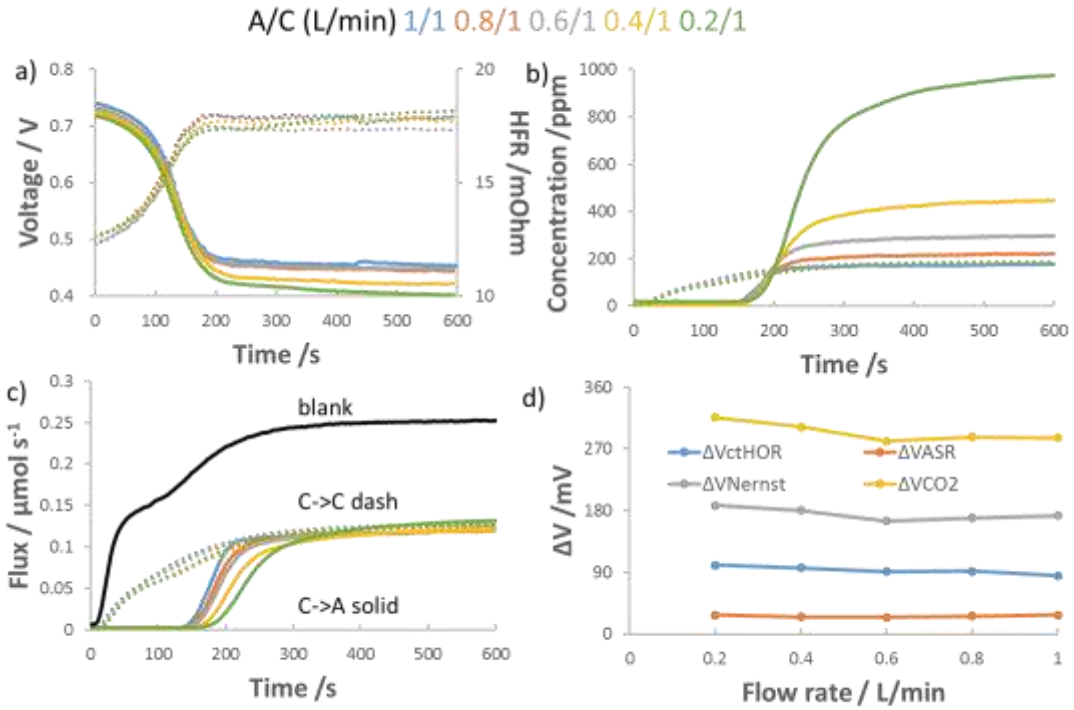

Figure 3.2 Anode flowrate effect on AEMFC carbonation and performance loss. AEMFC operating at 1 A/cm^2 and 60 ^{o}C with a LDPE-BTMA AEM, 400 ppm CO_2 fed to cathode at t = 0 s, 1 L/min anode flowrate, 5 cm^2 active area. a) Voltage loss (solid lines) and HFR increase (dotted lines) following the introduction of CO_2 into the cathode; b) Concentration of CO_2 in the anode (solid lines) and cathode (dotted lines) effluent streams; c) CO_2 flux leaving the anode and cathode; and d) deconvoluted CO_2-related voltage losses.

Table 3.2 Degree of steady-state carbonation as function of anode flowrate feeding with 400 ppm CO_2.

Anode/Cathode Flowrate (L/min)	**1 /1**	**0.8/1**	**0.6/1**	**0.4/1**	**0.2/1**
AEMFC carbonate / µmol	19 ± 2	20 ± 2	20 ± 2	27 ± 3	24 ± 4
Anode carbonate / µmol	11 ± 2	11 ± 6	14 ± 4	14 ± 2	18 ± 2

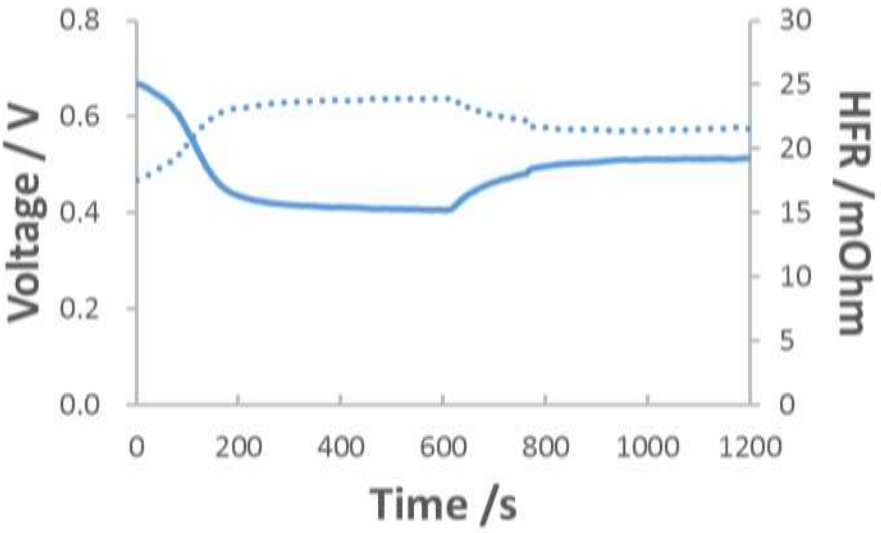

Figure 3.3 Voltage and HFR changes during CO_2 dosing (within 600 s) and removing CO_2 after 600 s; voltage: solid line, HFR: dash line; anode flowrate 1 L/min, cathode flowrate 1 L/min. AEMFC operating at 1 A/cm^2 and 60 ^{o}C with 25 um LDPE AEM, 400 ppm CO_2 was fed to cathode.

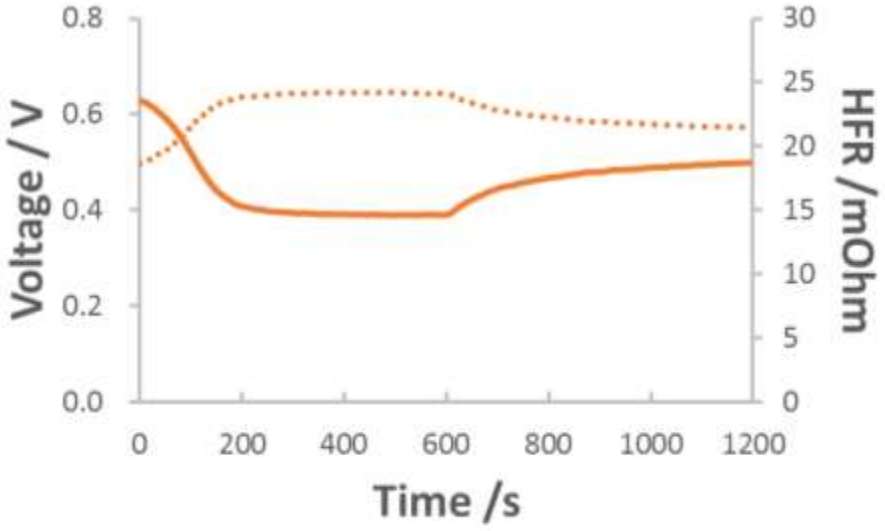

Figure 3.4 Voltage and HFR changes during CO_2 dosing (within 600 s) and removing CO_2 after 600 s; voltage: solid line, HFR: dash line; anode flowrate 1 L/min, cathode flowrate 0.8 L/min. AEMFC operating at 1 A/cm^2 and 60 ^{o}C with 25 um LDPE AEM, 400 ppm CO_2 was fed to cathode.

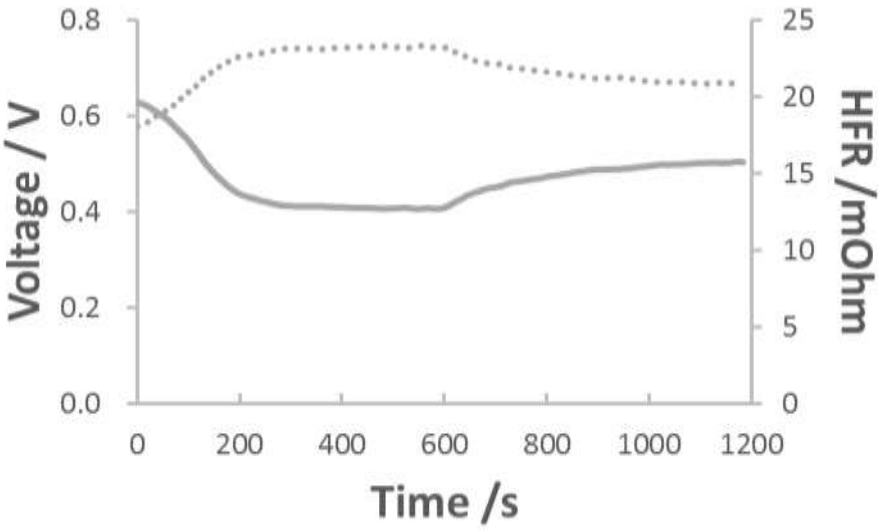

Figure 3.5 Voltage and HFR changes during CO_2 dosing (within 600 s) and removing CO_2 after 600 s; voltage: solid line, HFR: dash line; anode flowrate 1 L/min, cathode flowrate 0.6 L/min. AEMFC operating at 1 A/cm^2 and 60 ^{o}C with 25 um LDPE AEM, 400 ppm CO_2 was fed to cathode.

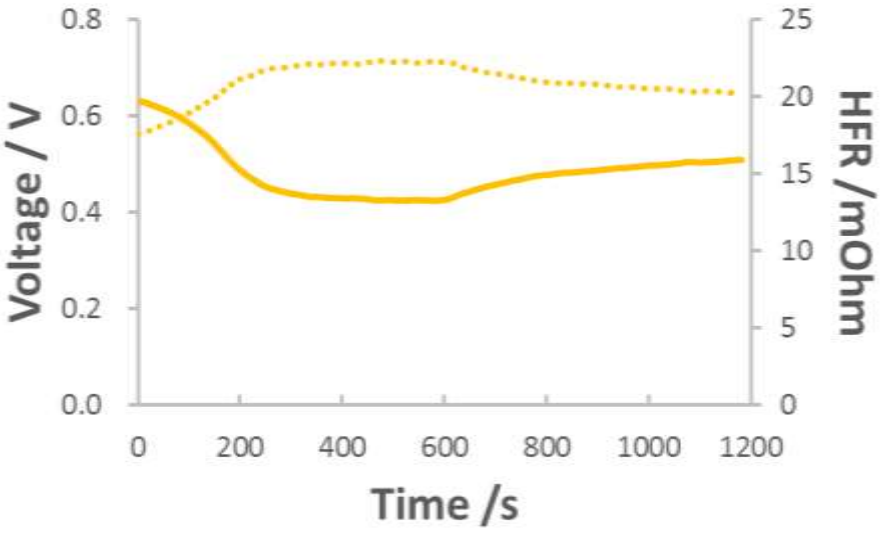

Figure 3.6 Voltage and HFR changes during CO_2 dosing (within 600 s) and removing CO_2 after 600 s; voltage: solid line, HFR: dash line; anode flowrate 1 L/min, cathode flowrate 0.4 L/min. AEMFC operating at 1 A/cm^2 and 60 ^{o}C with 25 um LDPE AEM, 400 ppm CO_2 was fed to cathode.

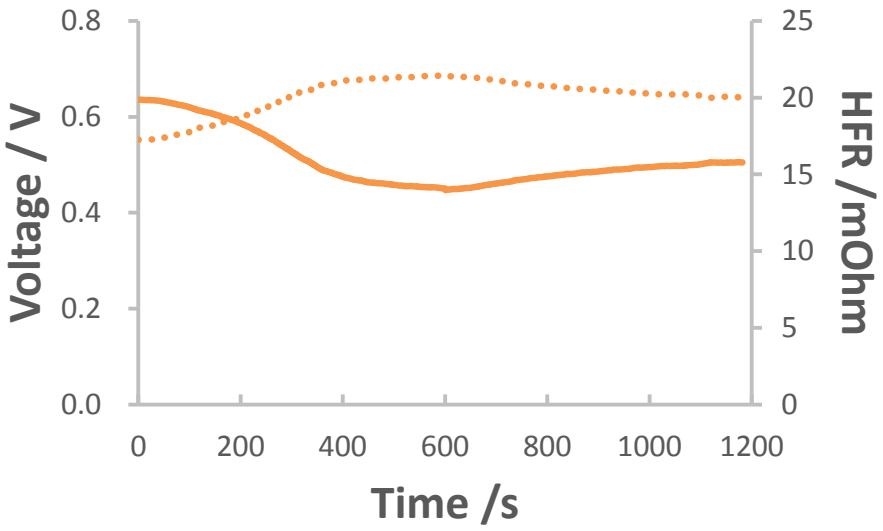

Figure 3.7 Voltage and HFR changes during CO_2 dosing (within 600 s) and removing CO_2 after 600 s; voltage: solid line, HFR: dash line; anode flowrate 1 L/min, cathode flowrate 0.2 L/min. AEMFC operating at 1 A/cm^2 and 60 ^{o}C with 25 um LDPE AEM, 400 ppm CO_2 was fed to cathode.

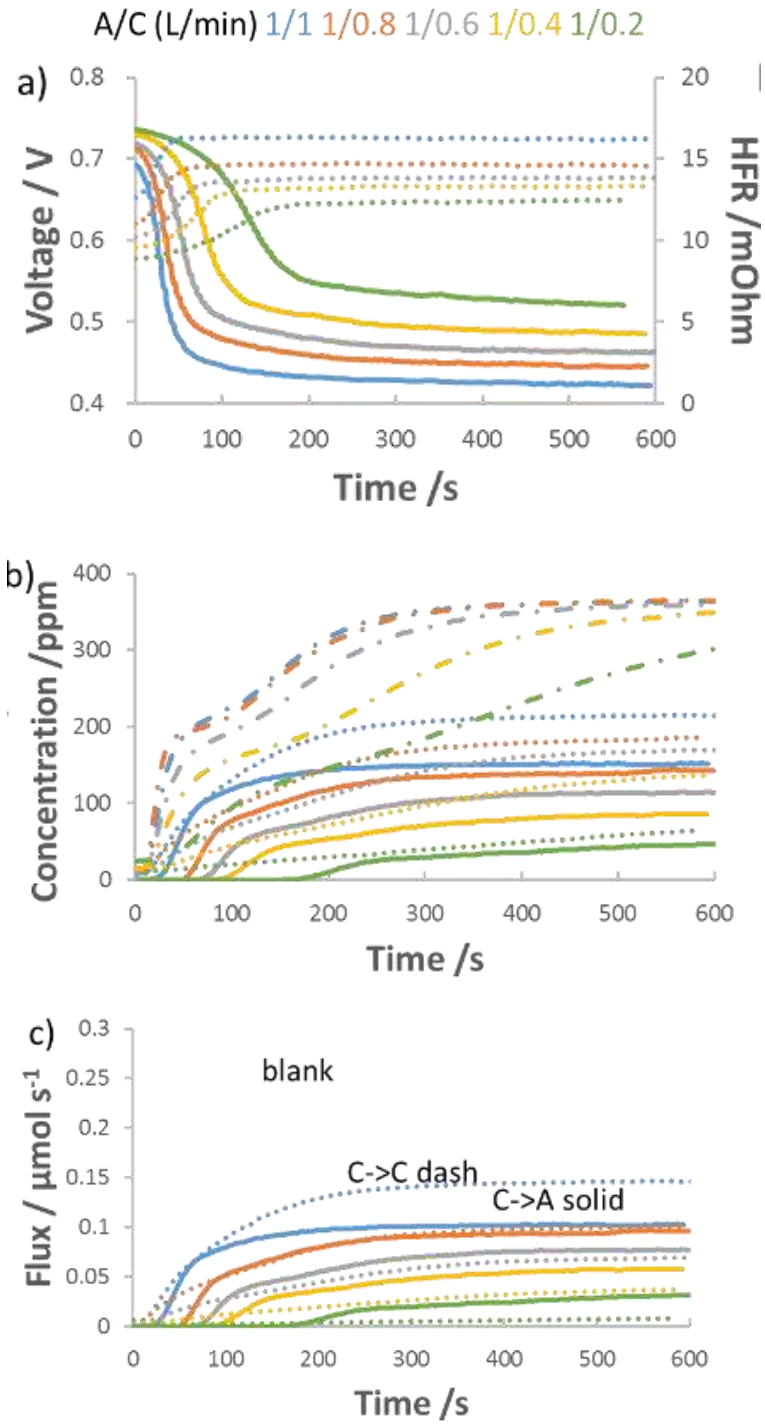

Figure 3.8 Effect of cathode flowrate on the carbonation of an AEMFC operating at 1 A/cm^2 and 60 ºC with the GT-64-15 AEM, 400 ppm CO_2 fed to cathode at t = 0 s, 1 L/min anode flowrate, 5cm^2 active area. a) Voltage loss (solid lines) and HFR increase (dotted lines) following the introduction of CO_2 into the cathode; b) Concentration of CO_2 in the anode (solid lines) and cathode (dotted lines) effluent streams; c) CO_2 flux in the anode and cathode effluent

Table 3.3 Deconvonlution of flowrate effect experiments.

Cathode flowrate (L/min)	ΔV_{CO2} (mV)	before (V)	after (V)	cutoff (V)	ΔV_{ctHOR} (mV)	ΔR_{ctHOR} (mΩ)	ΔASR (mΩ*cm^2)	before (mΩ)	after (mΩ)	cutoff (mΩ)	ΔASR' (mΩ*cm^2)	ΔV_{Nernst} (mV)	ΔV_{ASR} (mV)
1	264	0.67	0.406	0.513	95.5	19.1	31.8	17.58	23.94	21.64	11.5	136.7	31.8
0.8	237	0.628	0.391	0.498	93.5	18.7	27.85	18.64	24.21	21.51	13.5	115.65	27.85
0.6	223	0.629	0.406	0.503	84.8	16.96	26.15	18.02	23.25	20.81	12.2	112.05	26.15
0.4	207	0.632	0.425	0.509	73.55	14.71	23.6	17.63	22.35	20.26	10.45	109.85	23.6
0.2	189	0.636	0.447	0.505	50.95	10.19	20.9	17.26	21.44	20.03	7.05	117.15	20.9
Anode/Cathode flowrate (L/min)													
0.8	237	0.631	0.394	0.506	98.7	19.74	25.1	17.32	22.34	19.68	13.3	113.2	25.1
0.6	237	0.657	0.42	0.518	87.25	17.45	25.75	16.19	21.34	19.19	10.75	124	25.75
0.4	242	0.685	0.443	0.523	72	14.4	27.65	15.2	20.73	19.13	8	142.35	27.65
Anode flowrate (L/min)													
1	286	0.74	0.454	0.547	84.9	16.98	28.15	12.29	17.92	16.3	8.1	172.95	28.15
0.8	287	0.731	0.444	0.545	91.55	18.31	26.1	12.64	17.86	15.97	9.45	169.35	26.1
0.6	281	0.729	0.448	0.548	91.3	18.26	24.8	12.38	17.34	15.6	8.7	164.9	24.8
0.4	302	0.724	0.422	0.528	96.55	19.31	25.05	12.69	17.7	15.81	9.45	180.4	25.05
0.2	316	0.718	0.402	0.513	100.55	20.11	27.75	12.62	18.17	16.08	10.45	187.7	27.75

The final flowrate-related experiment involved lowering the flowrates of both the anode and cathode gases simultaneously and equally. As shown in Figure 3.9a, the voltage and HFR showed similar behavior to Figure 3.1a as CO_2 is applied. It is noted that the initial operating voltage is different in each case due to performance differences at lower reacting gas flowrates; low flowrates can make it more difficult to manage the AEMFC water production at the anode and this has an effect on the cell performance[24,89]. In fact, in these cells, stable operation at 0.2 L/s was not possible and is, thus, not reported here. There were some notable CO_2-related cell dynamics at this condition that were not obvious by looking at the data in Figures 3.1 and 3.2. For instance, in Figure 3.9b, the amount of CO_2 in the exhausts were comparable, suggesting a balance between the dosing and removal. In addition, Figure 3.9c shows higher flux at reasonably higher flowrates. But the most surprising observations were made after deconvoluting the data sets where CO_2 was first applied and then released (shown in Figure 3.15 – 3.17) to determine the contribution of each of the fundamental causes of CO_2-related voltage loss. The Nernstian, Ohmic and kinetic losses from the addition of CO_2 at various identical anode/cathode flowrates are summarized in Figure 3.9d. Despite the dynamics in the CO_2 flux (Figure 3.9c) at various flowrates, lowering the flowrates symmetrically did not significantly impact the total CO_2-derived overpotentials nor did it drastically change any individual contributor, though there does seem to be some interplay between ΔR_{ctHOR} and ΔV_{Nernst} where the former slightly increases with flowrate and the latter decreases. This can be understood based on the dynamics of the system where despite the fact that lower cathode flowrates reduce the dosing of the cell, the lower anode flowrate makes it more difficult to remove carbonate from the system. Thus, at lower flowrates, as summarized in Table 3,

despite similar overall amounts of carbonate in the system, the anode itself appears to have a higher total amount of CO_2 at lower flowrate than at higher flowrate, which is expected to increase the charge transfer resistance. The Nernstian voltage loss did slightly increase with decreasing flowrates, which is most likely the result of carbonate accumulation in regions of the cell other than the anode. This causes the pH difference between the anode and cathode to be less at lower flowrates than higher flowrates. Figure 3.28 and Table 3.5 show the same flowrate effect with a different membrane, GT-64-15, which again showed the same behavior.

3.2.2 EFFECT OF HYDRATION ON THE PERFORMANCE OF AEMFC OPERATING WITH 400 PPM CO2

Another variable that may influence the CO_2 uptake in the AEM cell is cell hydration. There are multiple ways to manipulate the amount of water in the cell. One way is to change the dew point of the anode and cathode reacting gases. The results of doing so on the CO_2-related voltage loss is shown in Figure 3.19a and summarized in Table 3.6. At low to intermediate dew point values, the total CO_2-related overpotential very slightly decreased with increased hydration (evidenced the by the lower HFR in Table 3.6). As the dew points were increased, the concentration and flux of CO_2 in the anode exhaust decreased while the concentration leaving the cathode increased, shown in Figure 3.19b-c. This appears to confirm that increasing the amount of free water in the cell slightly lowers CO_2 uptake in the cathode. The presence of this free water most likely leads to a dilution effect, where the environment is made less basic in nature, decreasing the CO_2 solubility. At the highest dew point settings, the total CO_2 overpotential was low, but this was subject

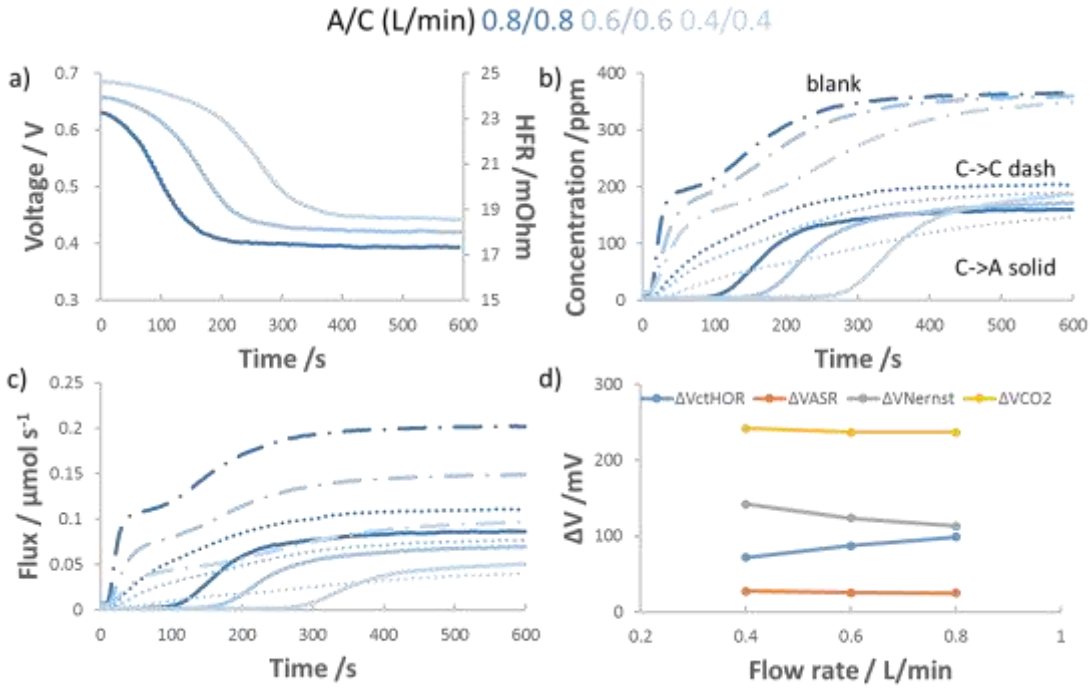

Figure 3.9 Effect of symmetrically reducing the anode and cathode flowrate on AEMFC carbonation. All cells were operated at 1 A/cm^2 and 60 ^{o}C with 25 um LDPE-BTMA AEM, 5cm^2 active area. The concentration of CO_2 fed to the cathode was 400 ppm CO_2 applied at t = 0 s. a) voltage losses and HFR increases after the introduction of CO_2, b) CO_2 emission from the anode (solid lines) and cathode (dotted lines); c) CO_2 flux; and d) deconvoluted CO_2 related voltage losses at the investigated symmetrical flowrates.

Table 3.4 Degree of steady-state carbonation as function of anode/cathode flowrate feeding with 400 ppm CO_2.

Anode/Cathode Flowrate (L/min)	**0.8/0.8**	**0.6/0.6**	**0.4/0.4**
AEMFC carbonate/ µmol	15 ± 4	14 ± 4	15 ± 3
Anode carbonate / µmol	8 ± 3	9 ± 2	11 ± 2

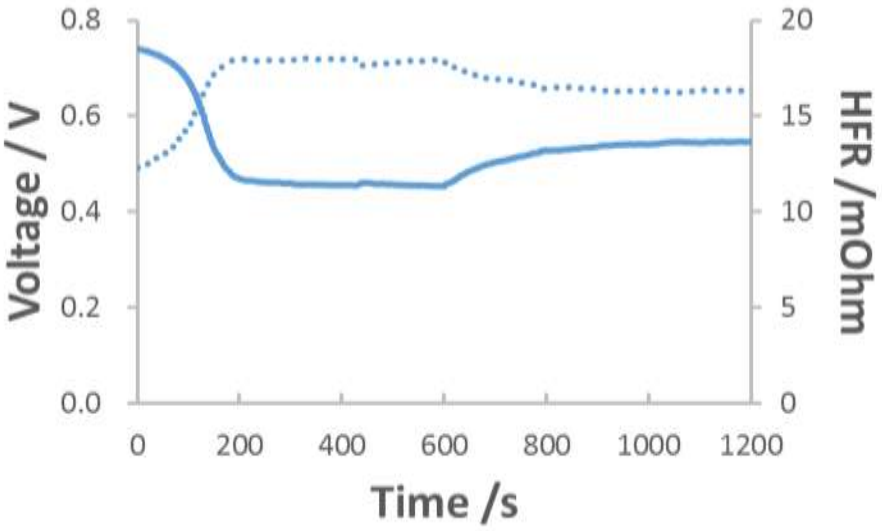

Figure 3.10 Voltage and HFR changes during CO_2 dosing (within 600 s) and removing CO_2 after 600 s; voltage: solid line, HFR: dash line; anode flowrate 1 L/min, cathode flowrate 1 L/min. AEMFC operating at 1 A/cm^2 and 60 ^{o}C with 25 um LDPE AEM, 400 ppm CO_2 was fed to cathode.

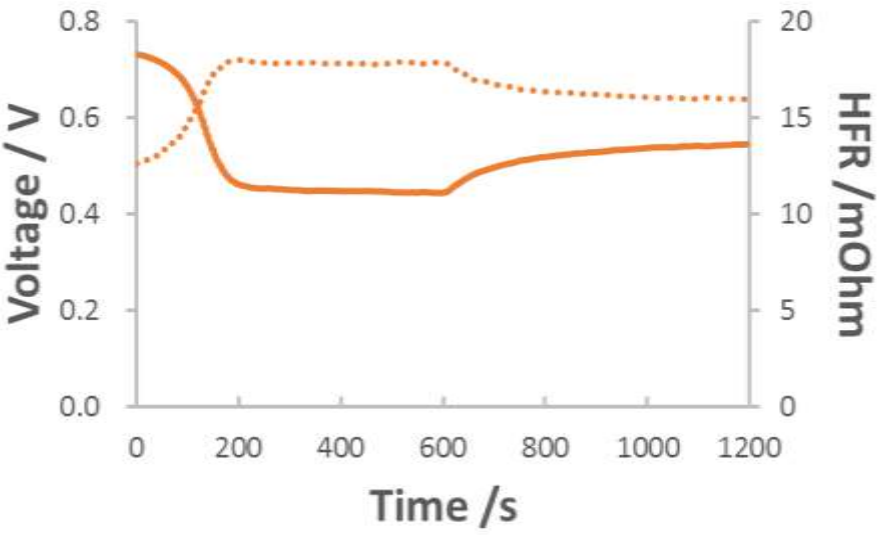

Figure 3.11 Voltage and HFR changes during CO_2 dosing (within 600 s) and removing CO_2 after 600 s; voltage: solid line, HFR: dash line; anode flowrate 0.8 L/min, cathode flowrate 1 L/min. AEMFC operating at 1 A/cm^2 and 60 ^{o}C with 25 um LDPE AEM, 400 ppm CO_2 was fed to cathode.

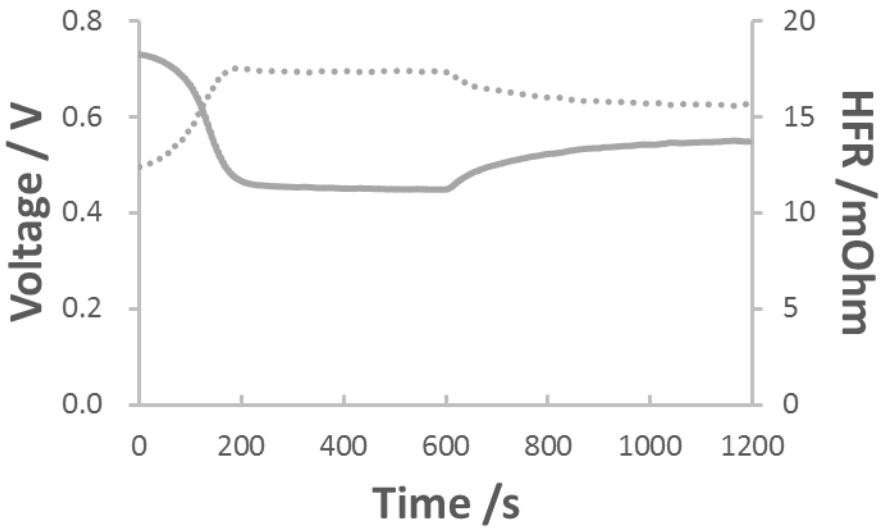

Figure 3.12 Voltage and HFR changes during CO_2 dosing (within 600 s) and removing CO_2 after 600 s; voltage: solid line, HFR: dash line; anode flowrate 0.6 L/min, cathode flowrate 1 L/min. AEMFC operating at 1 A/cm^2 and 60 ^{o}C with 25 um LDPE AEM, 400 ppm CO_2 was fed to cathode.

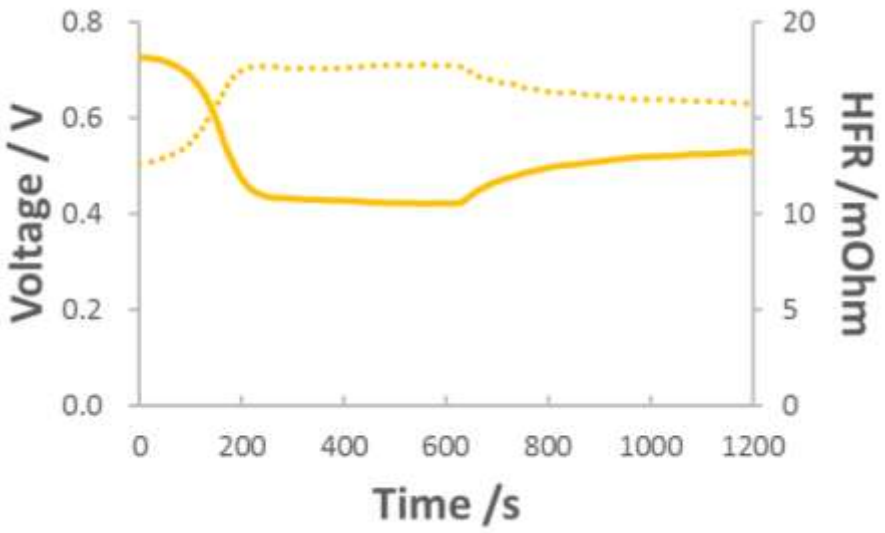

Figure 3.13 Voltage and HFR changes during CO_2 dosing (within 600 s) and removing CO_2 after 600 s; voltage: solid line, HFR: dash line; anode flowrate 0.4 L/min, cathode flowrate 1 L/min. AEMFC operating at 1 A/cm^2 and 60 ^{o}C with 25 um LDPE AEM, 400 ppm CO_2 was fed to cathode.

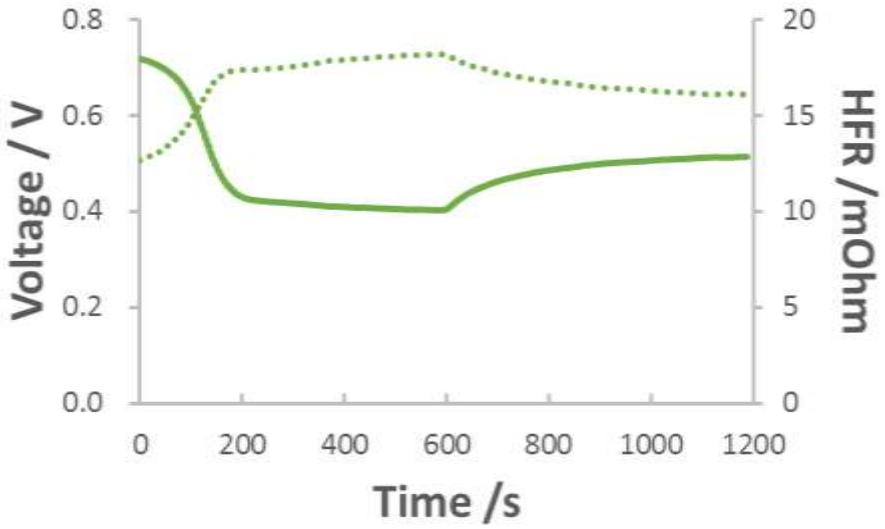

Figure 3.14 Voltage and HFR changes during CO_2 dosing (within 600 s) and removing CO_2 after 600 s; voltage: solid line, HFR: dash line; anode flowrate 0.2 L/min, cathode flowrate 1 L/min. AEMFC operating at 1 A/cm^2 and 60 ^{o}C with 25 um LDPE AEM, 400 ppm CO_2 was fed to cathode.

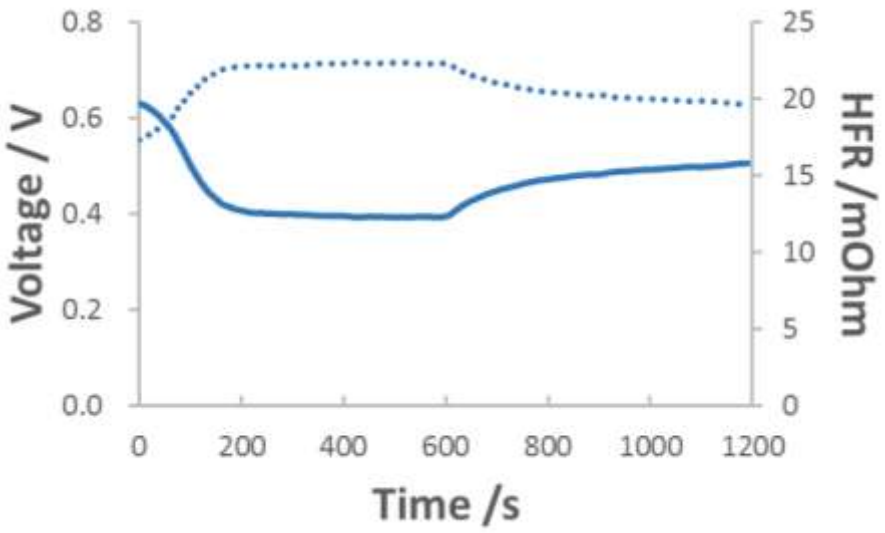

Figure 3.15 Voltage and HFR changes during CO_2 dosing (within 600 s) and removing CO_2 after 600 s; voltage: solid line, HFR: dash line; anode flowrate 0.8 L/min, cathode flowrate 0.8 L/min. AEMFC operating at 1 A/cm^2 and 60 ^{o}C with 25 um LDPE AEM, 400 ppm CO_2 was fed to cathode.

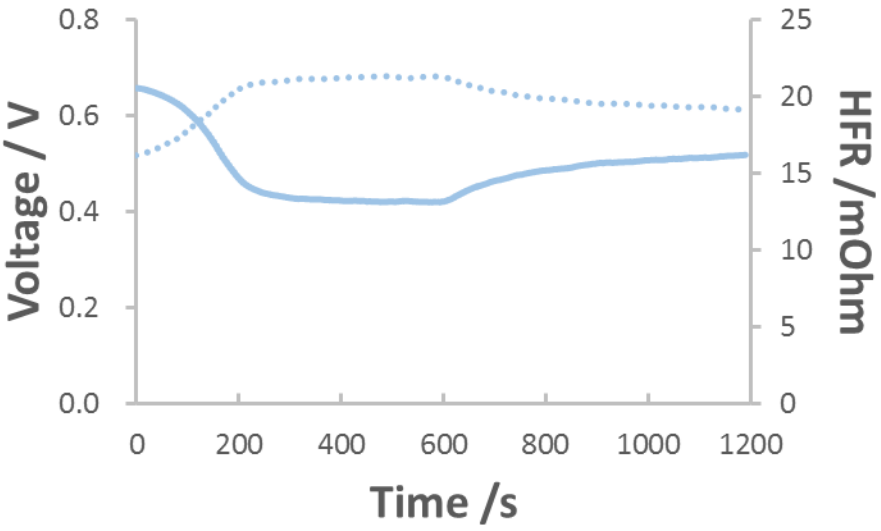

Figure 3.16 Voltage and HFR changes during CO_2 dosing (within 600 s) and removing CO_2 after 600 s; voltage: solid line, HFR: dash line; anode flowrate 0.6 L/min, cathode flowrate 0.6 L/min. AEMFC operating at 1 A/cm^2 and 60 ^{o}C with 25 um LDPE AEM, 400 ppm CO_2 was fed to cathode.

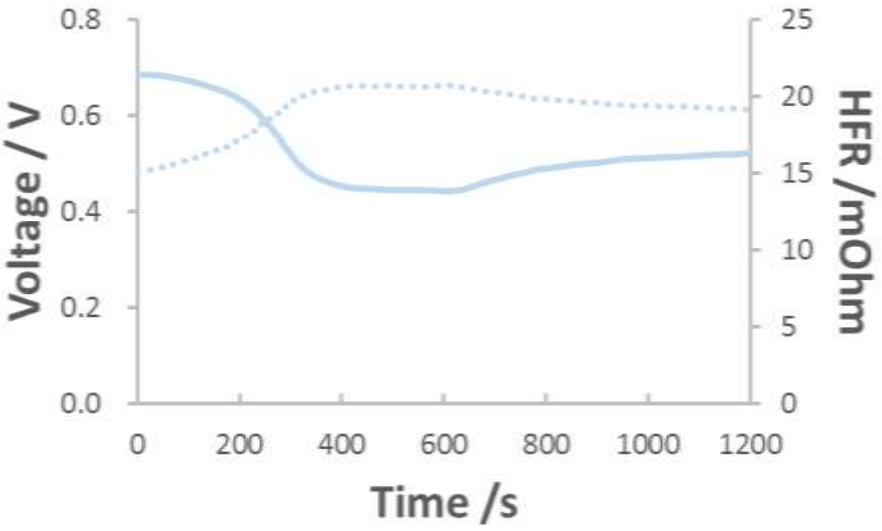

Figure 3.17 Voltage and HFR changes during CO_2 dosing (within 600 s) and removing CO_2 after 600 s; voltage: solid line, HFR: dash line; anode flowrate 0.4 L/min, cathode flowrate 0.4 L/min. AEMFC operating at 1 A/cm^2 and 60 ^{o}C with 25 um LDPE AEM, 400 ppm CO_2 was fed to cathode.

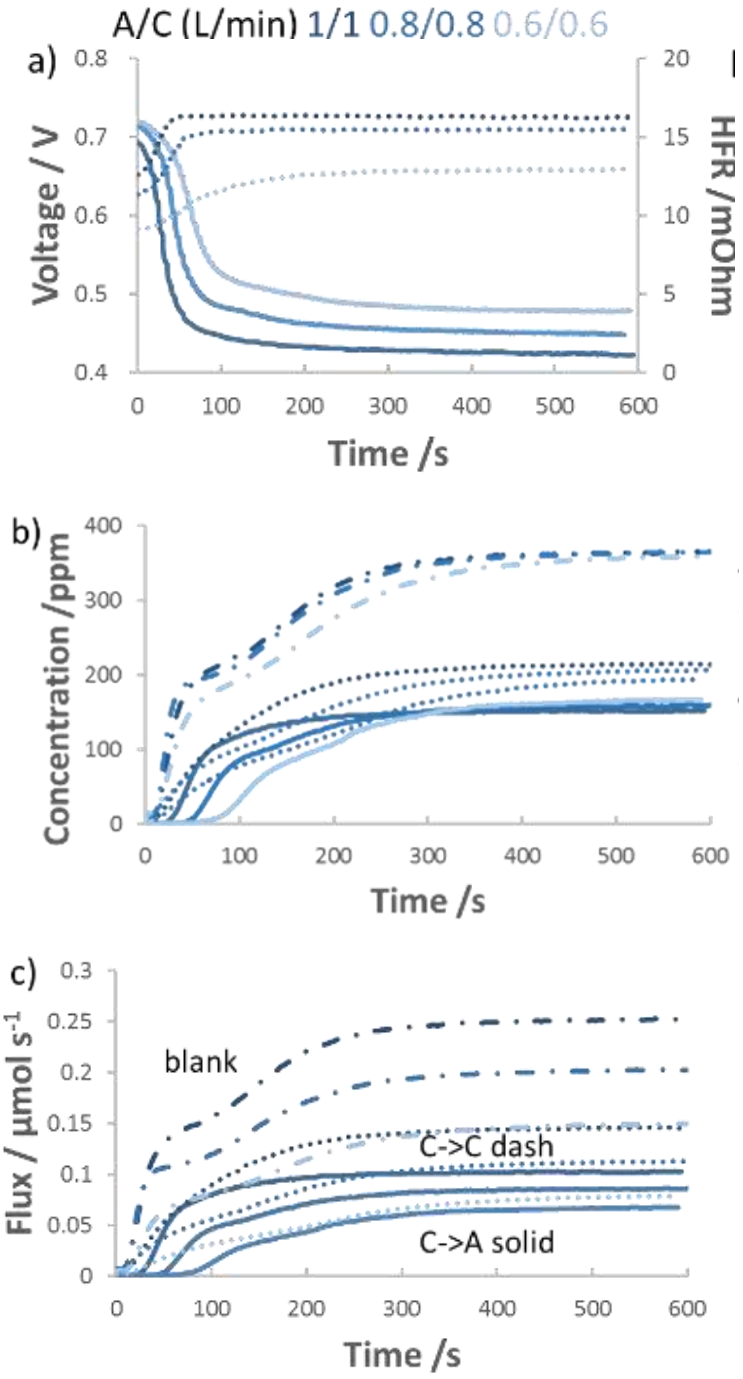

Figure 3.18 Effect of cathode flowrate on the carbonation of an AEMFC operating at 1 A/cm^2 and 60 ºC with the GT-64-15 AEM, 400 ppm CO_2 fed to cathode at t = 0 s, 5cm^2 active area. a) Voltage loss (solid lines) and HFR increase (dotted lines) following the introduction of CO_2 into the cathode; b) Concentration of CO_2 in the anode (solid lines) and cathode (dotted lines) effluent streams; c) CO_2 flux in the anode and cathode effluent.

Table 3.5 Degree of steady-state carbonation with GT-64-15 AEM as function of cathode flowrate feeding with 400 ppm CO_2.

Anode/Cathode Flowrate (L/min)	**1/1**	**1/0.8**	**1/0.6**	**1/0.4**	**1/0.2**	**0.8/0.8**	**0.6/0.6**
AEMFC carbonate N_{CO2} / µmol	10 ± 1	9 ± 1	7 ± 1	3 ± 1	2 ± 1	8 ± 1	9 ± 1
Anode carbonate / µmol	2 ± 1	4 ± 1	4 ± 1	2 ± 1	1 ± 1	3 ± 1	2 ± 1

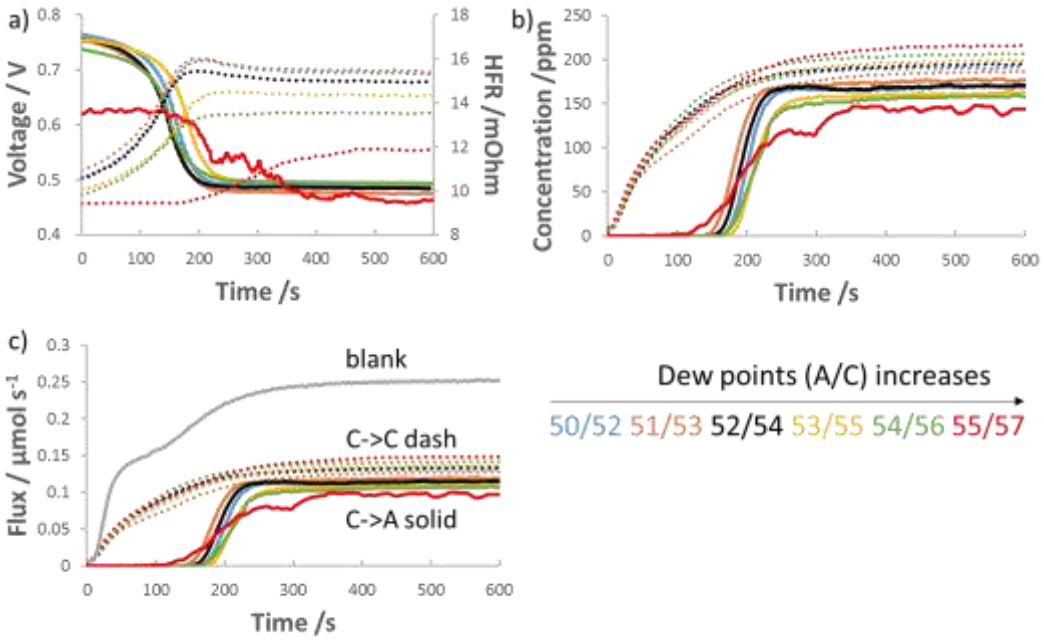

Figure 3.19 Effect of water content on the carbonation of AEMFCs operating at 1 A/cm^2 and 60 ^{o}C with ETFE-BTMA AEM, 5 cm^2 active area. 400 ppm CO_2 in O_2 was fed to cathode at t = 0 s, and UHP H_2 to the anode, both at a rate of 1 L/min. a) voltage loss and HFR increase as function of dew points (anode/cathode); b) CO_2 emission from the anode (solid lines) and cathode (dotted lines); c) CO_2 flux.

Table 3.6 Influence of hydration on the CO_2-related overpotential and degree of carbonation for an AEMFC operating at 60 ^oC.

Anode/Cathode Dew Points	**50/52**	**51/53**	**52/54**	**53/55**	**54/56**	**55/57**
CO_2 overpotential /V	0.277	0.277	0.272	0.261	0.244	0.151
△HFR / mOhm	4.73	4.43	4.37	4.21	3.72	2.66
AEMFC carbonate / µmol	17 ± 1	16 ± 1	14 ± 1	18 ± 1	15 ± 1	17 ± 1
Anode carbonate / µmol	16 ± 1	15 ± 1	17 ± 1	17 ± 1	17 ± 1	12 ± 1

to a tradeoff where the high hydration levels led to anode flooding (excess liquid water), which reduced overall cell performance and resulted in fluctuations in the cell voltage (cathode/anode dew points = 55/57 ^{o}C in Figure 3.19a).

A second pathway to change the water content of the cell is to manipulate the polymer itself. One way to do that is to vary the amount of water that can be taken up by the polymer, which can be done by changing its degree of crosslinking or the ratio of the monomers in the copolymer. To show this effect, the percentage of crosslinker in a GT-64 polynorbornene copolymer AEM was varied from 5% to 25%. As the degree of crosslinking is increased, the water uptake is reduced.[20] Therefore, in this study, the GT-64-5 AEM had the highest water content and GT-64-25 had the lowest water content. As shown in Figure 3.20a, the overall voltage loss decreased with increasing water content. GT-64-5, -15, and -25 AEMFCs showed overall CO_2-related the voltage losses of 254 mV, 292mV, and 300mV, respectively. Figures 3.19 and 3.20 confirm that increasing the water contents in an operating AEMFC helps reduce the CO_2-related performance penalty. Figure 3.20b reports the CO_2 concentrations in the anode and cathode effluents for the GT-64 AEMs with varied crosslinking. Interestingly, the overall amount of CO_2 taken up by the cell does not appear to be significantly changed by the crosslinker content. But, the lower crosslinker content (higher water content) did have a clear effect on the HFR and voltage loss. This suggests that the membrane water can influence the cell behavior even if the total CO_2 content of the cell is similar.

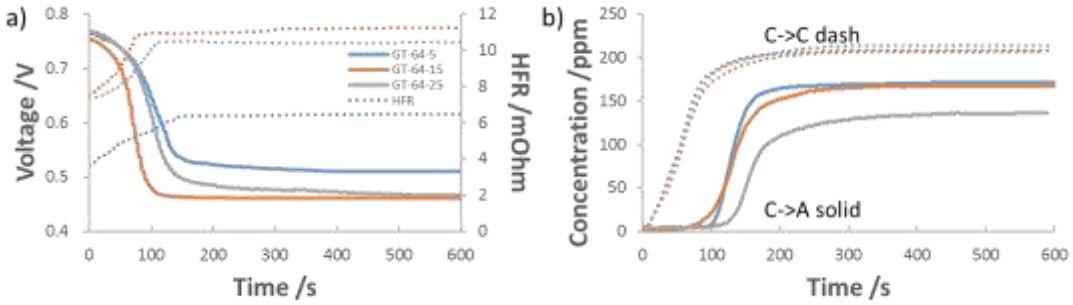

Figure 3.20 Influence of water uptake on AEMFC carbonation for cells operated at 1 A/cm^2 and 74/74/80 ºC (A/C/cell) with 10 µm thick GT-64-X AEMs. The GT-64-X AEMs contain increasing crosslinker content (5%, 15%, and 25%, denoted as X = 5, 15, 25, respectively). 400 ppm CO_2 was fed to cathode, 5 cm^2 active area. Specifically shown are a) voltage loss and HFR increase and b) CO_2 emission from the anode (solid lines) and cathode (dotted lines) as crosslinker content is increases.

3.2.3 OPTIMIZING OPERATING CONDITIONS TO MINIMIZE THE EFFECT OF CO_2 ON AEMFCS

The results above show that lower cathode flowrate (i.e. high ratio between the anode/cathode flowrate) and higher cell water content both contribute to lower total CO_2-related voltage loss. The experimental results in this work also agree with the modeling work by Gerhardt et al.[44] and Setzler et al.[90] who both showed that the degree of carbonation increased with decreased cathode flowrate. In addition to these two mechanisms, Chapter 2 [53] showed that higher operating current density, lower the CO_2 concentration, and higher temperature also lowered CO_2-related voltage losses. Therefore, a combination of the above advantageous conditions was deployed and a cell was operated at 80 ^oC, anode/cathode dew points of 78/80 ^oC, high anode flowrate at 1L/min and low cathode flowrate at 0.2 L/min. Then point-by-point data was recorded with varied CO_2 content in the cathode at a constant current density of 2 A/cm^2 (Figure 3.21a). Polarization curves were also recorded at several cathode CO_2 concentrations (Figure 3.21b).

As shown in Figure 3.21a, under these "optimized" conditions, operating an AEMFC with low CO_2 concentrations did not lead to catastrophic voltage losses. In fact, only a 30 mV voltage loss was observed with 5 ppm CO_2 in the cathode feed. When 400 ppm CO_2 oxygen was fed to the cathode, the total CO_2-related voltage loss was 182 mV, which is half of the previously reported value,[53] showing that the operating conditions are vitally important in dictating CO_2 tolerance. As the CO_2 concentration exceeded 100 ppm, there was an asymptotic behavior where increasing from 100 ppm to 400 ppm did not significantly affect the CO_2-related voltage losses. However, increasing the concentration of CO_2 in the cathode feed led to further decreases in the achievable mass transport limiting

current and peak power density. However, most AEMFCs (like most PEMFCs), would not actually be operated near the peak power density. Considering a more realistic operating point (2 A/cm^2 at 0.6 V) for various applications, including automotive, there was only *ca.* 20% reduction in the power density with 400 ppm CO_2 in the cathode gas compared to benchmark CO_2-free conditions. Some slightly lower concentrations (<100 ppm) have less than a 10% loss. This seems to provide some good news –that AEMFCs can be operated with CO_2 in the cathode stream, even at 400 ppm, without catastrophic performance losses. It is important to acknowledge that pure oxygen instead of air is being used here when the latter has reduced overall performance. The focus here is on the intrinsic effect of CO_2, justifying the use of O_2, but it is noted that the use of air is a more realistic operating condition for automotive and other applications.

3.3 SUMMARY

In this study, it experimentally shown in high performance AEMFCs that decreasing the total CO_2 dose to the cell (by decreasing the cathode flowrate) and increasing the level of hydration in an operating AEMFC are two possible pathways to lowering the CO_2-related voltage losses. Considering the fundamental mechanisms for CO_2-related voltage losses, the Nernstian contribution dominated voltage losses and was not affected by the gas flowrates. The next most important contributor to voltage loss was the anode charge transfer resistance, which increased with increasing O_2 flowrate and decreasing H_2 flowrate. The Ohmic resistance increased with increasing cathode flowrate, but was a minor overall contributor to cell performance losses. Lastly, a new set of optimal conditions, which lowered the total CO_2-related overpotentials to achieve practical current-voltage values

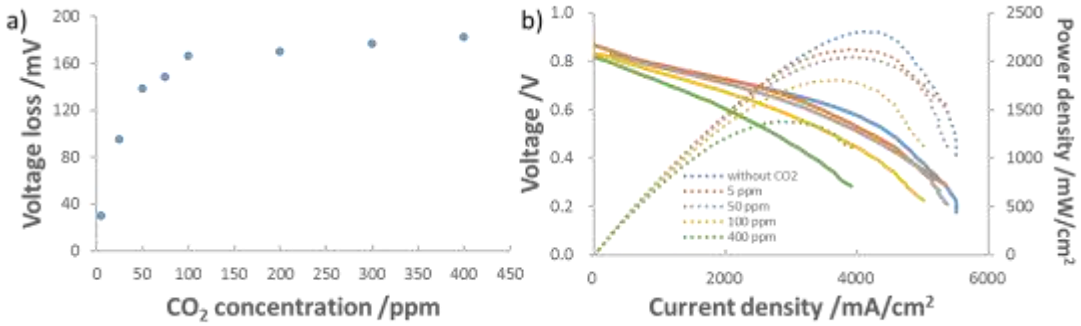

Figure 3.21 a) Voltage loss as function of CO_2 concentration at 2 A/cm^2 cell discharge; b) Power density curves for AEMFCs operated at various CO_2 concentrations in O_2, up to 400 ppm. The cell was operated at 80 ºC with anode/cathode dew points of 78/80 ºC. The anode flowrate was 1L/min and the cathode flowrate was 0.2 L/min. The membrane was HDPE-BTMA (ca. 30 µm thick when fully hydrated). 5 cm^2 active area.

was found and demonstrated. These insights will help both modeling groups and experimental researchers to better understand the operation of AEMFCs with CO_2 containing cathode feeds, as well as allow them to pose and assess new solutions.

It is also shown that AEM-like devices may be able to act as CO_2 separators that can simultaneously generate power. Finally, as the anode feed flowrate decreased, the CO_2 concentration in the anode increased to levels several times larger than the cathode inlet concentration, showing that these devices can act as energy-generating CO_2 concentrators.

CHAPTER 4: EFFECT OF MEMBRANE PROPERTIES ON THE CARBONATION OF ANION EXCHANGE MEMBRANE FUEL CELLS

Recently, anion exchange membrane fuel cell performance and stability have been enhanced to the point where their future deployment in real applications can be seriously considered. AEMFC peak power densities have been reported as high as 3.4 W/cm^2 operating on H_2/O_2 gas feeds [91] and 1.7 W/cm^2 operating on H_2/CO_2-free air [29]. In addition, multiple groups have reported 500+ h stability at low degradation rates (5–10%) [25,26,30] and one recent study showed durability over 2000 h with only a 3.65% voltage decay[29]. However, there remains one very serious issue that must be addressed: performance loss caused by exposure of operating cells to carbon dioxide, typically from the ambient air cathode feed. When CO_2 enters an operating AEMFC, it reacts with the OH^- anions in the polymer as well as those being continuously produced in the cathode from oxygen reduction (Equation 1.1) to form (bi)carbonates [7–9] (Equations 1.3 and 1.4).

Once the (bi)carbonate anions are formed, there are three primary mechanisms [44,53,54,88], all tied to the movement of the (bi)carbonate anions to the anode, that lead to a reduction in the operating voltage of the cell, which can amount to as much as 400 mV [42]. First, because hydrogen does not directly react with the (bi)carbonate anions arriving at the anode at typical operating potentials, they accumulate in the anode over time, lowering the pH. The drop in the anode pH leads to a thermodynamically driven increase in the anode

potential (ΔV_{Nernst}, typically 160–210 mV), decreasing the operating voltage. Second, accumulated (bi)carbonates lead to increased anode charge transfer resistance (ΔR_{ctHOR}) and higher kinetic overpotentials ($\Delta V_{ctHOR} = i \cdot \Delta R_{ctHOR}$, typically 50–100 mV). Third, (bi)carbonates have lower mobility than hydroxide, which lowers ionic conductivity and increases the area-specific resistance (ΔASR), leading to a corresponding voltage loss ($\Delta V_{ASR} = i \cdot \Delta ASR$, typically 10–20 mV). It is important to note that the impact of the increase in the ASR is generally a minor contributor (<10%) to the total CO_2-related operating voltage loss, which is dominated by the kinetic and thermodynamic effects discussed above [44,53]. Taking the three mechanisms for CO_2-related voltage loss into consideration, the operating voltage for an AEMFC upon exposure to CO_2 can be described by Equation 2.3 [53].

Recently, there have been several experimental [53,61,74,80–82] and modeling [43,44,63,70] studies focused on quantifying the effect of CO_2 on operating AEMFCs. Early work in this area suggested that the cumulative CO_2-related voltage losses might be too large to overcome and it might be necessary to almost completely remove carbon dioxide from the cathode air feed [53,74,80], which could be quite expensive and add system complexity. However, recent studies have identified several pathways by which the CO_2-related voltage penalty can mitigated [42,53,54,63] such as increasing the AEMFC operating current density, cell temperature and hydration level as well as decreasing the cathode flowrate. In high-performing AEMFCs, operating conditions have been found that minimize the CO_2-related voltage loss to only 30 mV with 5 ppm CO_2 in the cathode feed and 182 mV with 400 ppm CO_2 in the cathode feed [54]. However, there are no studies in the present literature that have systematically studied the effect of the AEM itself and there does not exist a fundamental

link between the AEM properties and the degree of AEMFC carbonation.

That being said, a tremendous amount of literature has been generated regarding membrane preparation and the investigation of the backbone chemistry [92–94], headgroup chemistry [65,95,96], and structure [97–99] on their electrochemical and mechanical properties [100–102]. Those electrochemical properties (especially hydroxide conductivity) are directly related to cell Ohmic resistance as well as the water uptake (WU) and transport. These can have an impact on the uptake of CO_2 and transport of carbonate in AEMFCs. Additionally, membrane thickness can be used to manipulate the transport of both ions and water in AEMFCs [21]. Because it has been shown that the accumulation and release of CO_2 is related to cell hydration and anode pH, it is very likely that the wise selection of AEMs may further allow AEMFCs to resist carbonation. Therefore, it is important to explore the impact of AEM physical and electrochemical properties on the tolerance of operating AEMFCs to the presence of CO_2 in the cathode feed.

In this study, the carbonation of AEMFCs assembled was investigated from a series of very high-performing AEMs from the literature with different chemistries and properties, including high-density polyethylene with a benzyltrimethylammonium cation (HDPE-BTMA) [103], low-density polyethylene with a benzyltrimethylammonium cation (LDPE-BTMA) [103], poly (norbornene) copolymers of GT72-5 [104], GT78-15 [91], GT64-15 [105], poly(aryl piperidinium) copolymer that possesses a terphenyl chain (PAP-TP-85) [86] (the full names for each AEM are defined in the Section 4.1.1). After cell startup and break-in, each of the AEMs are exposed to 400 ppm CO_2. During this time, the dynamics of cell carbonation are observed and the degree of carbonation and magnitude of the CO_2-related voltage loss are quantified. The results allow the effect of several variables on

AEM/AEMFC carbonation to be elucidated, including: AEM thickness, conductivity and crystallinity. Lastly, the carbonation of a 15 μm HDPE-BTMA AEM—with highest CO_2-related voltage loss—was investigated operando by neutron imaging in order to quantify the effect of adding CO_2 to the amount of liquid water in the MEA, which is the first time that the water content of a carbonated AEMFC has been imaged.

4.1 EXPERIMENTAL

4.1.1 MEMBRANE PROPERTIES AND OPERATION CONDITIONS

Eight AEMs were investigated in this study. Their structures and properties are summarized in Figure 4.1 and Table 4.1, respectively. The first two AEMs were radiation-grafted 15 μm or 25 μm low-density polyethylene with a benzyltrimethylammonium (LDPE-BTMA) stationary cation [66] The third AEM was a 15 μm radiation-grafted high-density polyethylene polymer with a BTMA cation (HDPE-BTMA) [103]. The fourth AEM was a 15 μm poly(aryl piperidinium) (PAP)-based copolymer. Both parts of the copolymer have primary repeat group that possesses a terphenyl (TP) chain. The AEM used here is denoted as PAP-TP-85, which means that a mole fraction of 0.85 of the copolymer contains the piperidinium group and a mole fraction of 0.15 does not [86].

The final family of four AEMs were based on cross-linked tetra-block poly(norbornene) (PNB) copolymers [104,105]. These AEMs were made from a combination of halogenated and non-halogenated monomers and a N,N,N', N'-tetramethyl-1, 6-hexanediamine (TMHDA) crosslinker. In the following discussion, these AEMs are denoted as GTXX-YY where XX indicates the percentage of the halogenated monomer and YY provides the mass fraction (in %) of the TMHDA. Therefore, a GT78-15 AEM comprises 78% halogenated monomer

and 15% crosslinker. Two GT78-15 (10 μm and 20 μm thickness), one GT64-15 (10 μm) and one GT72-5 (10 μm) AEMs were studied.

The optimized reacting gas dew points were very repeatable from cell to cell for the same membrane; but to keep consistent hydration level across all cells, the dew points were typically maintained as: (i) 72 °C at the anode and 72 °C at the cathode for an AEMFC operating at 80 °C or (ii) 50 °C at the anode and 52 °C at the cathode for an AEMFC operating at 60 °C. Following the optimization of the reacting gas dew points, the cells were operated galvanostatically at 0.2 A cm^{-2}. They were allowed to equilibrate for at least 30 min before CO_2 exposure was initiated. Multiple cells were constructed and tested for each measurement.

4.1.2 WIDE ANGLE X-RAY SCATTERING ANALYSIS

X-ray experiments were conducted using a SAXSLab Ganesha (SAXSLab, Holyoke, MA, USA) at the South Carolina SAXS Collaborative. A Xenocs GeniX 3D (Xenocs, Grenoble, France) microfocus source was used with a copper target to produce a monochromatic beam with a wavelength of 0.154 nm. The instrument was calibrated just prior to use with the National Institute of Standards and Technology reference material, 640 d silicon powder with the peak position of 2θ = 28.44°, where 2θ refers to the total scattering angle. A Pilatus 300 k detector (Dectris, Baden-Daettwil, Switzerland) was used to collect the two-dimensional (2D) scattering pattern with nominal pixel dimensions of 172 μm × 172 μm. The SAXS data were acquired with an X-ray flux of~40 million photons per second incident upon the sample at a sample-to-detector distance of 104.5 mm. The 2D images were azimuthally integrated to yield the scattering vector and intensity. Crystalline

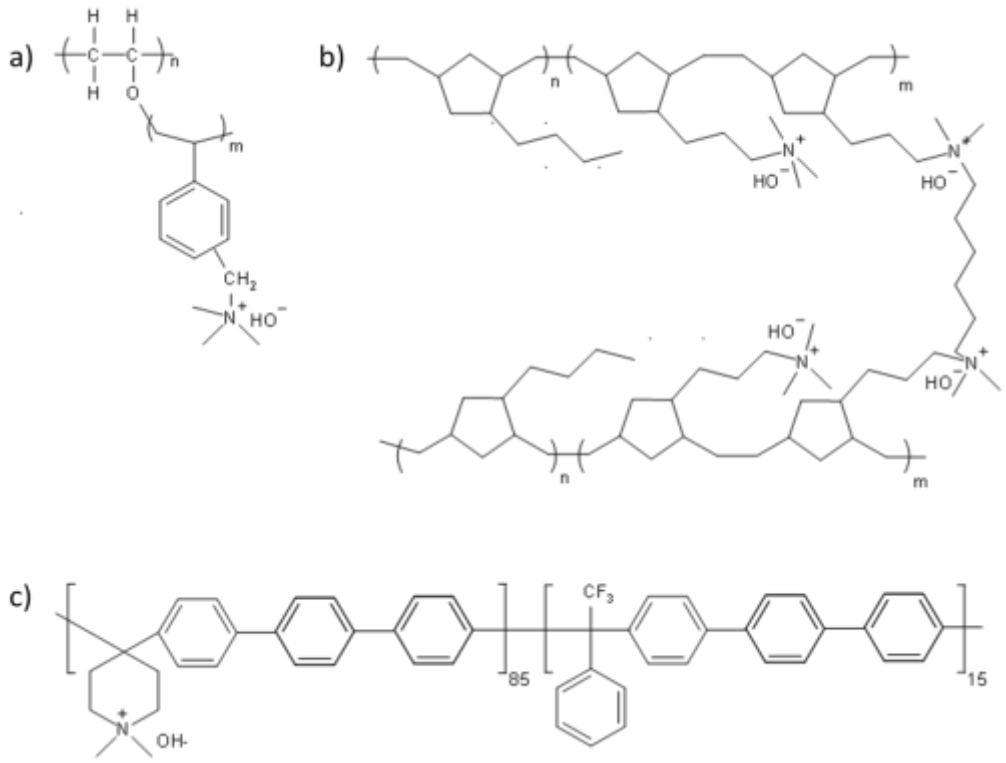

Figure 4.1 The structure of AEMs used in this study (a) high-density polyethylene polymer with a benzyltrimethylammonium cation (HDPE-BTMA) and low-density polyethylene polymer with a benzyltrimethylammonium cation (LDPE-BTMA), (b) poly (norbornene) copolymer of GT64-15, GT72-5 and GT78-15 and (c) poly(aryl piperidinium)-based polymer with a terphenyl chain (PAP-TP-85).

Table 4.1 Key properties of the polyethylene-based, poly(norbornene)-based and poly(aryl piperidinium)-based AEMs used in this study.

AEM	Cross-Linking Ratio (%)	IEC [a] (mmol/g)	Thickness [b] (μm)	WU [c] (%)	λ_{H2O} [d]	Swelling [e] (%)	σ [f], OH^-, 80 °C (mS cm^{-1})	Young's Modulus (MPa) [g]	Stress at Break (MPa) [g]
LDPE-BTMA [103]	NR	2.54 ± 0.21	15	149 ± 16	32 ± 3	27 ± 10	208 ± 6	248 ± 31	23 ± 6
		2.87 ± 0.05	25	104 ± 9	18 ± 2	22 ± 2	145 ± 8	386 ± 83	29 ± 5
HDPE-BTMA [103]	NR	2.44 ± 0.04	15	155 ± 15	35 ± 2	38 ± 7	214 ± 2	NR	35
PAP-TP-85 [86]	NR	2.2	15	60	15.13	8	175	425	50
GT72-5 [91,105]	5	3.44	10	96	15.24	35	175	NR	NR
GT78-15 [91,105]	15	3.62	10, 20	65	9.98	50	138	NR	28
GT64-15 [91,105]	15	3.28	10	29	8.81	14	142	175	NR

[a] IEC = mmol Cl^- per g (dry AEM, Cl^- form). [b] Dehydrated AEM thickness at room temperature (Cl^- form). [c] Gravimetric water uptake (Cl^- form) at room temperature (= 100 × (m_{hyd}–m_{dehyd})/m_{dehyd}, where m = mass/g). [d] The number of water molecules per Cl^- anion in the fully hydrated AEM, calculated as: λ_{H2O} = WU/(100 × 18.02 × IEC). [e] Through-plane swelling (= 100 × (t_{hyd}–t_{dehyd})/t_{dehyd}). [f] The 4-probe (in-plane) OH^- conductivity in a flowing 100% relative humidity N_2 atmosphere. [g] Tensile properties of the Cl^--form AEMs (error within 25%) in the ambient atmosphere. NR = not reported.

and amorphous signal were deconvolved by fitting the former to a linear baseline for integration. Integrals were performed using custom software coded in MATLAB software (Version 2020b, Mathworks, Natick, MA, USA). The measurement of polymer crystallinity is defined as:

$$\%\ Crystallinity = \frac{X_c}{X_c + X_a} \times\ 100 \quad (4.1)$$

Where X_c and X_a refer to the area of the crystalline and amorphous regions of scattering, respectively.

Shown as Figure 4.2, crystalline and amorphous regions were deconvolved by fitting crystalline regions to a linear baseline. The crystalline integral was defined as the area above this baseline while the amorphous was the region below. In other words, the amorphous integral is the total convolved integral minus the crystalline integral fit to a linear baseline. Integral values provided are arbitrary, but their relationship provides the basis for determination of percent crystallinity for the sample.

4.1.3 NEUTRON IMAGING CELL AND OPERATION

The operando neutron scattering imaging experiments were conducted at the NIST (National Institute for Standards and Technology) Center for Neutron Research (NCNR). The A diagram showing the dimensions for of the operando flowfields for these operando measurements is shown in Figure 4.3. The GDEs used in these experiments were identical to the ones described above, only cut to a smaller size after spraying. Before cell assembly, the membranes and GDEs were treated identically to above. The main difference was the cell hardware, previous described in detail elsewhere [24,26], which consisted of a gold-plated combination current collector and flow fields with a parallel flow pattern and active area of 2.5 cm^2. Again, cells were assembled with 6-mil gaskets to achieve approximately 20-

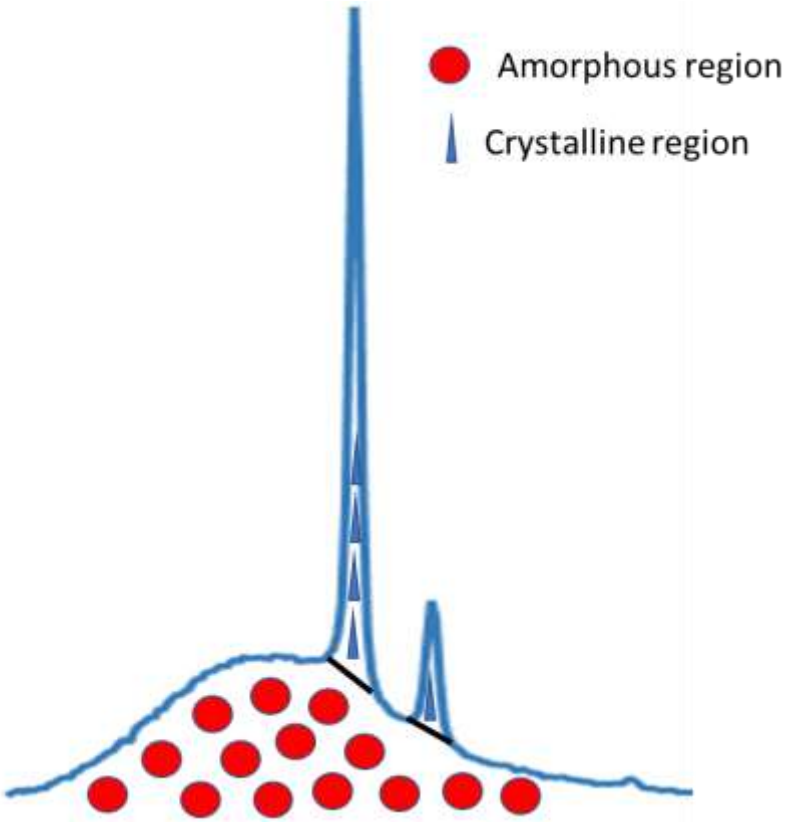

Figure 4.2 Illustration of crystallinity calculation

25% pinch. The cells were then humidified and broken in under the same protocol used for the 5 cm^2 cells. After stably running a cell for more than 8 h, 1% CO_2 was introduced into cathode gas stream, and the cell was run stably running for another 8 h. The neutron images were collected on the BT-2 beamline at the NCNR [106,107], and captured with an intensified macroscope detector capable of determining the centroid of emitted scintillation light [108]. For collimation, the L/D was 6000 along the through plane direction. Since the center of the test section was about 3 cm from the detector, the full-width half maximum of the geometric blur was ~2.5 μm. To align the operando fuel cell (FC) along the beam to yield 1 μm resolution would require an angular resolution on the rotation state of better than 0.005 degrees, which was within the state angular resolution of 0.001 degrees. For each fuel cell data point, about 4 h of centroid data were acquired, corresponding to a live time of about 20 min.

4.2 RESULTS AND DISCUSSION

4.2.1 INLUENCE OF ANION EXCHANGE MEMBRANE THICKNESS ON AEMFC PERFORMANCE WITH 400 PPM CATHODE CO_2

In the absence of CO_2, AEMFC performance generally increases as the membrane thickness decreases due to a combination of decreased ohmic resistance and increased water diffusivity [20,109–111]. It is also known that the water balance between the anode and cathode is extremely important for AEMFC performance as either cathode dryout or anode flooding can severely compromise FC stable operation [24]. In previous publications [54], It was also showed that FC water content has an effect on the CO_2 uptake into the cell and that a considerable fraction of the carbonation dynamics rely on what is happening in

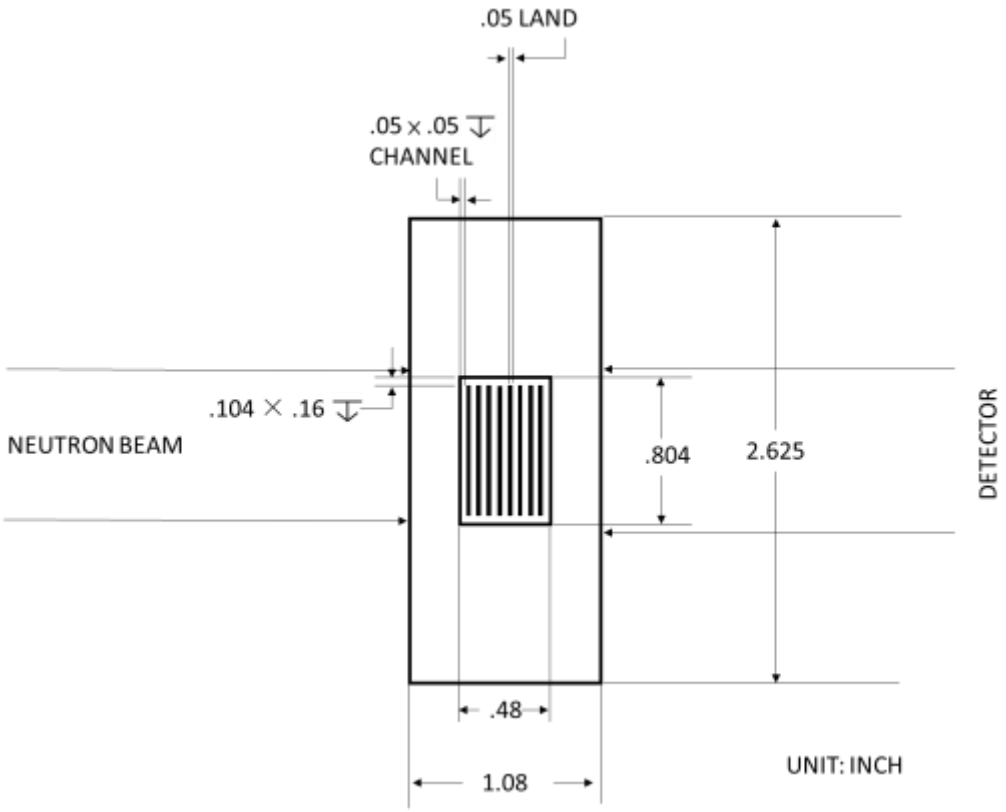

Figure 4.3 Schematic of the 2.5 cm^2 active area cell used for neutron imaging. Schematic dimensions are in inch.

the anode while the AEM can be a reservoir for carbonate. Therefore, despite the fact that increasing membrane thickness should increase the cell Ohmic resistance, it does not naturally follow that increasing the AEM thickness will increase the CO_2-related voltage losses.

The effect of AEM thickness on the AEMFC carbonation is shown in Figure 4.4. Figure 4.4 presents representative data from 2 sets of AEMs: 10 μm/20 μm GT78-15 and 15 μm/25 μm LDPE-BTMA. Figure 4.4a is the dynamic measurement of the voltage decrease and HFR increase for the AEMFCs deploying the AEMs above as CO_2 was introduced into the system. At t = 0 s, CO_2 was introduced to the cathode, and in all cases the voltage decreased and HFR increased. After ca. 5 min, a steady state voltage and HFR were reached and the rate in which the cell is taking up CO_2 at the cathode was equal to the rate of CO_2 emission at the anode. For both membrane types, a thinner membrane led to increased total voltage loss and a lower ΔASR.

Figure 4.4b shows the dynamic measurements for the concentration of CO_2 in the exhaust of the anode and cathode, which is transformed into molar flux in Figure 4.4c. In all cases, there was a time lag from the time that CO_2 was fed to the cathode and the time that CO_2 was observed purging out of the anode. This time lag is the result of carbonate accumulation in the anode, as discussed in the introduction, which lowers the anode pH until the reverse of Equations 1.3 and 1.4 are favorable and CO_2 is emitted. Within the same AEM chemistry, thinner membranes had lower lag times. This is most likely because thinner AEMs have fewer charge-carrying groups, allowing carbonation and equilibration to occur faster. The increase in charge carrying groups means that thicker AEMs can uptake

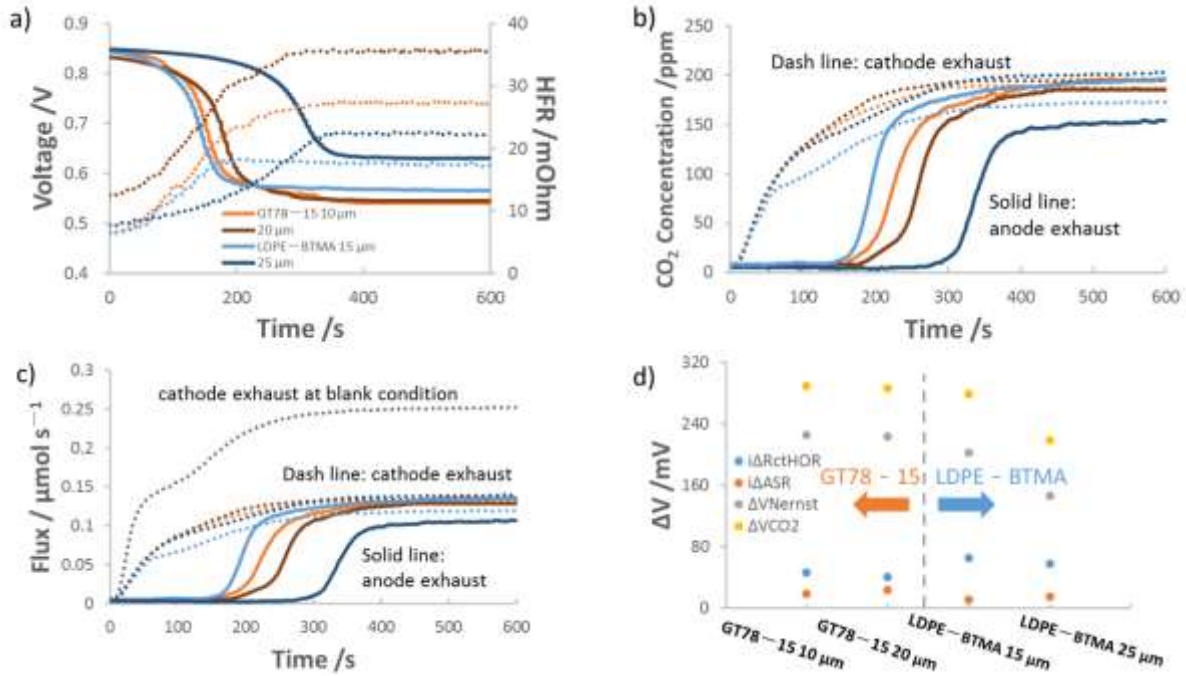

Figure 4.4 Effect of AEM thickness on AEMFC carbonation and performance loss. The AEMFCs were operated at 0.2 A/cm^2 and 76 °C/76 °C/80 °C with 10 µm, 20 µm GT78-15 and 15 µm, 25 µm LDPE-BTMA AEMs, 400 ppm CO_2 fed to cathode at t = 0 s, and 1 L/min H_2/O_2 flowrates. The anode catalyst loading was 0.5 mg_{Pt} cm^{-2} ± 0.1 mg_{Pt} cm^{-2}. The cathode catalyst loading was 0.6 mg_{Pt} cm^{-2} ± 0.1 mg_{Pt} cm^{-2}. (a) Voltage loss (solid lines) and HFR (dotted lines) following the introduction of CO_2 into the cathode; (b) concentration of CO_2 in the anode (solid lines) and cathode (dotted lines) effluent streams; (c) CO_2 flux leaving the anode and cathode; (d) deconvolution of the CO_2-related voltage losses.

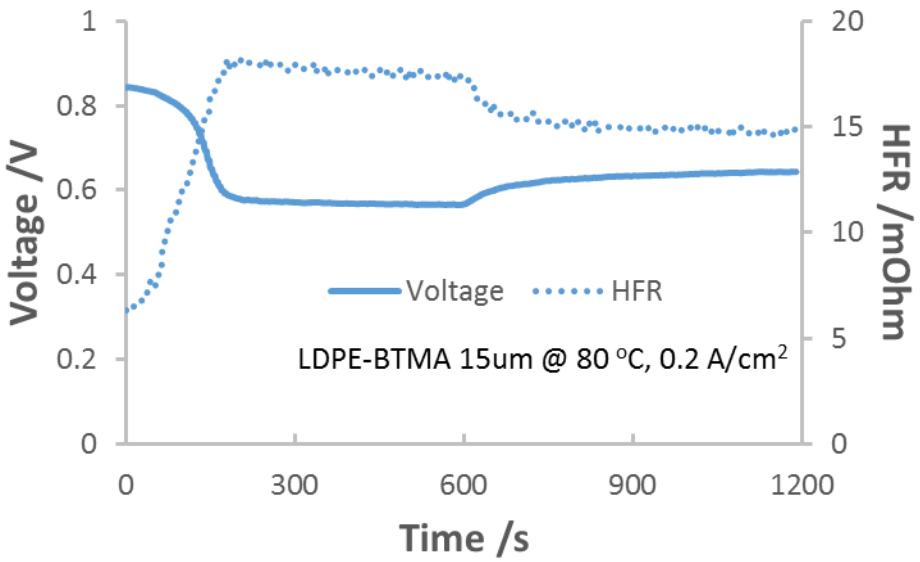

Figure 4.5 Voltage and HFR changes for 10 min carbonation and 10 min recovery process. Same condition as Figure 4.4.

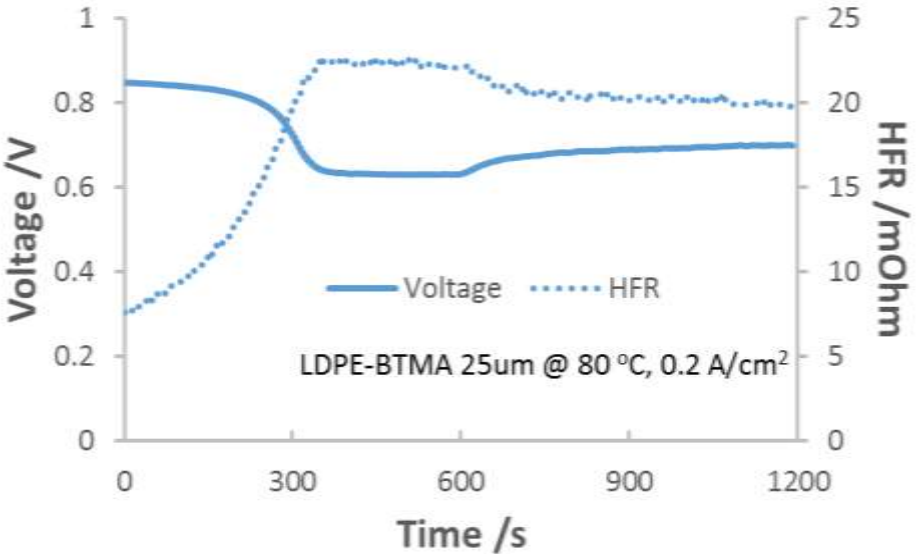

Figure 4.6 Voltage and HFR changes for 10 min carbonation and 10 min recovery process. Same condition as Figure 4.4.

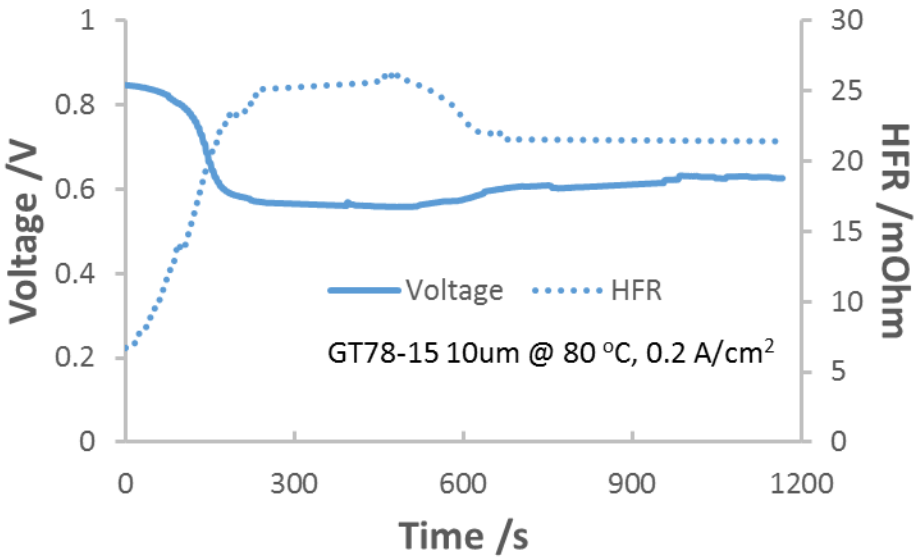

Figure 4.7 Voltage and HFR changes for 10 min carbonation and 10 min recovery process. Same condition as Figure 4.4.

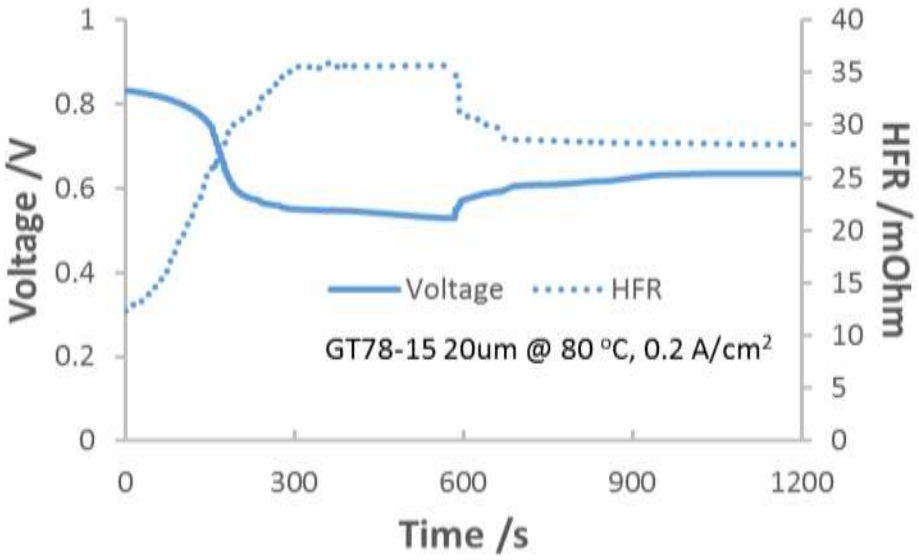

Figure 4.8 Voltage and HFR changes for 10 min carbonation and 10 min recovery process. Same condition as Figure 4.4.

Table 4.2 Degree of steady-state carbonation as function of AEM thickness of GT78-15 and LDPE-BTMA AEMs feeding with 400 ppm CO_2.

	GT78-15		**LDPE-BTMA**	
	10 μm	**20 μm**	**15 μm**	**25 μm**
AEMFC carbonate N_{CO2}/μmol	19 ± 1	24 ± 1	21 ± 1	32 ± 1
ΔASR/mΩ·cm^2	0.91	116	54	73
ΔR_{ctHOR}/mΩ	46	40	65	58
Degree of Carbonation, DOC (%)	27	21	41	44

more CO_2, which is confirmed by calculations of the total amount of carbonate (N_{CO2}) in Table 4.2.

From the carbonation data in Figure 4.4 and the CO_2-release data in Figures 4.5–8, it is possible to deconvolute the overall voltage loss from CO_2 into the contributions from the three main mechanisms discussed in the introduction: ΔASR, ΔV_{Nernst} and ΔR_{ctHOR}. The process to perform the deconvolution is described in the Supporting Information and detailed in previous publication [53] and the results are shown in Figure 4.4d and Table 4.2. As expected from the carbonation data in Table 4.2, where thicker membranes contained more carbonates, thicker membranes had both higher ΔASR and higher overall resistance. However, AEMFCs with thicker membranes experienced less ΔR_{ctHOR} and ΔV_{Nernst}, suggesting that AEMFCs with thicker AEMs may have less carbonate accumulated at the anode side or at least a longer distance over which the carbonate concentration gradient is relaxed.

Though the overall trends using both AEMs were the same, the degree of carbonation and the extent to which ΔASR, ΔR_{ctHOR} and ΔV_{Nernst} changed were not the same and cannot be explained by simple scaling functions based on the thickness. This suggests that the membrane chemistry or another underlying property might play a role in the carbonation of AEMFCs.

4.2.2 EFFECT OF AEM CHEMICAL STRUCTURE ON THE PERFORMANCE OF AEMFCS OPERATING WITH 400 PPM CO_2

Six AEMs—GT64-15, GT72-5, GT78-15, LDPE-BTMA, HDPE-BTMA and PAP-TP-85—were employed to investigate the effect of chemical structure on AEMFC carbonation.

These anion exchange membranes were selected because they have a wide range of properties and backbones, although they are similar in thickness at 10–15 μm. The behavior of AEMFCs using these AEMs under CO_2 dosing is presented as Figure 4.9. Of the membranes selected, HDPE-BTMA stood out as the fastest to reach the new steady-state voltage and HFR in Figure 4.9a. Compared within the same backbone and functional group, Figure 4.9a shows GT78-15 and LDPE-BTMA are slower to reach the new steady-state voltage and HFR than GT64-15 and HDPE-BTMA, respectively, implying that the carbonate interactions might be more complex. The former AEMs have larger HFR changes after CO_2 dosing, suggesting GT78-15 is more resistant to CO_2 poisoning than GT64-15 and LDPE-BTMA is slightly more resistant to CO_2 than HDPE-BTMA.

Also, as the degree of crosslinking of the GTXX-YY series of polymers was changed, differences in the carbonation behavior were observed. For a lower degree of crosslinking and similar IEC (e.g., GT72-5 vs. GT78-15), the poly(norbornene) polymers allow for more water uptake and have higher conductivity[18,104]. This is because AEMs with less crosslinking have more degrees of freedom for movement during synthesis, allowing for their structured water and ion transport channels to be more freely established[112]. Thus, GT72-5 showed more rapid voltage and HFR stabilization after feeding CO_2 than the other two anion exchange membranes with 15% crosslinker. This is also consistent with what was observed with PAP-TP-85. Because the PAP-TP-85 has its functional sites on the polymer backbone, they have less rotational freedom than some of the other polymers, also leading to longer equilibration times—although the same feature means that PAP-TP-85 has the best mechanical properties among the six AEMs, such as Young's modulus and stress at break as shown in Table 4.1.

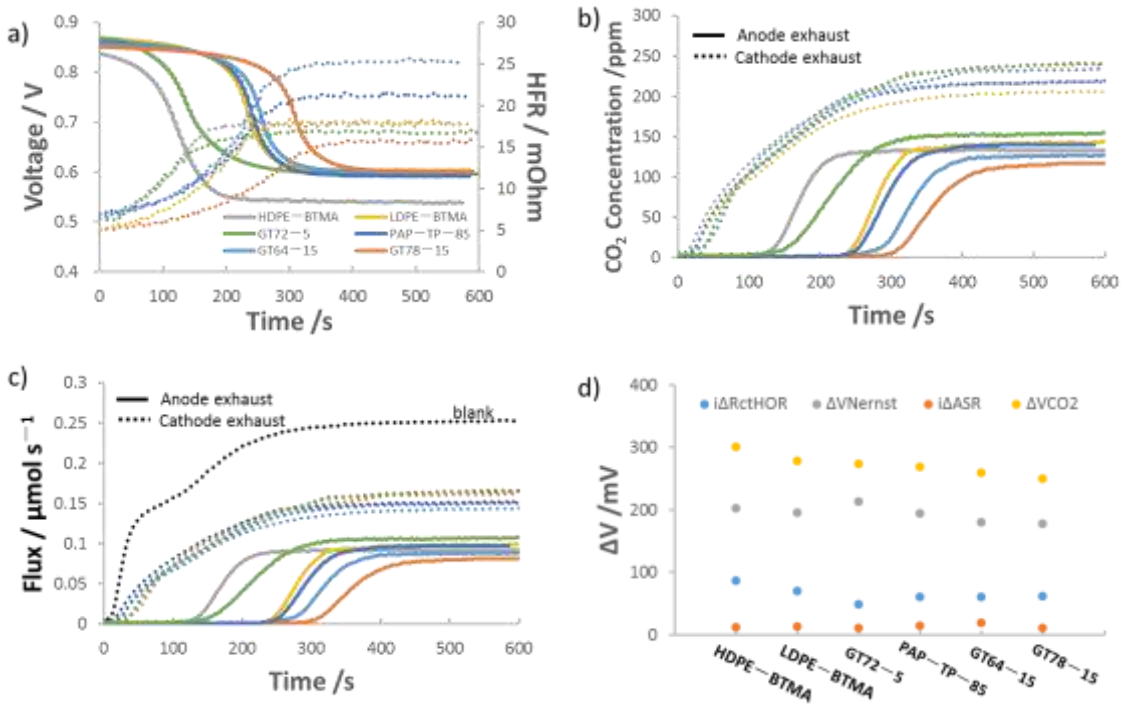

Figure 4.9 AEMFC carbonation and performance loss for six AEMs. AEMFC operating at 0.2 A/cm^2 and 52 °C/54 °C/60 °C with 15 µm ± 2 µm HDPE-BTMA, LDPE-BTMA, GT72-5, PAP-TP-85, GT64-15 and GT78-15 AEMs, 400 ppm CO_2 fed to cathode at t = 0 s, 1 L/min H_2/O_2 flowrate, 0.6 mg_{Pt} cm^{-2} ± 0.1 mg_{Pt} cm^{-2} on anode, 0.7 mg_{Pt} cm^{-2} ± 0.1 mg_{Pt} cm^{-2} on cathode. (a) Voltage loss (solid lines) and HFR increase (dotted lines) following the introduction of CO_2 into the cathode; (b) Concentration of CO_2 in the anode (solid lines) and cathode (dotted lines) effluent streams; (c) CO_2 flux leaving the anode and cathode; (d) deconvolution of the CO_2-related voltage losses.

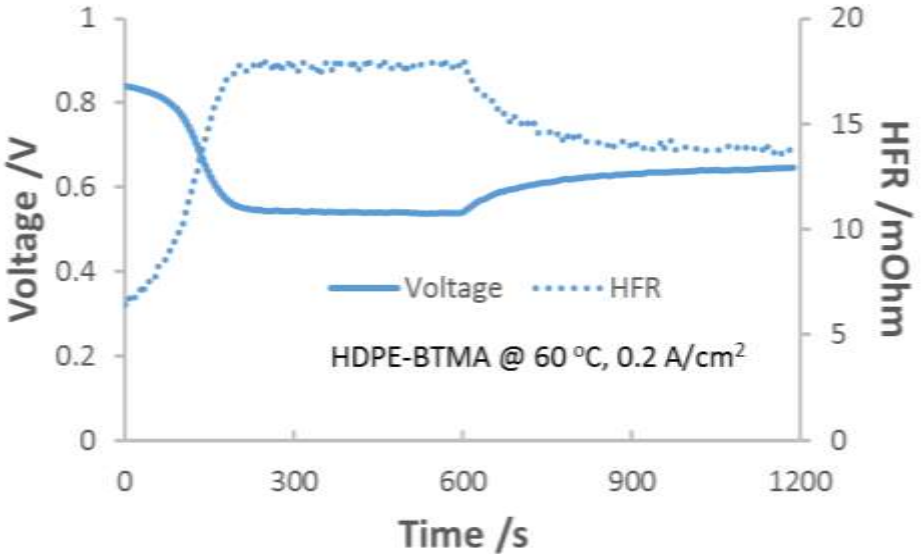

Figure 4.10 Voltage and HFR changes for 10 min carbonation and 10 min recovery process. Same condition as Figure 4.9.

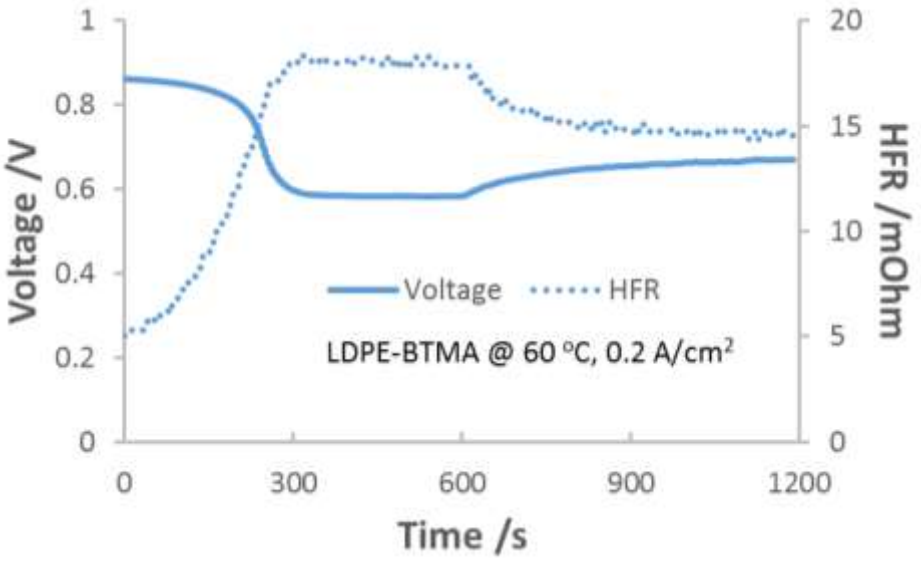

Figure 4.11 Voltage and HFR changes for 10 min carbonation and 10 min recovery process. Same condition as Figure 4.9.

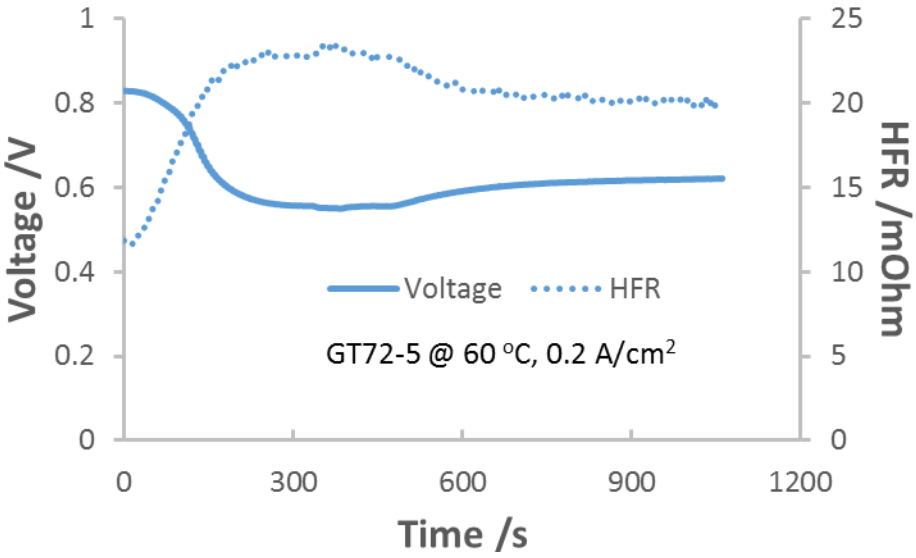

Figure 4.12 Voltage and HFR changes for 10 min carbonation and 10 min recovery process. Same condition as Figure 4.9.

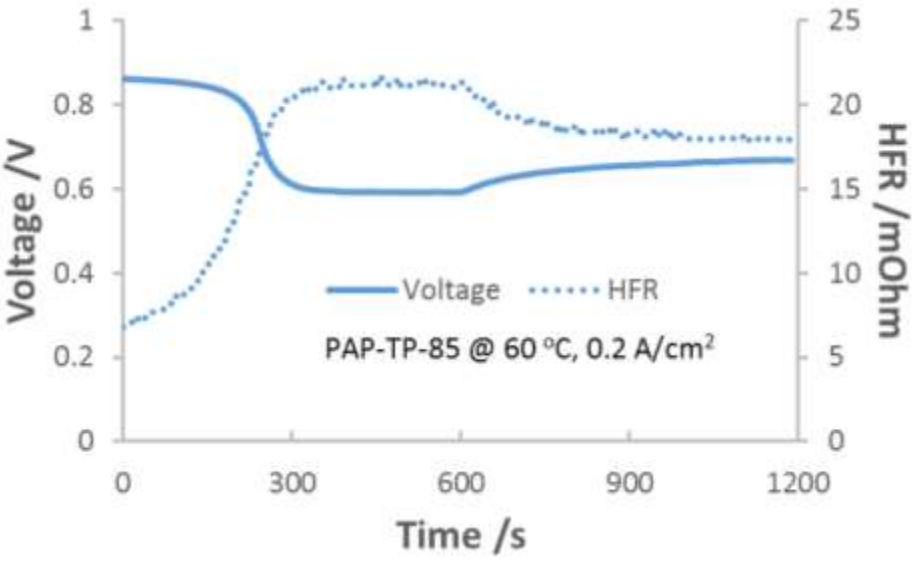

Figure 4.13 Voltage and HFR changes for 10 min carbonation and 10 min recovery process. Same condition as Figure 4.9.

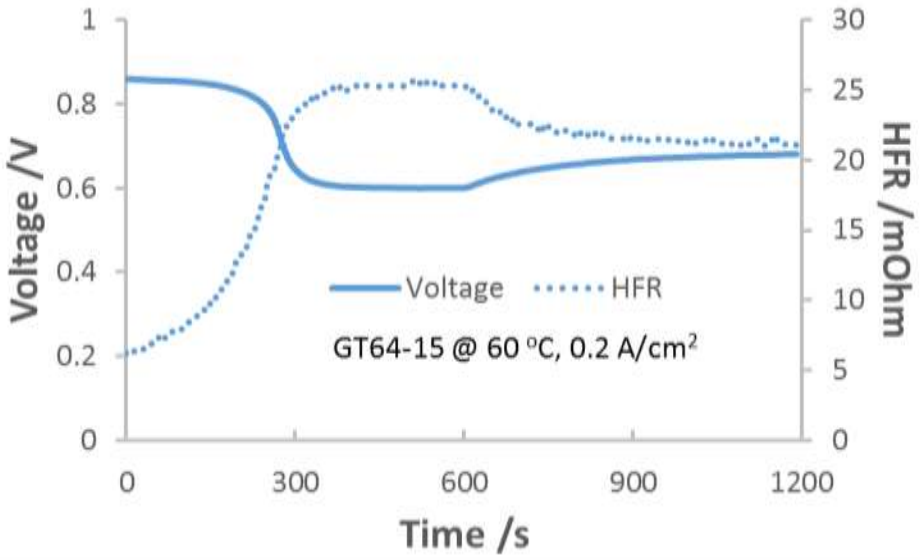

Figure 4.14 Voltage and HFR changes for 10 min carbonation and 10 min recovery process. Same condition as Figure 4.9.

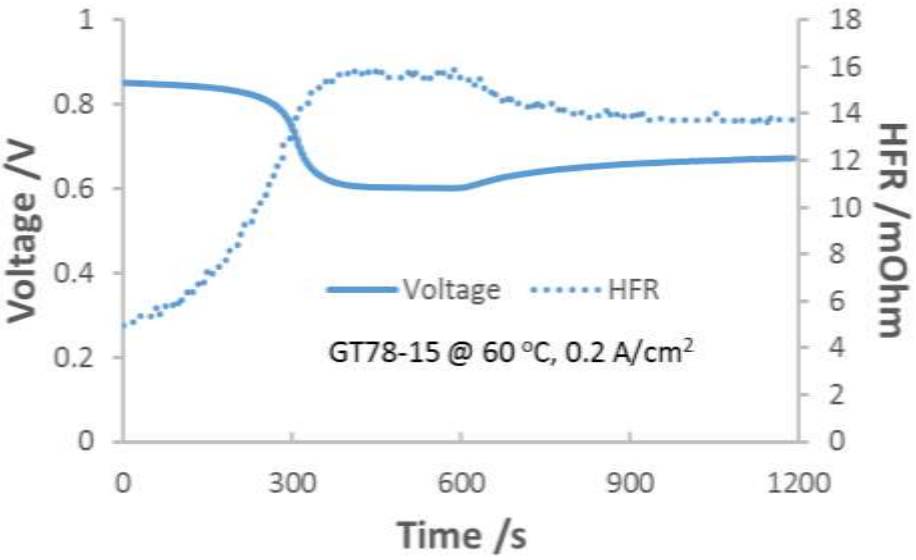

Figure 4.15 Voltage and HFR changes for 10 min carbonation and 10 min recovery process. Same condition as Figure 4.9.

The trends in the time that it takes for the cell voltage and HFR to achieve steady state after CO_2 addition suggests that the AEM crystallinity may play a role in in its carbonation behavior. Therefore, the crystallinity of the AEMs was investigated by wide-angle X-ray scattering (WAXS) and the results are shown in in Figure 4.16a. The integration and quantification of membrane crystallinity is shown in Figure 4.17-22. From data in Figure 4.16a, the degree of crystallinity obeys the following order: GT72-5 > HDPE-BTMA > LDPE-BTMA > GT64-15 > GT78-15 > PAP-TP-85. Regarding the trend, in the GT series, it makes sense that lower IEC, less cross-linked polymers would result in higher degrees of crystallinity. It also follows logically that HDPE has higher crystallinity than LDPE, though they are both similarly structured. Finally, it was observed that the PAP-TP-85 AEM is completely amorphous while still showing good conductivity and water uptake (Table 4.1)—showing that crystallinity and conductivity might need to be considered separately, which is discussed later.

This leaves open the question of whether or not crystallinity is the sole descriptor for carbonation behavior. To answer this, in addition to the operating voltage and HFR, the dynamics of cell carbonation can be observed in Figure 4.9b, which shows CO_2 concentration profiles of the anode and cathode exhaust for AEMFCs with all six AEMs. These are converted to the molar fluxes of CO_2 in Figure 4.9c. Figure 4.9b shows that the (bi)carbonate transport and stabilization is indeed slower for the GT78-15 and LDPE-BTMA AEMs than the GT64-15 and HDPE-BTMA AEMs, respectively. This further suggests that the former is more CO_2 tolerant. In addition, the CO_2 break-through time from the anode for GT72-5 is obviously shorter than the other GT AEMs, which is consistent with the voltage decrease rate in Figure 4.9a. GT72-5 also has the highest anode

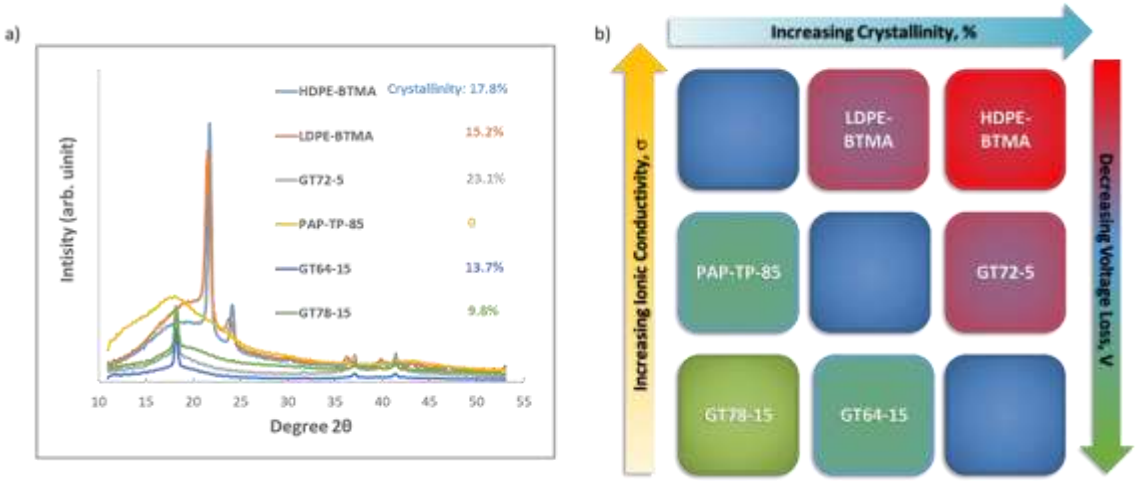

Figure 4.16 (a) Wide-angle X-ray scattering (WAXS) analysis of polyethylene-based, poly(norbornene) copolymer and poly (aryl piperidinium)-based AEMs; (b) AEMs mapping based on their relative conductivity and crystallinity properties.

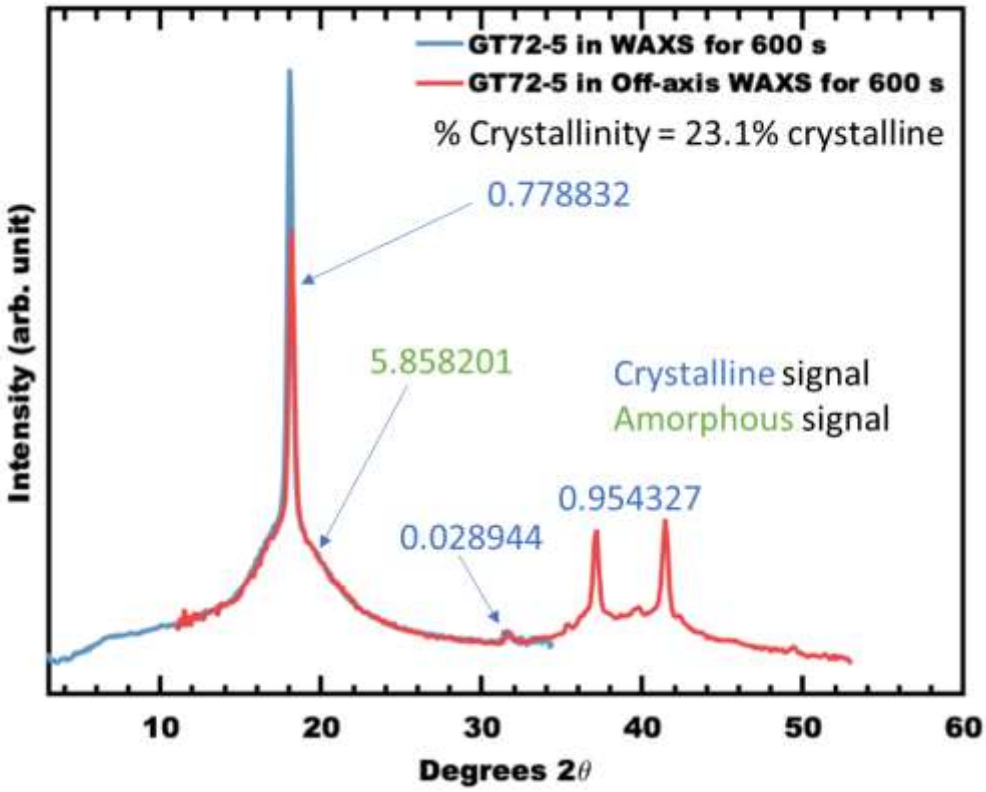

Figure 4.17 Quantification of GT72-5 AEM crystallinity by convoluting WAXS and Off-axis WAXS results

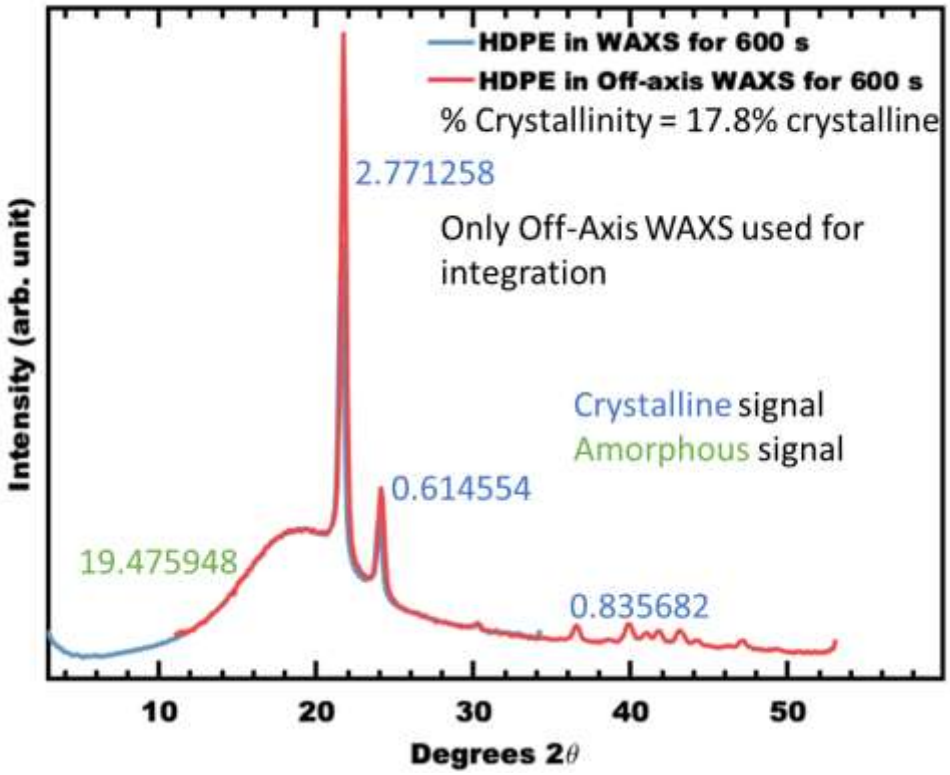

Figure 4.18 Quantification of HDPE-BTMA AEM crystallinity by convoluting WAXS and Off-axis WAXS results.

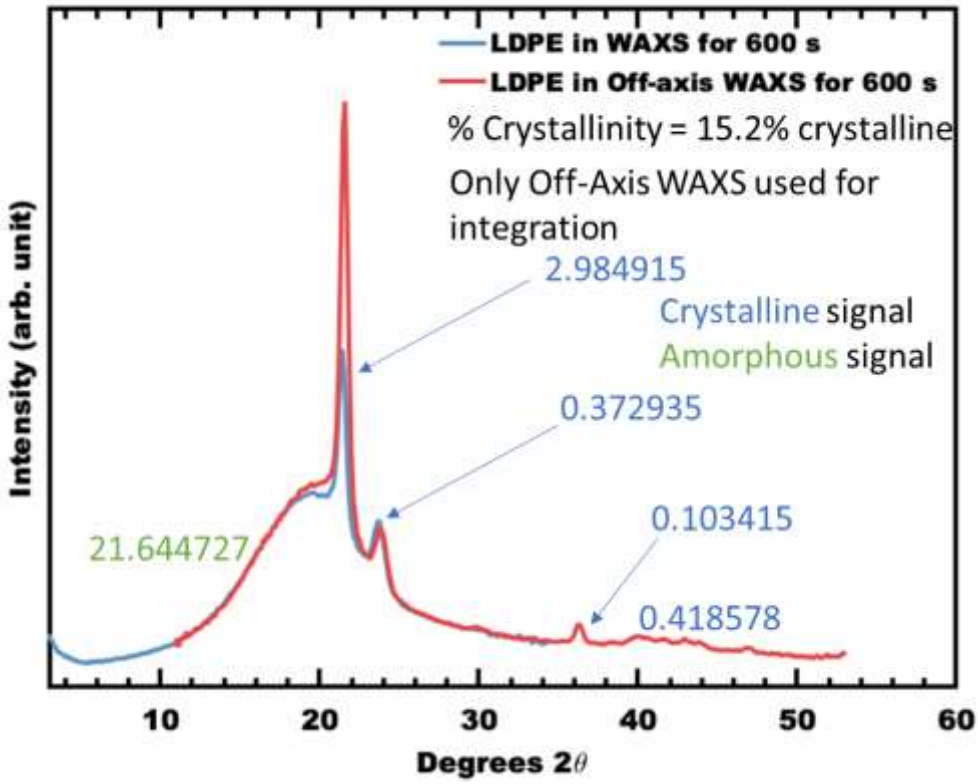

Figure 4.19 Quantification of LDPE-BTMA AEM crystallinity by convoluting WAXS and Off-axis WAXS results

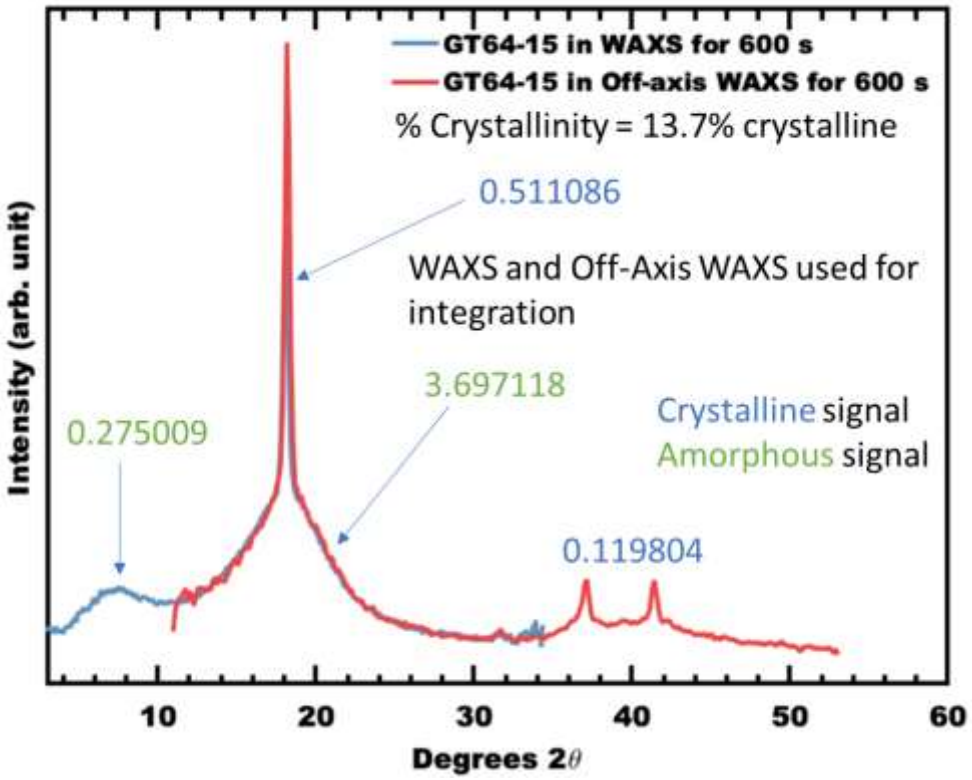

Figure 4.20 Quantification of GT64-15 AEM crystallinity by convoluting WAXS and Off-axis WAXS results

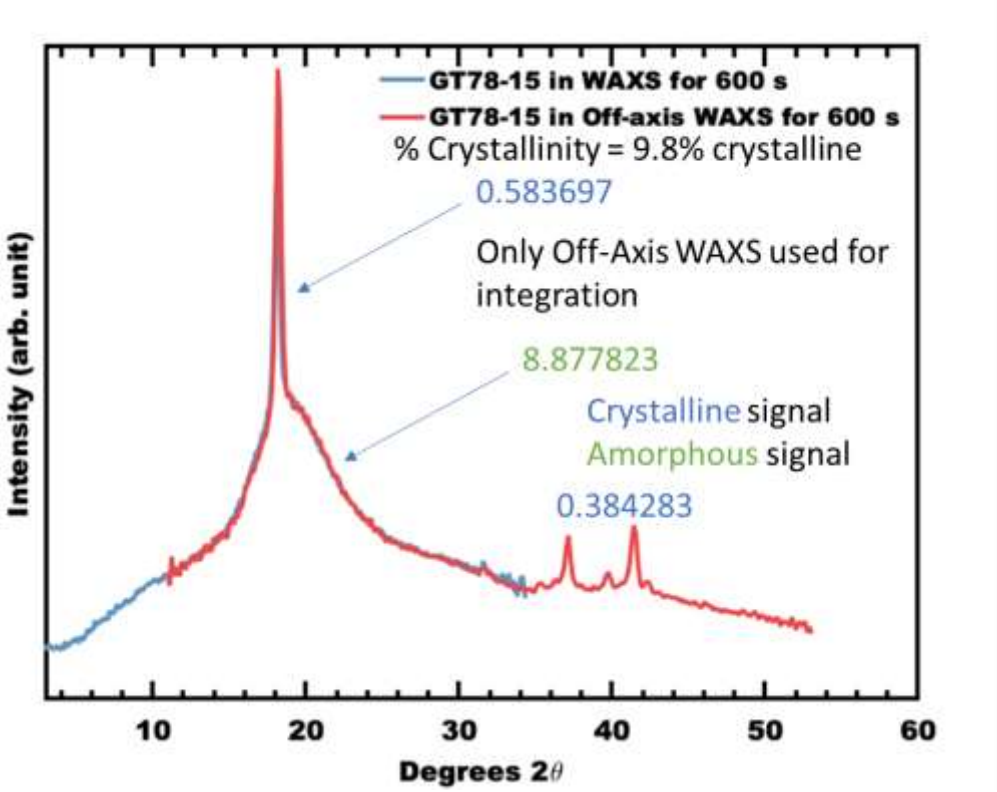

Figure 4.21 Quantification of GT78-15 AEM crystallinity by convoluting WAXS and Off-axis WAXS results.

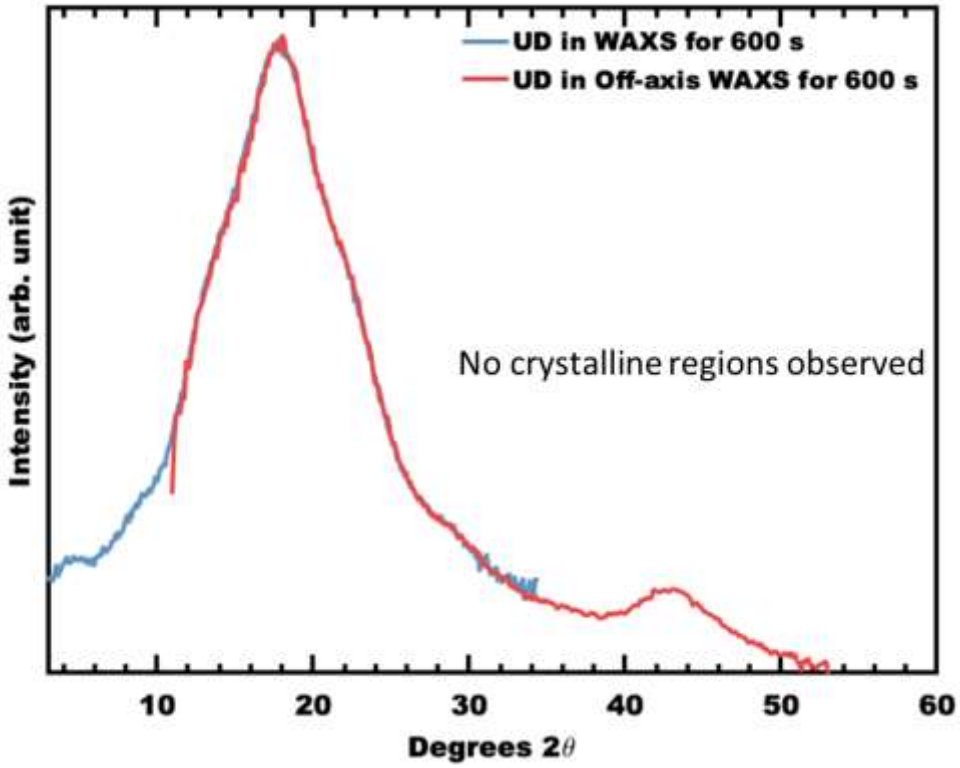

Figure 4.22 Quantification of PAP-TP-85 AEM crystallinity by convoluting WAXS and Off-axis WAXS results

exhaust concentration showing good CO_2 transport ability through MEA. Next, the steady-state carbonation and CO_2-release data in Figures 4.10-15 were deconvoluted and the results are shown in Figure 4.9d. There, the trend in the overall CO_2-related voltage loss was: HDPE-BTMA > LDPE-BTMA > GT72-5 > PAP-TP-85 > GT64-15 > GT78-15. Interestingly, this trend coincides better with their conductivity order—in fact, the highest conductivity AEMs showed the highest CO_2-related voltage loss. Therefore, it appears that the best-performing cells from a carbonation perspective prefer lower crystallinity and relatively lower ionic conductivity (note that although GT78-15 and GT64-15 are classified as "lower conductivity" here, their conductivity values are all high compared to an overwhelming majority of AEMs in the literature). This is illustrated in Figure 4.16b.

Digging into the individual mechanisms a bit deeper, it is not surprising that ΔV_{Nernst} is the overwhelming contributor to the CO_2-related voltage loss. However, both ΔV_{Nernst} and ΔV_{ctHOR} decreased with decreasing conductivity and increasing crystallinity, supporting the conclusion that the CO_2 concentration gradient in these materials may extend further into the AEM.

4.2.3 WATER DISTRIBUTION OF CARBONATED AEMFC BY OPERANDO NEUTRON IMAGING

To really see the influence of carbonation on AEMFC performance, the AEM that was the most influenced by carbonation (HDPE-BTMA) was selected and exposed it to CO_2 during operando neutron imaging. This was done because it has been suggested that the reaction of OH^- with CO_2 can lead to a further decrease in backbone crystallinity. Therefore, the CO_2 reaction not only affects the conductivity but also affects the overall polymer morphology. Combined, this says that the introduction of carbonate to the operating

AEMFC can lower the water uptake of the AEMs [51]. However, this has never been directly measured in an operating cell. This is important because it has become well known that water content and transport is of significant importance to AEMFC performance.

During the neutron imaging experiments, Figure 4.23, the cell was held at a constant current density, ensuring that the rate of water production in all experiments was identical. Therefore, any difference in the water content comes from the reacting gas dew points and water uptake abilities of the AEM + AEI. Figure 4.23a shows the operando neutron images for an AEMFC with a HDPE-BTMA AEM held at high dew points for more than 8 h without CO_2 poisoning. Figure 4.23b shows the same cell at optimized dew points, also operated for 8 h without CO_2 poisoning. Clearly, at lower dew points, the cell has less liquid water essentially everywhere in the cell due to increased convective evaporation of produced water into the reacting gases. Finally, at the optimized dew points, 1% CO_2 was added to the cathode inlet, and the resulting neutron images are shown in Figure 4.23c. Compared with Figure 4.23b, there was significantly less water in the AEM and electrodes. Quantitative through-plane water distribution plots, Figure 4.23d, confirm that, indeed, introducing CO_2 into an operating AEMFC does lower the water content of the cell, which will further decrease performance—even in addition to the three direct CO_2-related mechanisms already recognized.

4.3 SUMMARY

In this paper, the effect of AEM properties on AEMFC carbonation is focused and studied for the first time. It was found that, across AEM chemistries, decreasing ionic conductivity and decreasing crystallinity tended to lower the overall CO_2-related voltage loss. These give new design principles to manufacture next-generation AEMs with higher

CO_2 tolerance. Lastly, the content and distribution of liquid water in a stably operating AEMFC was directly observed by neutron imaging before and after carbonation. It was shown that carbonation significantly reduces the water content of the cell.

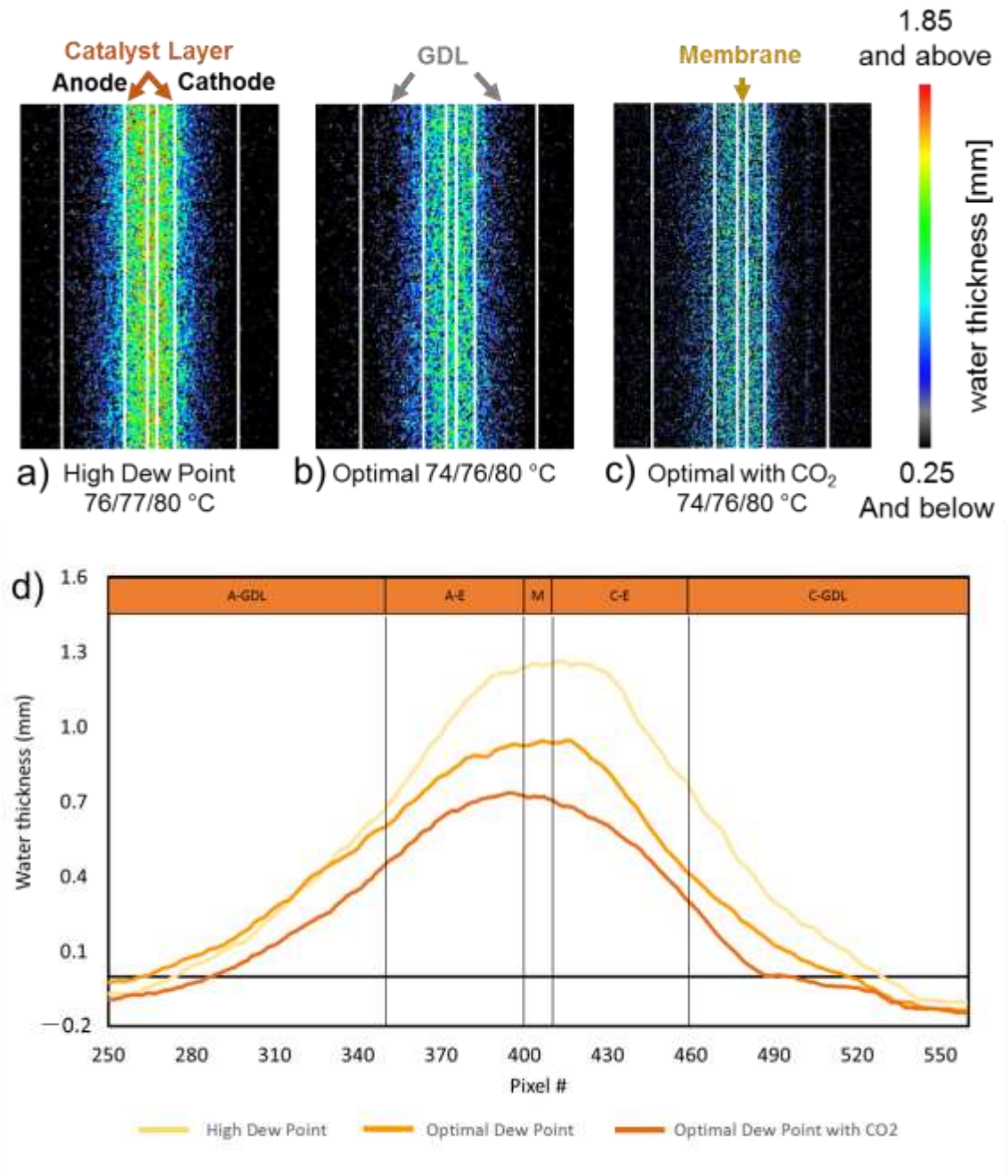

Figure 4.23 *Operando* neutron images of water in the gas diffusion layers, catalyst layers, and HDPE-BTMA AEM in operating at 1 A cm^{-2}, 1 L/min at both sides, (a) high dew point at 76 °C /77 °C /80 °C (b) optimal dew point of 74 °C/76 °C/80 °C (**c**) optimal dew point and 1% CO_2 in cathode stream (d) qualitative through-plane water distribution plot extracted from (a)–(c). The cells used in the neutron beam (2.5 cm^2 active area) were constructed with a 0.88 mg_{Pt} cm^{-2} PtRu/C anode, a Pt/C cathode at 1.3 mg_{Pt} cm^{-2}, and an ETFE-based AEI

CHAPTER 5: POWER-GENERATING ELETROCHEMICAL SCRUBBING FROM AIR ENABLING PRACTICAL AEMFC APPLICATION

In total, those three mechanisms mentioned in the Chapters above can lead to an AEMFC voltage loss of 150-300 mV when the cathode gas contains 400 ppm CO_2.[44,45,53] Unfortunately, cell voltage losses are not limited to air-relevant CO_2 concentrations. AEMFCs continue to experience significant reductions in cell performance even when the CO_2 in the cathode feed is reduced below 50 ppm and adjustments are made in the operational variables (e.g. reduced cathode flowrate, increased temperature) to limit it effects.[54] Therefore, it has become clear that the clearest path to enabling AEMFC operation with atmospheric air, is to lower the CO_2 concentration in the air feed to the cathode before entering the cell.

Current CO_2 capture technology includes mainly physical and chemical absorption, adsorption and membrane processes. Chemical absorption is the most mature and reliable technology for post combustion CO_2 removal from thermal power plants. [113,114] However, each of the aforementioned technologies are net energy consumers (either thermal or electrical) and they would also increase system volume and complicate the systems-level balance-of-plant for an AEMFC system. Electrochemical methods offer a unique way to separate CO_2 from a gas stream with no moving parts, unlike sorbent or solvent-based processes. The original motivation of applying electrochemistry to CO_2 separation dates

back to the need for removal of carbon dioxide from breathing gas mixtures on manned space flights or underwater environments.[115,116] However, most electrochemical approaches have also been significant energy consumers as they are based on the "pumping" of carbonates.[82,115–118]

Putting the unwanted side reactions with CO_2 in the AEMFC to work, AEMFCs electrochemically separating CO_2 from a gas mixture has its origins in investigations of the self-purging mechanism. Eisaman[119] et al proposed a fuel-cell concentrator to separate CO_2 from air. Using air with 400 ppm of CO_2 as the cathode gas and pure H_2 as the anode gas, a net pumping of up to 20% of the CO_2 from the cathode stream to the anode was achieved. However, only extremely low current densities (<1 mA/cm^2) were applied, limiting the scalability of the approach to capture appreciable amounts of CO_2. The CO_2 separation aspect would have other implications including the removal, compression, and storage of the CO_2 from the H_2-rich anode gas, which would present additional challenges, particularly in mobile applications.

One main AEM CO_2 separation approach used in the literature is a driven cell method in which a mixture of O_2 and CO_2 is fed on the cathode side and an inert carrier gas is fed on the anode side.[82,120] Current is applied to the cell, driving the oxygen reduction reaction on the cathode side and the oxygen evolution reaction on the anode side. It is not clear if carbonate is formed through direct electrochemical reactions with O_2 or subsequent chemical reactions with OH^-, but the net result is the same. For the indirect pathway, OH^- reacts with the CO_2, forming CO_3^{2-} and HCO_3^-, allowing for the net transfer of CO_2 from the cathode to anode. When HCO_3^- or CO_3^{2-} is neutralized on the anode, it results in CO_2:O_2 ratios of 4 and 2, respectively. Therefore, it would not be possible to obtain a pure

CO_2 gas from this process alone, as it necessitates the evolution of O_2 in the permeate gas. One proposed use for the gas is as an oxidant for an oxy-combustion process, which would then result in a high-CO_2 exhaust gas that could be stored or processed to other products[121,122].

One interesting alternative approach has been previously proposed by Yan et al, both in the patent literature[123] and presented at the 235th meeting of the Electrochemical Society [124]. However, the concept has not been widely investigated or its behavior reported in the archival literature. The approach is inspired by the carbonation chemistry in the AEMFC, where it is possible to take advantage of the fact that the AEMFC intrinsically will remove CO_2 from the oxidant stream and move it to the fuel stream while producing power. In this approach, illustrated in Figure 5.1, air is supplied to the cathode inlet of a smaller AEMFC-device, which is denoted as the anion exchange CO_2 separator (AECS). It is in the AECS where the carbon dioxide is captured. The product air from the AECS, with a much lower CO_2 concentration, is then fed to the cathode of the primary, larger AEMFC. The fuel for the primary AEMFC is supplied by the H_2 feed and the fuel stream for the AECS is supplied from the hydrogen purge from the main AEMFC. The anode stream from the scrubber AECS will contain the exhaust CO_2, water, N_2 and, if engineered properly, only trace H_2. Though it is not the primary goal of the system, it is also noteworthy that this presents an alternative solution to N_2 accumulation in the AEMFC from diffusion, which also occurs in PEMFCs (forcing the anode to be periodically vented).

Though such a system appears conceptually sound, it should be noted that its performance has not been reported in the archival literature to date. Therefore, it is presently unknown how effective such a device would be in removing CO_2 and very important questions

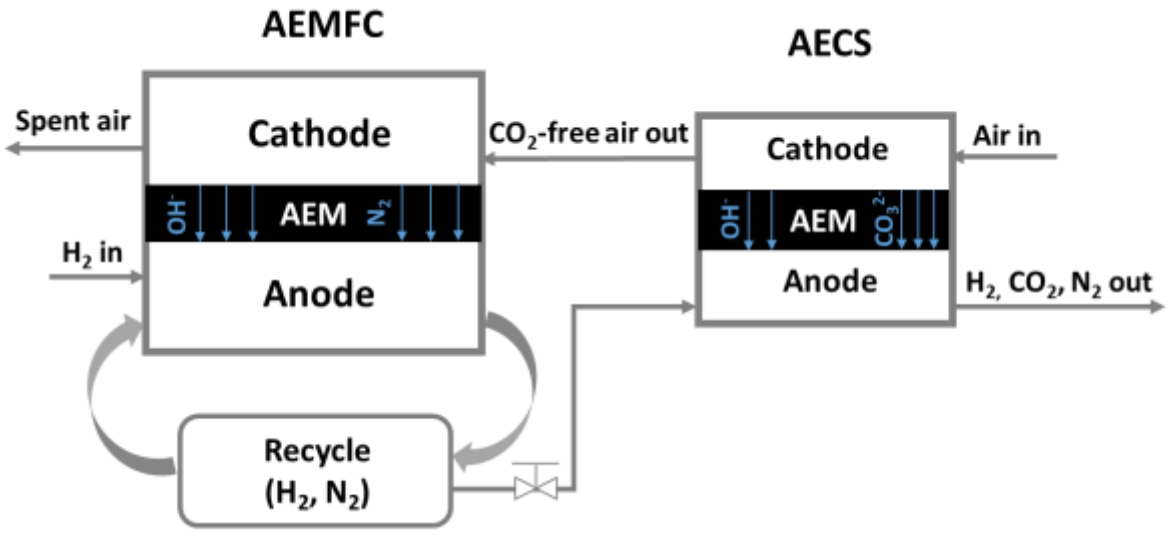

Figure 5.1 Scheme of the fuel cell system comprised of both the CO_2-removing AECS and the primary AEMFC.

remain, such as: (i) can AEMFC-based electrochemical CO_2 scrubbers remove enough CO_2 from the air stream to run the primary AEMFC without any notable performance loss? (ii) What is the lowest CO_2 concentration that can be achieved coming out of the scrubber? (iii) How is the lowest achievable concentration affected by the flow configurations of the cell? (iv) How large (in terms of surface area) would the scrubber cell have to be relative to the main cell in a real system? It is also worth noting that no cell has yet been demonstrated in the literature where electrochemically-scrubbed CO_2 was fed to an operating AEMFC.

In this Chapter, AECS cells comprised of cumulative geometric areas from 5-50 cm^2 are assembled and operated. The effect of surface area on the efficacy of the CO_2 removal, with the goal of demonstrating an AECS with less than 1ppm CO_2 in the exhaust is evaluated. AECS cells are also exposed to stability tests in excess of 100 hr with industrial air as the feed. Finally, an AECS-AEMFC system is demonstrated for the first time where electrochemically scrubbed CO_2 is successfully fed to the cathode of an operating AEMFC.

5.1 EXPERIMENTAL

For the AECS cells operating on O_2, after break-in and equilibration, the cell current was maintained at its equilibrated value (0.2, 1, 1.2 or 2 A/cm^2 for different cells and conditions) and 400 ppm CO_2 was added to the cathode stream. The flowrate of O_2 was maintained at 1 L min^{-1} and flowrates of H_2 were set at 0.2 or 1 L/min. 30 psi cathode backpressure was applied for all conditions. Typically, after CO_2 addition, the cell was operated for 20 min, which was much longer than the time required to reach quasi-steady-state operation (typically < 5 min). After 20 min operation at constant current, CO_2 was removed from the gas stream and the cell was allowed to self-purge for an initial 10 min. After this, the AECS was fully decarbonated by lowering the cell potential to 0.1 V for 2

min, after which no CO_2 emission was measured in the anode stream and the operating voltage returned to the value observed before CO_2 was added. For cells operated on industrial air, after the break-in procedure under O_2 at the desired operating current, the cell was switched from O_2 to CO_2-free air and the cell was allowed to reach steady state at the same current (0.12, 0.6 or 1.2 A/cm^2) for 10 min. To introduce CO_2 to the system, the cathode gas was switched from CO_2-free air to industrial air. The cathode flowrate was maintained at 1 L min^{-1} and the flowrate of H_2 was set at either 0.2 or 1 L/min. 30 psi cathode backpressure was applied for all experiments. The carbonation and decarbonation procedures were the same as described above for the cells operating on O_2, though decarbonation was achieved by switching back to CO_2 –free air not O_2.

For all experiments, the concentration of CO_2 in the AECS anode and cathode effluents were continuously monitored using a PP Systems WMA-5 non-dispersive infrared CO_2 gas analyzer. A water trap was placed in-line before the WMA-5 in order to preserve the unit and its calibration. It should also be noted here that the full configuration illustrated in Figure 5.1 was not assembled here to test the performance of the AECS in isolation. Instead, single cells were assembled with the flow pattern described above. For clarity, an illustration of the flow pattern for the cell is provided in Figure 5.2.

5.2 RESULTS AND DISCUSSION

5.2.1 CO_2 REMOVAL IN 5 CM^2 ACTIVE AREA AECS CELLS USING 400 PPM CO_2 IN O_2

One of the most important features of the AECS scrubber is the effectiveness for CO_2 removal per unit scrubber area because this will set its relative size of the AECS versus the

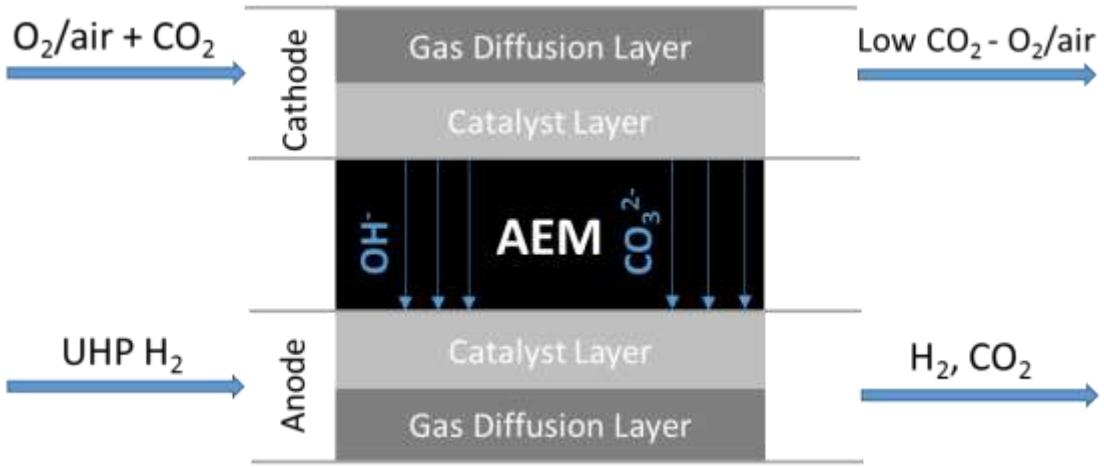

Figure 5.2 AECS cell configuration for the stage experiments.

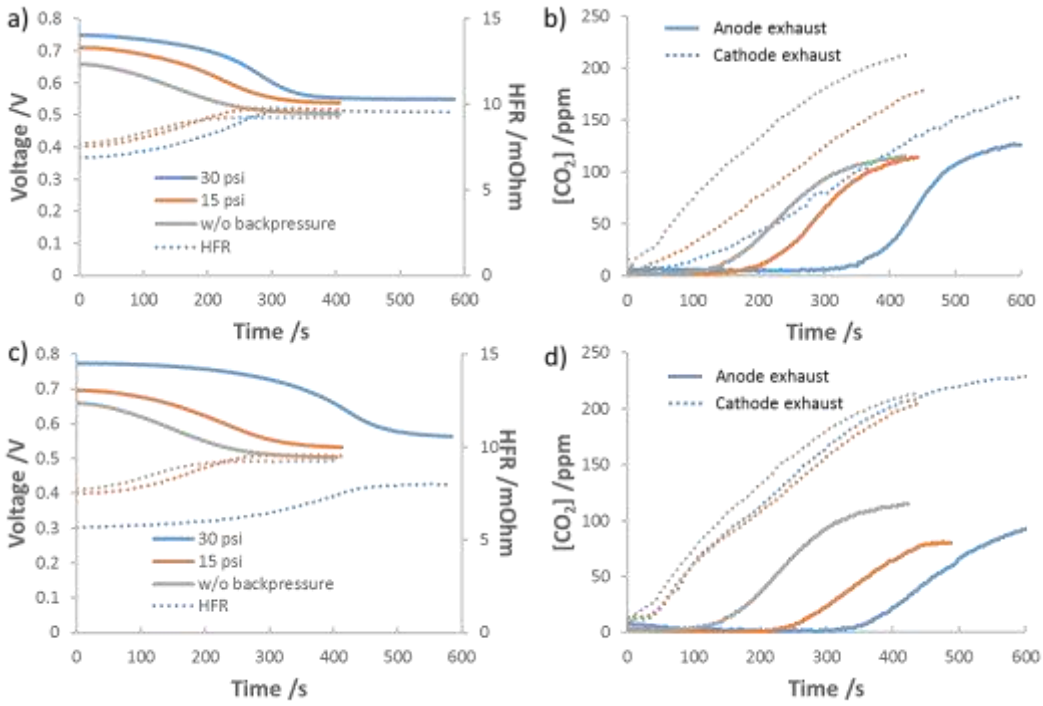

Figure 5.3 5 cm^2 active area AECS operating at 6 A and 70 ^oC with a GT72-5 AEM with 400 ppm CO_2 fed to the cathode at t = 0 s with 1.0 L/min anode and cathode flowrates. a) Voltage loss (solid lines) and HFR increase (dotted lines) following the introduction of CO_2 into the cathode with cathode backpressure at 0, 15, 30 psi and no anode backpressure; b) Concentration of CO_2 in the anode (solid lines) and cathode (dotted lines) effluent from the experiment in panel a; c) Voltage loss (solid lines) and HFR increase (dotted lines) following the introduction of CO_2 into the cathode with anode backpressure at 0, 15, 30 psi and no cathode backpressure. and d) Concentration of CO_2 in the anode (solid lines) and cathode (dotted lines) effluent streams from the experiment in panel c. The results are color-coded based on CO_2 dosing concentrations.

AEMFC. As the AECS active area increases, a greater amount of CO_2 can be separated from the cathode air stream, under most conditions. To understand the CO_2 capture efficacy of the AECS, without any possible interference from the O_2 dilution, first CO_2 was added to UHP O_2. The flowrate was set at 1.0 L/min of oxygen with 400 ppm CO_2 at 80 ^oC (34 mmol/min oxygen), which would be sufficient to power a total active area (AECS + AEMFC) of 219 cm^2 operating at 1.0 A/cm^2 (which is required to satisfy the U.S. Department of Energy 2022 AEMFC performance target[125]). Also, 30 psi backpressure was applied at the AECS cathode; the effect of anode and cathode backpressure on the AECS CO_2 efficacy is analyzed in Figure 5.3.

The effect of cathode and anode backpressure on the CO_2 capture efficacy of the AECS was studied in Figure 5.3. As shown in Figure 5.3a, increased cathode backpressure improved the operating cell voltage and reduced the HFR. However, as backpressure was added, the AECS required a longer time to reach steady state. The magnitude of the effect of backpressure was less when applied to the cathode than the anode (Figure 5.3c). Figure 5.3b shows that more CO_2 was transported through the MEA to the anode as the cathode backpressure was increased. Conversely, as the anode backpressure was increased, the amount of CO_2 measured in the anode was reduced.

Initially, 400 ppm CO_2 was added into the cathode flow and the 1.0 L/min reacting gas stream was fed to a 5 cm^2 AECS cell. During this time, the exhaust CO_2 concentrations from anode and cathode gas outlets were measured as well as the cell voltage and high frequency resistance. The results of those experiments – labeled as "stage 1-400 ppm-5 cm^2" – are shown in Figure 5.4 for AECS cells operating at 70^oC and 1.2 A/cm^2 with an anode H_2 flowrate of 0.2 L/min (Figures 5.4a-b) and 1.0 L/min (Figures 5.4c-d). The x-

axis in Figure 5.4 is the time from initiation of the CO_2 flow in the cathode feed. The time delay from the time that CO_2 is fed to the cathode to when it is detected is mostly due to gas equilibration within the humidifier bottle as well as the uptake of CO_2 into the cell. The time delay in the measurement of CO_2 in the anode exhaust is mostly due to the time that it takes for the buildup of carbonates at the anode and the pH to drop, releasing CO_2. For both anode flowrates, when 400 ppm CO_2 was fed to the cell, the cell voltage was decreased by approximately 200 mV compared to the CO_2-free O_2 feed condition. As expected from previous work[54], the anode flowrate did not significantly affect the voltage loss or the HFR because the level of cell carbonation at steady state is similar. For cells operating at both flowrates with 400 ppm CO_2 fed to the cathode, the exhaust concentration of CO_2 after 1200s was around 233 ppm CO_2. The main effect was in the concentration leaving the anode exhaust, which was higher at lower flowrates due to less dilution, though it should be noted that lower anode flowrates also lead to longer times for both CO_2 breakthrough (when CO_2 is measured in the anode exhaust) and reaching steady-state. From the data in Figure 5.4, it is clear that a 5 cm^2 AECS operated under those conditions shown in Figure 5.4, is not able to remove a sufficient amount of CO_2 to effectively operate the main AEMFC.

To further decrease the CO_2 concentration in the AECS cathode exhaust to acceptable levels to operate a main AEMFC, a larger AECS active area is needed. However, the exact size of the needed cell is uncertain from the one measurement above. It is also unclear how the CO_2 removal efficacy would be affected as the size of the AECS would be increased. To mimic a systematic increase in the AECS active area, a series of experiments were done that increased the effective active area in 5 cm^2 "stages". To do this, the same cell was

used for each family of experiments. First, 400 ppm was fed to a 5 cm^2 AECS. This was considered to be Stage 1 (total AECS active area = 5 cm^2). After 1200 s, the concentration of CO_2 in the cathode exhaust was noted (233 ppm in Figure 5.4a and 232 in Figure 5.4c). Then, inlet concentration of CO_2 into the AECS cathode was changed to be equal that leaving Stage 1. This was considered to be Stage 2 (total AECS active area = 10 cm^2, the sum of Stage 1 and Stage 2). The concentration leaving the cathode is close for each stage at both anode flowrates. After 1200 s, the CO_2 concentration in the cathode exhaust was noted (127 ppm in Figure 5.4a and 130 in Figure 5.4c) and the concentration entering the AECS cathode was changed to that value. This process was repeated multiple times with the same 5 cm^2 cell until a total effective area of 30 cm^2 (Stage 1 + Stage 2 + Stage 3 + Stage 4 + Stage 5+ Stage 6) had been achieved. Thus, the labels for the curves in Figure 5.4 (in ppm CO_2) are the concentration of CO_2 entering a given 5 cm^2 stage. UHP H_2 was fed to the anode for all experiments. Because lower CO_2 concentrations can lead to longer times to reach steady state, stages 5 and 6 in Figure 5.4a do not reach steady state. A full 60 minute tracing for stages 5 and 6 are shown in Figure 5.5.

As shown in Figure 5.4, with each new stage (increased overall area), the concentration of CO_2 leaving the cathode was steadily reduced. In fact, as discussed later, the capture efficiency was a constant fraction of the inlet concentration and predictable (~60 % per 5cm^2 stage at these conditions). It should be noted that the mass balance closes and the molar flowrate of CO_2 leaving any stage was essentially equal the sum of the anode and cathode CO_2 molar flowrates from the next stage. Also, because of the lower CO_2 concentration in each successive stage, the presence CO_2 had less of an effect on the amount of energy that could be generated in that AECS stage. With each successive stage,

the output cell voltage increased and the HFR decreased, compared to the previous stage. After six stages with each having 5 cm^2 active area, the exhaust CO_2 concentration leaving the final AECS cathode was ca. 4 ppm. It is encouraging that such low concentrations are achievable. Of course, if the desired air flowrate to be scrubbed were higher, a larger cell would be needed to reach this same concentration. The CO_2 capture rate could also be increased by increasing the AECS operating current. It is noted that multiple cells were tested for each measurement, with representative data shown here, and the measured CO_2 exhaust show few ppm (< 5 ppm) deviation between cells.

5.2.2 LARGER FORMAT 25 CM^2 AECS CELLS WITH 400 PPM CO_2 IN O_2

Using smaller area stages to simulate a larger cell in the experiment described above allowed for inter-stage analysis, however, fresh H_2 was supplied to each stage, which could artificially boost the amount of CO_2 that can be removed. Therefore, the CO_2 scrubbing ability of a single 25 cm^2 active area AECS with 400 ppm CO_2 in the O_2 fed to the cathode was investigated and the results are shown in Figure 5.6. Figure 5.6a shows that voltage and HFR response of the larger cell under continuous CO_2 dosing are similar to the behavior of stage 1 in Figure 5.6a. After passing through the 25 cm^2 AECS, Figure 3b shows that the cathode exhaust CO_2 concentration was 41 ppm. This value is larger than the cathode exhaust concentration observed for the five successive stages in Figure 5.4, 4 ppm. On the positive side, the cell was able to remove 90% of the incoming CO_2. However, a single 25 cm^2 AECS was not as effective as the five smaller sequential stages with fresh H_2 fed to each stage, where the exit CO_2 concentration was 4 ppm. The lower CO_2 removal efficiency may be due to CO_2 re-absorbed by the membrane downstream. However, it's

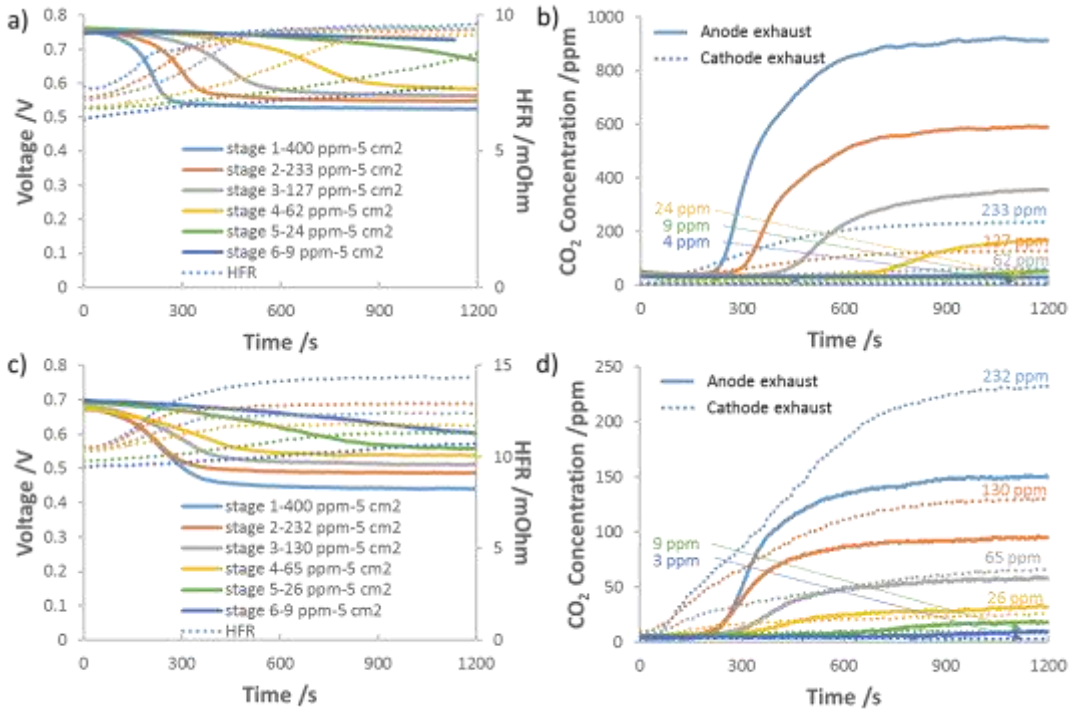

Figure 5.4 Performance of 5 cm^2 AECS cells with various concentrations of CO_2 in O_2. The numbers in the figure labels correspond to the concentration of CO_2 in O_2. All concentrations below 400 ppm were determined from the exhaust concentration of CO_2 from a previous cell with higher concentration, hence making the results represent the removal of CO_2 using a series of 5 cm^2 "stages". a) Voltage loss (solid lines) and HFR increase (dotted lines) for cells with an anode flowrate of 0.2 L/min. b) CO_2 concentration in the anode (solid lines) and cathode (dotted lines) effluent for cells with an anode flowrate of 0.2 L/min. c) Voltage loss (solid lines) and HFR increase (dotted lines) for cells with an anode flowrate of 1.0 L/min. d) CO_2 concentration in the anode (solid lines) and cathode (dotted lines) effluent for cells with an anode flowrate of 1.0 L/min. The results are color-coded based on CO_2 concentration entering the stage. All AECS cells were operated at a current density of 1.2 A/cm^2 at 54/56/70 °C with a GT72-5 AEM. The cathode flowrate was 1.0 L/min and the cathode backpressure was 30 psi.

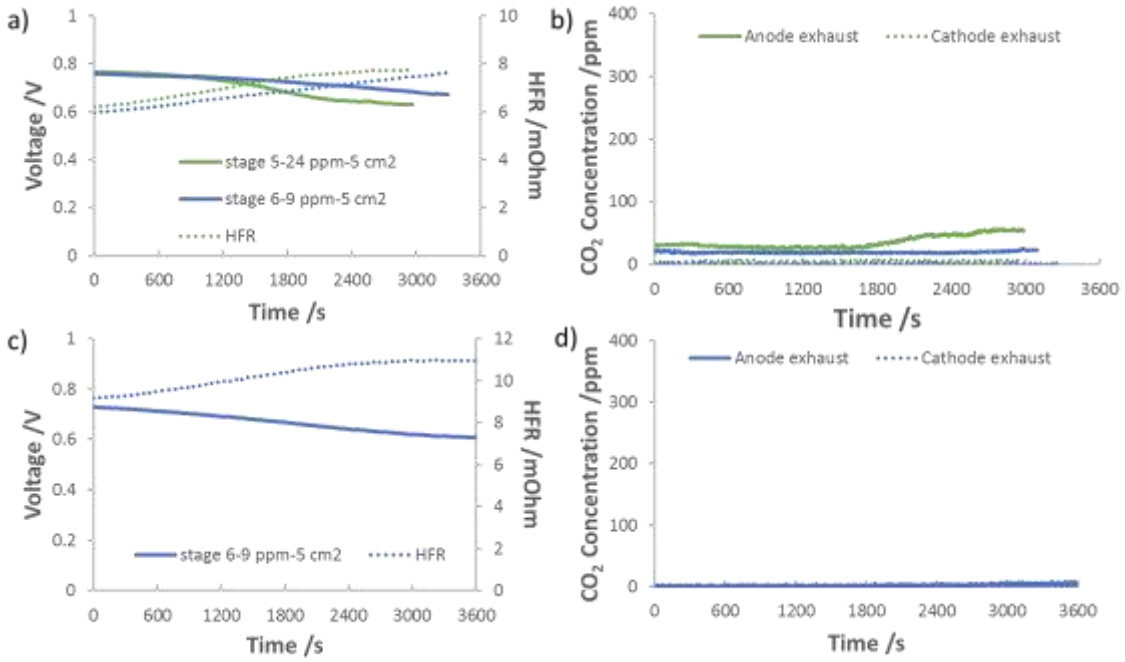

Figure 5.5 a) Extended measurement of voltage (solid lines) and HFR (dash lines) changes in stage 5 and 6 from the data in Figure 5.4a of the main document. The anode flowrate was 0.2 L/min. b) CO_2 concentration in the anode and cathode exhaust for the experiments in panel a; c) extended measurement of voltage (solid line) and HFR (dash line) changes in stage 6 from the data in Figure 5.4c of the main document. The anode flowrate was 1.0 L/min; d) CO_2 concentration in the anode and cathode exhaust from the experiments in panel c. The AECS was operating at 6 A with anode/cathode/cell temperatures of 54/56/70 ^oC. The AEM was GT72-5. The cathode backpressure was 30 psi. CO_2 was fed to the cathode at the labeled concentration at t = 0 s. The cathode flowrate was always 1.0 L/min.

also notable that cell engineering for the AECS might be a useful area for research. For example, the anode flowfield in the AECS could mimic segmented cells, essentially building smaller footprint "stages" inside of a larger flowfield. This is an area that is promising and will be worked on in the future.

Performing an additional experiment with a second 25 cm^2 stage (again with fresh UHP H_2 fed to the anode and changing the inlet CO_2 concentration, 41 ppm, to be equal to that leaving a single 25 cm^2 AECS) allowed very low levels of CO_2 in the oxygen to be achieved. Although the detector read < 1ppm CO_2 in the exhaust, approximately 4 ppm CO_2 can be removed by the water trap (see Figure 5.7). Thus, it is fair to say that the concentration of CO_2 leaving the second 25 cm^2 stage was < 5ppm CO_2. In fact, 4 ppm CO_2 would be expected if the 2^{nd} stage also removed 90% of the incoming CO_2, consistent with the results above.

The "blank" experiment in Figure 5.7 places a Teflon film between the flowfields instead of an MEA. This is meant to measure the actual CO_2 concentration fed to the cell when a specific amount of CO_2 is specified to the fuel cell test station. When 40 ppm CO_2 was demanded of the test station, 39 ppm was recorded when no water trap was used. 38 ppm was recorded with the water trap placed before the gas detector and no backpressure was applied. 36 ppm was recorded when 30 psi cathode backpressure was applied and the water trap was used. This shows that for most cases, the water trap does capture a small amount of CO_2 as discussed in the main manuscript. When 400 ppm CO_2 was fed to the cell, 374, 367, 369 ppm were recorded for the cases without water trap, with water trap, with water trap and backpressure, respectively.

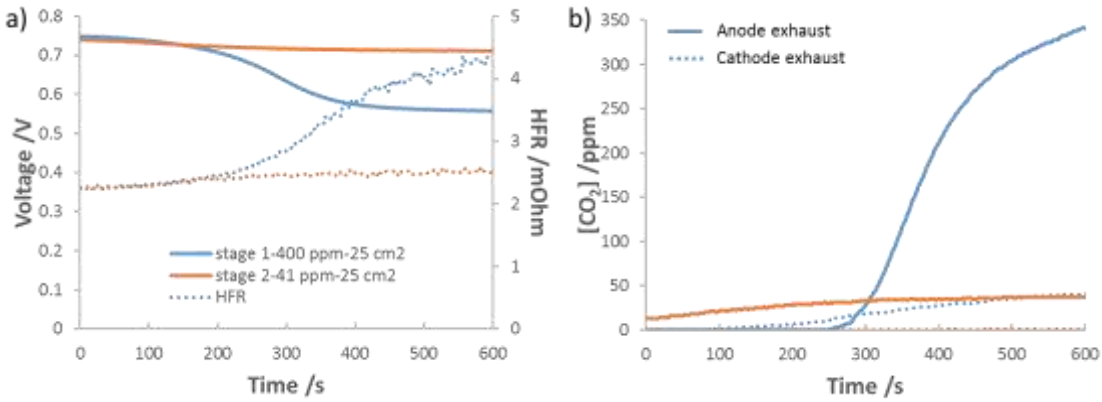

Figure 5.6 CO_2 scrubbing performance of a 25 cm^2 active area AECS operating at 1.0 A/cm^2 and anode/cathode/cell temperatures of 66/68/80 °C. The AEM was GT72-5. Both the anode and cathode flowrates were 1.0 L/min and the cathode backpressure was 30 psi. a) Voltage loss (solid lines) and HFR increase (dotted lines) following the introduction of CO_2 into the cathode; b) Concentration of CO_2 in the anode (solid lines) and cathode (dotted lines) effluent streams.

.

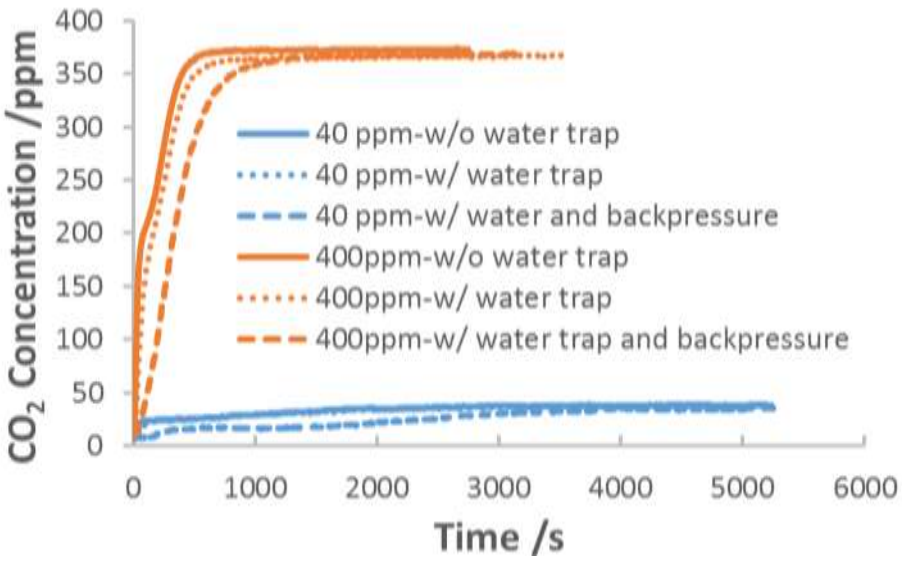

Figure 5.7 The blank experiment when Teflon is placed between the flowfields with no electrodes or membrane. Cathode feed streams containing 40 and 400 ppm were fed to the cell under three conditions: without water trap, with water trap, with water trap and 30 psi cathode backpressure. All of the concentrations shown here are from the cathode exhaust. The concentration leaving the anode was always zero since the Teflon film does not have sufficient CO_2 absorption and transport.

Next, instead of using stages – where just the inlet concentrations are controlled to mimic the interaction of multiple cells – two independently operated 25 cm^2 AECS cells were connected in series where the first cell was connected to FC test stand with pure reactant gases feeds. The second cell was connected directly to the first cell, using its exhaust. In this configuration, the CO_2 concentration leaving the water trap following Cell 2 was measured below 1 ppm, quite low (from the discussion above, the actual concentration leaving Cell 2 can be said to be < 5ppm). Previous work[54] suggests that this CO_2 concentration is not expected to be substantively harmful to AEMFC performance. Therefore, the cathode of a real operating 5 cm^2 AEMFC was connected to the cathode exhaust of Cell 2. Just as would be expected based on Figure 5.1, the AEMFC was fed fresh H_2. As shown in Figure 5.8, the performance of the AEMFC was essentially identical to a cell that was fed UHP O_2. This is very promising and the first demonstration of an AEMFC operating on an AECS-purified cathode feed.

5.2.3 CO_2 REMOVAL IN AECS CELLS USING INDUSTRIAL AIR

For AEMFCs, the ultimate goal is to use air as the oxidant, not oxygen. After confirming that the AECS concept is functionally sound, attention was turned to operating the cells on realistic CO_2-contanining air. These experiments were done under the same conditions and in the same manner as the O_2 experiments described previously. This includes investigating the CO_2 removal with increasing active area through a series of 5 cm^2 stages. The results are shown in Figure 5.9.

In general, when air was fed to the AECS cathode instead of oxygen, there was virtually no effect on the cell's ability to capture and transport CO_2. This is further supported by Figure 5.10 and surrounding discussion, which shows that carbonate uptake dynamics and

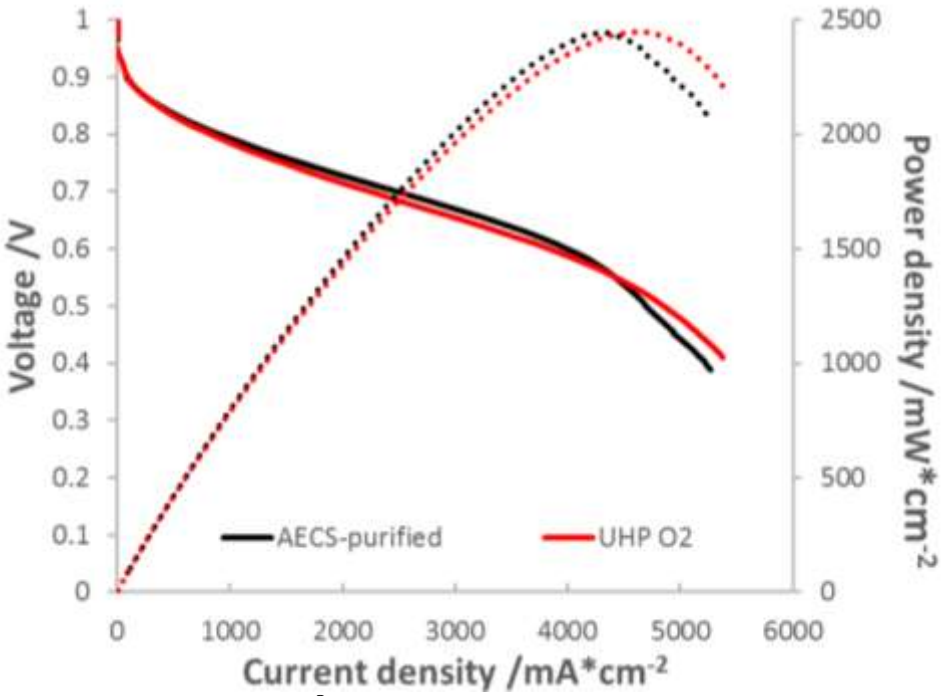

Figure 5.8 Performance of a 5 cm^2 AEMFC operating on both AECS-purified O_2 (starting from 400 ppm CO_2 in O_2) and UHP O_2. The AECS cells were operating at 1.2 A/cm^2 and temperatures of 66/68/80 °C with a GT72-5 AEM and cathode backpressure of 30 psi. The anode and cathode flowrates entering the AECS were both 1.0 L/min. The 5 cm^2 AEMFC was operated at temperatures of 66/68/80 °C and was assembled with a PtRu/C anode, Pt/C cathode and GT72-5 AEM.

the amount of charge that is carried by carbonate through the cell, are essentially the same between the air and O_2 case for a given inlet CO_2 concentration and operating current density. However, the cells operating on air (Figure 5.9) do so at a lower voltage than those operating on oxygen (Figure 5.4), even before carbonation occurs, due to lower oxygen activity and increased cathode overpotentials.

Next, 25 cm^2 AECS cells were assembled, fed with industrial air and operated in two configurations. The first configuration was a stand-alone 25 cm^2 cell, which was able to reduce the CO_2 concentration from 400 ppm to 68 ppm. On the positive side, the efficacy of this cell in removing CO_2 was quite consistent over 150 hr of continuous operation (Figure 5.11a), although the cell operating voltage did decline slightly during that time. Also, just like the O_2 case, the larger 25 cm^2 stage was not quite as effective as 5 stages with 5 cm^2 active area – supporting the idea discussed above that advanced flowfields might be able to boost the performance of AECS cells with large active areas. In the second configuration, two 25 cm^2 AECS cells were connected in series and also operated for 150 hr. As shown in Figure 5.11a, such a tandem configuration was able to create an effluent stream with consistently low CO_2 concentration, though the operating voltage did decline moderately during the test – most likely due to sub-optimal AECS operating conditions, such as imbalanced cell-level water, which is a well-known contributor to AEM-based device performance decline. Finally, the exhaust from the series AECS configuration was fed to a 5 cm^2 active area AEMFC. The results are shown in Figure 5.11b along with the performance of the same cell operating on CO_2-free air before any exposure to CO_2. The two curves nearly perfectly overlap, showing that it is possible to operate an AEMFC on AECS-purified air.

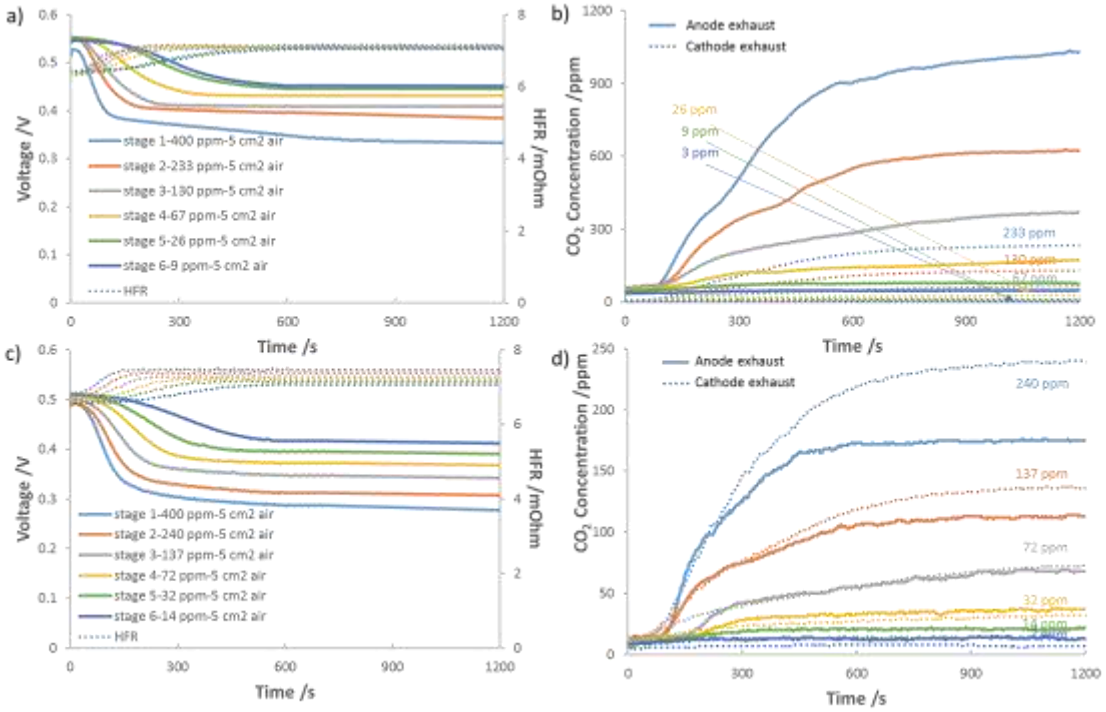

Figure 5.9 Performance of an AECS as a function of the number of 5 cm^2 stages that were implemented, starting with 400 ppm CO_2 in air. a) Voltage loss (solid lines) and HFR increase (dotted lines) for cells with an anode flowrate of 0.2 L/min. b) CO_2 concentration of in the anode (solid lines) and cathode (dotted lines) effluent for cells with an anode flowrate of 0.2 L/min. c) Voltage loss (solid lines) and HFR increase (dotted lines) for cells with an anode flowrate of 1.0 L/min. d) CO_2 concentration of in the anode (solid lines) and cathode (dotted lines) effluent for cells with an anode flowrate of 1.0 L/min. The results are color-coded based on CO_2 concentration entering the stage. All cells were operated at a current density of 1.2 A/cm^2 at 54/46/70 °C with a GT72-5 AEM. The cathode flowrate was 1.0 L/min and the cathode backpressure was 30 psi.

For applications such as AEM-based electrochemical CO_2 capture [82], visualizing the steady-state transport of CO_2/CO_3^{2-} from the cathode to the anode in an operating device is important and shown in Figure 5.10. The ratio of the number of electrons transferred per molecule of CO_2 emitted at the anode as a metric (e^-/CO_2) is used which is easily measurable experimentally.

$$\log\left(\frac{e^-}{CO_2}\right) = \left[\log i - \log i_o + \frac{\alpha}{n}\log\frac{P_{O2}[OH^-]^4 K_{b2}^4}{P_{H2O}^2[CO_3^{2-}]^4}\right] - \alpha \log P_{CO2} \quad (2.10)$$

The equation above was thoroughly derived in Chapter 2.[53] It was shown that at a defined current density (where everything in the square brackets in Equation 2.10 Are constant), there is a linear relationship between the log e^-/CO_2 and log P_{CO2} with a negative slope equal to the effective ORR transfer coefficient. The slope in Figure 5.10 is approximately -0.80, which is consistent with measurements of the effective transfer coefficient for the ORR in operating fuel cells (should be ~ -1)[83,84]. With different oxidant of simulated oxygen and air and the same current, two lines overlap, showing its independency of reactant gas type.

Regarding the relative size of the AEMFC and AECS, it is acknowledged here that both demonstrations of AECS-purified streams operating AEMFCs (O_2 and air in Figure 5.4 and Figure 5.9b, respectively) had a 5 cm^2 cell that was leveraging the work of an AECS with an effective area of 50 cm^2. However, these cells are clearly oversized. Previous work[54] as well as the flatness of the voltage response for the later-stages in Figures 5.4, 5.6 and 5.9 suggest that the true target might be to reduce the CO_2 concentration to below 20-40 ppm (though a thorough study on the effects of the fed AEMFC concentration is needed) might be acceptable. This is shown in Figure 5.12 where an AEMFC is operated with an inlet CO_2 concentration of 21 ppm in air with no ill effects. Operating on CO_2-containing

O_2 or air, the AECS needed 4 stages, or 20 cm^2 total active area (with a current density of 1.2 A/cm^2) to reduce the CO_2 concentration from 400 ppm to a value between 20 and 40 ppm.

As discussed above, the 1.0 L/min flowrate is enough O_2 to operate a 219 cm^2 total active area at 1.0 A/cm^2. This includes the operation of the AECS because it also consumes O_2. So, taking the O_2 consumption and different operating currents into consideration, the 20 cm^2 AECS operating at 1.2 A/cm^2 would be expected to support an AEMFC with an active area of 195 cm^2, giving a relative size ratio of around 1:9.8. Of course, this will be affected by switching to air. The lower molar flowrate of O_2 in air vs pure oxygen, a 1.0 L/min flowrate (6.8 vs. 34 mmol/min at 80^oC) of air is able to support a total active area of 44 cm^2 (at 1.0 A/cm^2) This means that the present efficiency for CO_2 removal of the AECS would require an AEMFC:AECS ratio around 1:1. Though this is not ideal, it should be remembered that the AECS also generates power, and each stage produces more and more as the CO_2 is removed – where at some point the AECS performance can be nearly indistinguishable from the AEMFC –until H_2 depletion kicks in. It should be noted that if the AECS is operated in the proposed fashion, the anode stream will contain N_2 and quite a bit of CO_2, meaning that the stream cannot be recycled for use later. Therefore, it would be beneficial from an engineering and efficiency perspective if the last stages of the AECS almost completely consumed the H_2. This may cause the last stage or stages to generate very little power, but simply polish the CO_2 level. It should also be noted that although Figure 5.1 presents the concept as two distinct stacks, it may in fact be better to not create two separate stacks, but to simply re-design the flowfields to designate certain cells in the

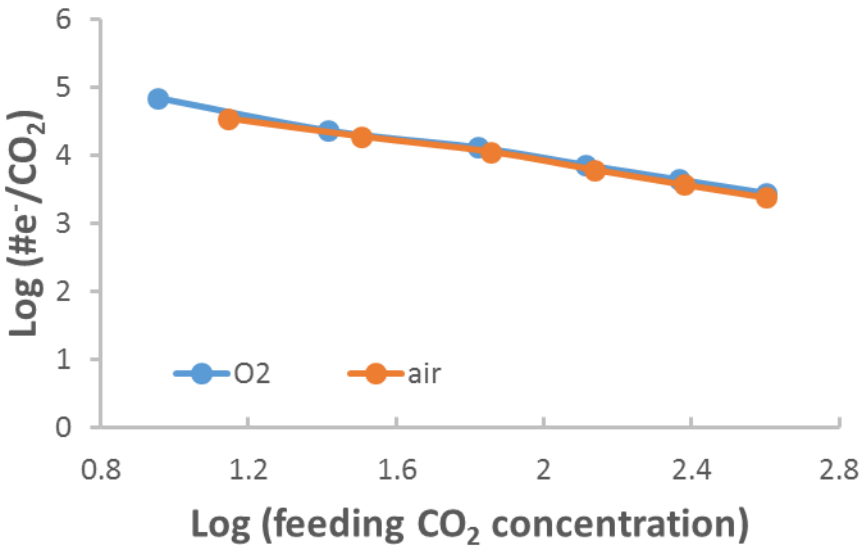

Figure 5.10 The relationship between the cathode CO_2 feed concentration and number of electrons that pass through the external circuit per CO_2 molecule that is transported from the cathode to the anode. This is related to the portion of the charge that is carried by CO_3^{2-}. The data here is taken from Figures 5.4 and 5.9 for simulated oxygen and industrial air as reactant gas, respectively.

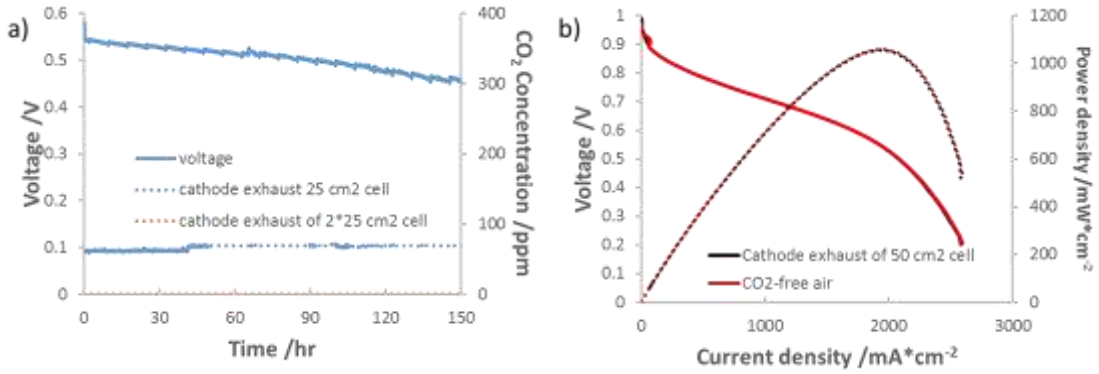

Figure 5.11 a) 150-hour AECS stability and performance using industrial air as oxidant. Two 25 cm^2 AECS cells were operated in series at an operating current of 600 mA/cm^2 at 66/68/80 °C with 1.0 L/min anode and cathode flowrates, and a cathode backpressure of 30 psi. The voltage curve shows the voltage operation stability of the first cell in the series. b) Polarization curves for 5 cm^2 active area AEMFCs bed with either CO_2-free air or AECS-purified air. Cell was constantly running at 600 mA/cm^2, 66/68/80 °C, 1.0 L/min anode and CO_2-free air flowrate, nearly 1.0 L/min former cathode exhaust flowrate and without backpressure.

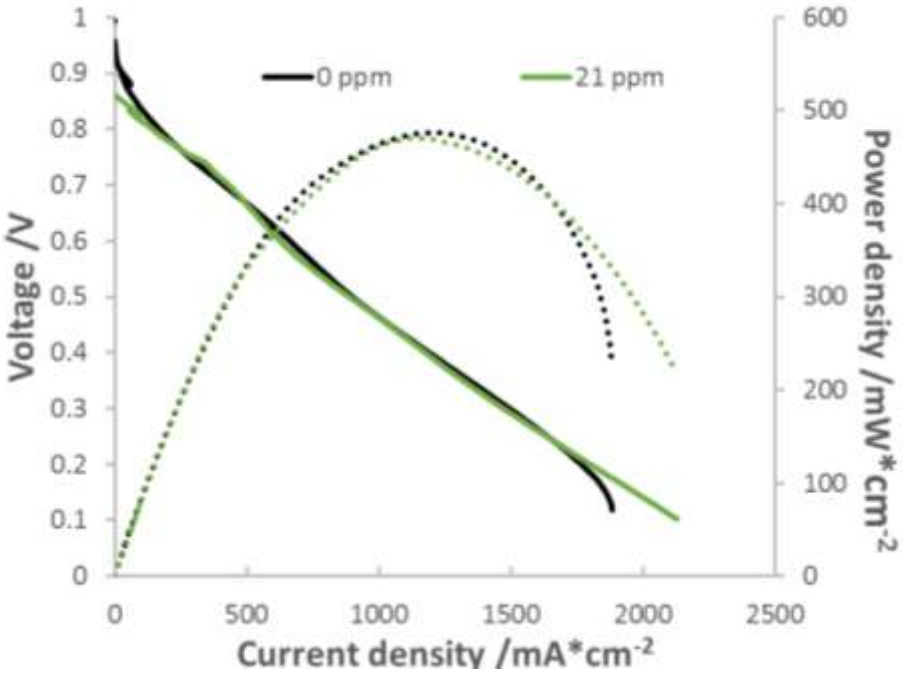

Figure 5.12 Performance of a 5 cm^2 AEMFC operating with CO_2-free air fed to the cathode and with 21 ppm air. The cell was operated at anode/cathode/cell temperatures of 54/46/70 °C with a GT72-5 AEM. The anode and cathode flowrates were 1.0 L/min and were applied without backpressure.

AEMFC stack as those operating with CO_2 and then use a more conventional setup once the CO_2 is removed.

Finally, as discussed above, additional research is needed with the goal of increasing CO_2 uptake in the AECS, where it may be possible to get a more favorable ratio for the active areas of the AEMFC and AECS. Some designs may even sacrifice the power output of the AECS, perhaps even to zero, but also increase the portion of charge carried by carbonate – which would decrease the needed active area and reduce the amount of oxygen consumed. Perhaps such a design will also leverage the fact that H_2 flowrate leaving the AECS needs to be fully depleted to avoid fuel-derived inefficiencies. Such designs will be working on moving forward. It should also be noted that the discussion above only emphasizes increasing the active area of the cells as a means of scrubbing more CO_2 from the AECS cathode. However, this is not the only way to increase the amount of CO_2 removed from the device. Alternative approaches could also include changing the channel dimensions, alternative flow field designs, new catalyst layers and gas diffusion layers, and increasing the current density.

5.3 SUMMARY

In this study, the performance of an anion exchange CO_2 separator (AECS) was reported for the first time. The CO_2 removal efficiency of this first-generation AECS was determined both under O_2 and CO_2 operation. Then, two AECS cells applied in series were used to purify a 1.0 L/min cathode flow with 400 ppm CO_2, which was fed to an operating AEMFC. It was shown, for the first time, that an AECS can be used to purify an AEMFC cathode feed and that the AEMFC could be operated with essentially no loss in performance.

CHAPTER 6: CONCLUSIONS

Before the work in this thesis was done, most literature discussion around AEMFC carbonation hypothesized: 1) that the negative effect of carbonation is limited to an increase in the Ohmic resistance; and/or 2) that it was possible "self-purge" or forcefully decarbonate operated AEMFCs by operating at a current density > 1 A cm^{-2}, thereby eliminating any CO_2-related voltage loss. However, this study definitively shows that neither of these assertions are correct.

This work was the first experimental examination of its kind, providing the first studies the dynamics of cell carbonation and its effect on AEMFC performance over a wide range of operating currents (0.2 – 2.0 A cm^{-2}), temperatures (60 – 80°C) and CO_2 concentrations in the reactant gases (5 – 3200 ppm). The resulting data allowed for new fundamental relationships to be developed and for the root causes of increased polarization in the presence of CO_2 to be quantitatively probed and deconvoluted into Ohmic, Nernstian and charge transfer components, with the Nernstian and charge transfer components controlling the cell behavior under conditions of practical interest.

Introduction of CO_2 into AEMFCs results in cell carbonation that can cause performance losses that add up to hundreds of millivolts. Therefore, it was important to find strategies and operational protocols for AEMFCs that minimize these overpotentials. The impacts of the anode and cathode flowrate were investigated, as well as the cell hydration level, on the extent of cell carbonation and cell polarization. Key findings

included: (1) decreasing the cathode flowrate generally decreases the total CO_2-related voltage loss while changing the anode flowrate has a minimal effect; and (2) increasing cell hydration helps to mitigate the performance loss in the presence of CO_2. Operational combinations are found that significantly reduced the CO_2 penalty compared to the present literature.

Although the chemical mechanisms for how carbonation leads to voltage loss in operating AEMFCs are known, the way those mechanisms are affected by the properties of the AEM had also not been elucidated. Therefore, several high-functioning AEMs from the literature were studied for their carbonation dynamics and it was found that the ionic conductivity of the AEM plays the most critical role in the CO_2-related voltage loss from carbonation, with the degree of AEM crystallinity playing a minor role. In short, higher conductivity—resulting either from a reduction in the membrane thickness or a change in the polymer chemistry—results in faster CO_2 migration and emission from the anode side. Although this does lead to a lower overall degree of carbonation in the polymer, it also increases CO_2-related voltage loss. Additionally, an *operando* neutron imaging cell was used to show that as AEMFCs become increasingly carbonated, their water content is reduced, which further drives down cell performance.

After understanding how cell carbonation affects AEMFCs, it became clear that a CO_2 scrubber is going to be needed to remove CO_2 from cathode air stream. However, most modern processes to do this are energy intensive and would complicate the system-level balance-of-plant. Therefore, an appropriate method for CO_2 filtering needs to be found. The last technical Chapter of this thesis focused on an electrochemical solution where CO_2 removal would still generate power, but not expose an entire AEMFC stack to carbonation conditions. Such a system consisted of two AEMFCs in series. The first AEMFC, which

acted as an anion exchange CO_2 separator, was relatively small and served to scrub CO_2 from the air. The AECS is powered by the hydrogen bleed from the second (i.e., main) AEMFC. A small amount of hydrogen is bled from the recycled hydrogen used in the main AEMFC to mitigate impurity build-up, including nitrogen gas from diffusion across its membrane. The second, main AEMFC operates on the purified air output from the AECS and fresh H_2. This work shows that it is possible to use an AECS to lower the CO_2 concentration in the AEMFC input air stream to values low enough that the main AEMFC can be operated stably for extended periods, where 150 h was demonstrated here. Also, AEMFCs were operated on AECS-purified air without experiencing a performance penalty. Lastly, the relative geometric active area of the AEMFC and AECS devices were evaluated and discussed.

CHAPTER 7: RECOMMENDATION FOR FUTURE WORK

The future for fuel cell technology is bright, filled with opportunity, and ever- changing. In this area, an overwhelming amount of the attention and investment has gone to PEMFCs. Academia, national labs and industry have worked together to overcome many of the technological and institutional barriers to the development of PEMFCs. However, the widespread deployment of PEMFCs is still elusive due to their high cost, both at the cell-level and systems-level. One of the most promising solutions to overcome the cost barriers for incumbent PEMFCs is to completely re-think the operating environment. Anion exchange membrane fuel cells can offer all of the advantages of PEMFCs (compact designs, high power density, etc.), but their less harsh environment allows a wider range of low-cost materials to be used for several cell components, including the bipolar plates, membranes, and catalysts[5,13]. To further lower the cost of the AEMFC and enhance its deployment, carbonation is a serious issue that inevitability must be faced and solved.

Though this thesis extensively studied the behavior of CO_2 and AEMFC carbonation during operation, there are still many questions left unknown. First, the effect of ionomer with varying IEC values and chemistries, hydrophilicities are under-discovered. All these ionomer properties are dictated by water interactions and ionic conductivity which were proved in this thesis to be significant affecting factors. Second, common impurities in the anode stream, such as ammonia and CO, also need to be considered for further study. It is also possible to aim for using mixed fuel instead of pure H_2. This strategy could further

bring the cost down and maximize the fuel utilization and power production. Third, the design of fuel cell hardware especially bipolar plates and electrodes could be helpful for reducing carbonation. For example, the addition of an interlayer composed of carbon and ionomer could boost the CO_2 removal as it can increase the interacting time between CO_2 and the catalyst. Below, each of these three main areas for future work are briefly discussed.

7.1 EFFECT OF IONOMER ON AEMFC CARBONATION

Ionomer properties such as IEC and hydrophilicity are of interest as they provide a different response in the polymer – more specifically they modify the OH^- conductivity and water uptake. In an AEMFC, hydrophobic ionomer can help to reject water and hydrophilic ionomer can help to move water around quickly or retain it in the electrodes. Careful control over the combination of anode and cathode ionomer can improve performance.[126–128] In this project, to make sure that the results were internally consistent, the same ionomer was used for all experiments. Because of the influence of the ionomer on performance, ionic conductivity and water uptake a future study should be designed that studies the impact of ionomer over a wide range of chemistries and properties. First, ionomers with different IECs but same chemistry should be used while maintaining all of the other conditions, such as cell operating conditions, electrode composition, AEM and so on. The cells would be operated at constant current. Voltage and HFR changes along with CO_2 concentrations leaving the cell system would be recorded. As was done throughout this thesis, the data would be used to deconvolute the observed voltage losses into the three main mechanisms.

Secondly, ionomers with same IEC but different hydrophilicity would be investigated while keeping the experimental procedure. As usual, its voltage and HFR response with

and without the introduction of CO_2 would be measured, the dynamic CO_2 concentrations that leave the FC system would be recorded. The detailed mechanisms would be analyzed. CO_2 resistance according to the equilibration time, voltage and HFR changes and CO_2 removal rate would be evaluated.

7.2 IMPACT OF ANODE IMPURITIES ON AEMFC PERFORMANCE

Similar to CO_2, first a method would need to be developed for in-cell NH_3 titration experiments. Then, 0-1% ammonia would be added into the anode stream (simulating H_2 production from ammonia). Next, one would need to determine if ammonia is taken up into the AEM and transported from the anode to the cathode during either normal operation or startup-shutdown. The study would need to conclude whether there are any transport issues when feeding ammonia or if the ammonia would poison either the anode or cathode electrode. Last, because there is a possibility for CO_2 and NH_3 to interact[129], it would be important to investigate the combined effects of ammonia and CO_2 on operating AEMFCs. If I were to design the study, the following experiments would be conducted.

- O_2 fed to the cathode, H_2 fed to the anode with up to 1 % NH_3. The NH_3 concentration leaving both the anode and cathode would be measured in real time. Cells would be operated at constant current, measuring the voltage and HFR changes in the absence of NH_3. NH_3 will then be dosed to the cell under constant flow, concentration will be changed between $0 \rightarrow 1\%$. The cell would be allowed to reach steady-state. The NH_3 would be shut off and the cell would rest holding at constant current. If needed, a step for forced ammonia removal would be developed.

- NH_3 would be introduced directly into the cathode. Pure H_2 would be fed to the anode. O_2 and air would be fed to the cathode separately (which allows for the separation of oxygen concentration effects from true NH_3 uptake effects) with increasing amount of NH_3. The NH_3 concentration leaving both the anode and cathode would be measured in real time. Cells would be operated at constant current, measuring the voltage and HFR in the absence of NH_3. NH_3 would then be dosed to the cell under constant flow, the concentration will be changed between $0 \rightarrow 100$ ppm. The cell would be allowed to come to steady-state. The NH_3 would be shut off and the cell would be allowed to rest. If needed, a step for forced ammonia removal will be developed.

- Third, CO_2 and NH_3 would be fed to operating cells at the same time. In a recent study, Katayama[129] et al. claimed that adding NH_3 to the anode of an operating AEMFC can help to improve cell tolerance to CO_2. However, this was done on relatively poor performing cells. Their claim was that bicarbonate was consumed, producing $H_2NCO_2^-$ and H_2O. If this were the case, the Nernstian voltage loss would be reduced as the anode pH would not be able to shift down during operation. To test this, experiments would be done with 400 ppm CO_2 fed to the cathode with NH_3 in the H_2 stream up to 1%. Polarization measurements at 80^oC, 0 kPa backpressure, H_2, NH_3/O_2, CO_2 and H_2, NH_3/air, CO_2 reacting gases would be done. Several experiments would be done under these conditions. First the CO_2 would be fed to the cell and released and the voltage losses deconvoluted in the same way as earlier in this

thesis. Long-term voltage stability measurements would be done for 100 h, using standard materials sets at operating current: 600 mA/cm^2. During this time, the voltage and HFR changes would be measured. Also, EIS would be done before and after testing at both OCV and under the operating current. Standard electrode materials would be used, e.g. 40% Pt/Vulcan at the cathode and 60% PtRu/Vulcan at the anode, GT72-5 AEM, Toray 060 with 5% PTFE GDL.

7.3 CATALYST LAYER, GAS DIFFUSION LAYER AND FLOW FIELD DESIGN

7.3.1 CATALYST LAYER DESIGN

The meticulous and integrated design of catalyst layer components and their morphological structure are essential for optimizing the fuel cell mass-transfer and catalytic performance. As above mentioned, adding an interlayer before catalyst coating would introduce extra porosity and increase the interaction time between the CO_2 and polymer. The introduction of interlayer has been widely applied in PEMFC for porous electrode design[130–132]. It tends to lead to a relatively thicker catalyst layer. If this were done in an AEMFC, there would be a longer OH^- transmission pathway and larger ion-transfer resistance. Several compositions of interlayer would be tried: i) Vulcan carbon; ii) Vulcan carbon + PTFE; iii) Vulcan carbon + PTFE + ionomer; and iv) Vulcan carbon + ionomer. The loading of each composition would be considered separately. PTFE would be used as hydrophobic media and ionomer would allow the anionic conductivity to be enhanced – all would be beneficial factors in FC performance.

7.3.2 GAS DIFFUSION LAYER DESIGN

The gas diffusion layer design plays an important role in the water management for AEM fuel cells. For example, transport of liquid water away from the active area of electrodes can be enhanced by the hydrophobic property of the micro-pores and the gradient of pore size[133,134]. Thus, the design of the GDL will have impact on AEMFC carbonation. The choice of GDL would be investigated by either purchasing a series of commercially available materials or by developing methods to modify a single material in-house. Carbon paper is usually credited as providing high conductivity, gas diffusivity and low cost. The detailed parameters such as: i) thickness, ii) porosity, iii) pore size, including gradiented pore size, and iv) hydrophobicity would be studied.

7.3.3 FLOW FIELD DESIGN

In addition to GDE designs, the choice of flow-channel geometry in the bipolar plates also has significant impacts on water management. Based on conductive solid materials (graphite or metal), a significant amount of research have been done on various flow channel configurations, such as pin-type, straight channel, serpentine channel, and interdigitated channel.[135–137] Materials for building bipolar plates, such as carbon and carbon composites plates, coated metallic plates, etc. have been widely investigated as well.[138,139] It has been shown that some designs provide advantages over others, allowing mass transport process to be improved. It is also possible to create configurations that reduce cost and/or improve manufacturability. However, it is still difficult to achieve the optimal water distribution throughout the flow channels (gas inlet, gas outlet, active area) simultaneously. This is particularly important in AEMFCs where a lot more water is

provided to the anode than even the cathode in PEMFCs. Unfortunately, flow field studies have been almost exclusively focused on PEMFCs, and research on AEMFC flow fields is scarce. In such a study, several flow field types would be investigated such as serpentine, parallel, and interdigitated. The serpentine-type flow field has good gas distribution, can minimize flooding while suffering from gas depletion and large pressure drop[136]. Parallel-type flow field bipolar plates experience less pressure drop but worse gas distribution[138]. Interdigitated bipolar plates have been reported to show improvement on water management[138] because they use forced-convection flow in the GDL to push reactant gases into the electrodes, which can result in lower mass-transport losses. The forced gas flow can help remove liquid water to avoid flooding, but also can promote dry out with low humidity reactants. However, the pressure drop experienced here can be the highest of all flow field types.

REFERENCES

1. R. K. N. Kirubakaran, Annamalai, Shailendra Jain, *Renew. Sustain. Energy Rev.*, **13**, 2430–2440 (2009).

2. T. J. Omasta, thesis, University of Connecticut (2018).

3. B. P. Setzler, Z. Zhuang, J. A. Wittkopf, and Y. Yan, *Nat. Nanotechnol.*, **11**, 1020–1025 (2016).

4. M. M. Whiston, I. L. Azevedo, S. Litster, K. S. Whitefoot, and C. Samaras, *PNAS*, **116**, 4899–4904 (2019).

5. J. R. Varcoe, P. Atanassov, D. R. Dekel, A. M. Herring, M. A. Hickner, P. A. Kohl, A. R. Kucernak, W. E. Mustain, K. Nijmeijer, K. Scott, T. Xu, and L. Zhuang, *Energy Environ. Sci.*, **7**, 3135–3191 (2014).

6. G. Merle, M. Wessling, and K. Nijmeijer, *J. Memb. Sci.*, **377**, 1–35 (2011).

7. E. Gülzow and M. Schulze, *J. Power Sources*, **127**, 243–251 (2004).

8. A. Sen A. Tewari, V. Sambhy, M. Urquidi Macdonald, *J. Power Sources*, **153**, 1–10 (2006).

9. L. A. Adams, S. D. Poynton, C. Tamain, R. C. T. Slade, and J. R. Varcoe, *ChemSusChem*, **1**, 79–81 (2008).

10. K. K. V. Cifrain M, *J. Power Sources*, **127**, 234–242 (2004).

11. K. Kordesch, V. Hacker, J. Gsellmann, M. Cifrain, G. Faleschini, P. Enzinger, R. Fankhauser, M. Ortner, M. Muhr, and R. R. Aronson, *J. Power Sources*, **86**, 162–165 (2000).

12. J. R. Varcoe and R. C. T. Slade, *Fuel Cells*, **5**, 187–200 (2005).

13. S. Gottesfeld, D. R. Dekel, M. Page, C. Bae, Y. Yan, P. Zelenay, and Y. S. Kim, *J. Power Sources*, **375**, 170–184 (2018).

14. W. E. Mustain, *Curr. Opin. Electrochem.*, **12**, 233–239 (2018).

15. J. R. Varcoe, *Phys. Chem. Chem. Phys.*, **9**, 1479–1486 (2007).

16. S. Gu, R. Cai, T. Luo, K. Jensen, C. Contreras, and Y. Yan, *ChemSusChem*, **3**, 555–558 (2010).

17. D. S. Kim, C. H. Fujimoto, M. R. Hibbs, A. Labouriau, Y. K. Choe, and Y. S. Kim, *Macromolecules*, **46**, 7826–7833 (2013).

18. M. Mandal, G. Huang, and P. A. Kohl, *ACS Appl. Energy Mater.*, **2**, 2447–2457 (2019).

19. L. Wang, J. J. Brink, and J. R. Varcoe, *Chem. Commun.*, **53**, 11771–11773 (2017).

20. G. Huang, M. Mandal, X. Peng, A. C. Yang-Neyerlin, B. S. Pivovar, W. E. Mustain, and P. A. Kohl, *J. Electrochem. Soc.*, **166**, F637–F644 (2019).

21. M. Mandal, G. Huang, N. U. Hassan, X. Peng, T. Gu, A. H. Brooks-starks, B. Bahar, W. E. Mustain, and P. A. Kohl, *J. Electrochem. Soc.*, **167**, 054501 (2020).

22. T. J. Omasta, X. Peng, H. A. Miller, F. Vizza, L. Wang, J. R. Varcoe, D. R. Dekel, and W. E. Mustain, *J. Electrochem. Soc.*, **165**, J3039–J3044 (2018).

23. T. J. Omasta, L. Wang, X. Peng, C. A. Lewis, J. R. Varcoe, and W. E. Mustain, *J. Power Sources*, 205–213 (2017).

24. T. J. Omasta, A. M. Park, J. M. Lamanna, Y. Zhang, X. Peng, L. Wang, D. L. Jacobson, J. R. Varcoe, D. S. Hussey, B. S. Pivovar, and W. E. Mustain, *Energy Environ. Sci.*, **11**, 551–558 (2018).

25. S. M. Alia, C. Ngo, S. Shulda, M. Ha, A. A. Dameron, J. N. Weker, K. C. Neyerlin, S. S. Kocha, S. Pylypenko, and B. S. Pivovar, *ACS Omega*, **2**, 1408−1418 (2017).

26. X. Peng, D. Kulkarni, Y. Huang, T. J. Omasta, B. Ng, Y. Zheng, L. Wang, J. M. Lamanna, D. S. Hussey, J. R. Varcoe, I. V Zenyuk, and W. E. Mustain, *Nat. Commun.*, **11**, 1–10 (2020).

27. S. M. Alia and B. S. Pivovar, *J. Electrochem. Soc.*, **165**, F441–F455 (2018).

28. L. Xie and D. W. Kirk, *Electrocatalysis*, **11**, 292–300 (2020).

29. N. U. Hassan, M. Mandal, G. Huang, H. A. Firouzjaie, P. A. Kohl, and W. E. Mustain, *Adv. Energy Mater*, **10**, 2001986 (2020).

30. W. E. Mustain, M. Chatenet, M. Page, and Y. S. Kim, *Energy Environ. Sci*, **13**, 2805–2838 (2020).

31. X. Peng, T. J. Omasta, E. Magliocca, L. Wang, J. R. Varcoe, and W. E. Mustain, *Angew.Chem. Int.Ed.*, **58**, 1046–1051 (2019).

32. T. Kimura and Y. Yamazaki, *Electrochemistry*, **79**, 94–97 (2011).

33. A. Amel, N. Gavish, L. Zhu, D. R. Dekel, M. A. Hickner, and Y. Ein-Eli, *J. Memb. Sci.*, **514**, 125–134 (2016).

34. C. Chen, Y. L. S. Tse, G. E. Lindberg, C. Knight, and G. A. Voth, *J. Am. Chem. Soc.*, **138**, 991–1000 (2016).

35. M. L. Di Vona, D. Marani, A. D'Epifanio, S. Licoccia, I. Beurroies, R. Denoyel, and P. Knauth, *J. Memb. Sci.*, **304**, 76–81 (2007).

36. M. L. Disabb-Miller, Z. D. Johnson, and M. A. Hickner, *Macromolecules*, **46**, 949–956 (2013).

37. C. W. K. Kiss A. M., Myles T. D., Grew K. N., Peracchio A. A., Nelson G. J., *J. Electrochem. Soc.*, **160**, F994–F999. (2013).

38. K. N. Grew, D. Chu, and W. K. S. Chiu, *J. Electrochem. Soc.*, **157**, B1024 (2010).

39. M. G. Marino, J. P. Melchior, A. Wohlfarth, and K. D. Kreuer, *J. Memb. Sci.*, **464**, 61–71 (2014).

40. Y. K. Choe, C. Fujimoto, K. S. Lee, L. T. Dalton, K. Ayers, N. J. Henson, and Y. S. Kim, *Chem. Mater.*, **26**, 5675–5682 (2014).

41. T. P. Pandey, H. N. Sarode, Y. Yang, Y. Yang, K. Vezzù, V. Di Noto, S. Seifert, D. M. Knauss, M. W. Liberatore, and A. M. Herring, *J. Electrochem. Soc.*, **163**, H513–H520 (2016).

42. N. Ziv, W. E. Mustain, and D. R. Dekel, *ChemSusChem*, **11**, 1136–1150 (2018).

43. U. Krewer, C. Weinzierl, N. Ziv, and D. R. Dekel, *Electrochim. Acta*, **263**, 433–446 (2018).

44. M. R. Gerhardt, L. M. Pant, and A. Z. Weber, *J. Electrochem. Soc.*, **166**, F3180–F3192 (2019).

45. S. Matz, B. P. Setzler, C. M. Weiss, L. Shi, S. Gottesfeld, and Y. Yan, *J. Electrochem. Soc.*, **168**, 014501 (2021).

46. S. Suzuki, H. Muroyama, T. Matsui, and K. Eguchi, *Electrochim. Acta*, **88**, 552–558 (2013).

47. S. Watanabe, K. Fukuta, and H. Yanagi, *ECS Trans.*, **33**, 1837–1845 (2010).

48. K. Fukuta, H. Inoue, S. Watanabe, and H. Yanagi, *ECS Trans.*, **19**, 23–27 (2009).

49. J. Peng, A. L. Roy, S. G. Greenbaum, and T. A. Zawodzinski, *J. Power Sources*, **380**, 64–75 (2018).

50. T. P. Pandey, A. M. Maes, H. N. Sarode, B. D. Peters, S. Lavina, K. Vezzù, Y. Yang, S. D. Poynton, J. R. Varcoe, S. Seifert, M. W. Liberatore, V. Di Noto, and A. M. Herring, *Phys. Chem. Chem. Phys. Phys. Chem. Chem. Phys*, **17**, 4367–4378 (2015).

51. A. G. Divekar, A. C. Yang-Neyerlin, C. M. Antunes, D. J. Strasser, A. R. Motz, S. S.

Seifert, X. Zuo, B. S. Pivovar, and A. M. Herring, *Sustain. Energy Fuels*, **4**, 1801–1811 (2020).

52. A. G. Divekar, B. S. Pivovar, and A. M. Herring, *ECS Trans.*, **86**, 643–648 (2018).

53. Y. Zheng, T. J. Omasta, X. Peng, L. Wang, J. R. Varcoe, S. Pivovar, and W. E. Mustain, *Energy Environ. Sci.*, **12**, 2806–2819 (2019).

54. Y. Zheng, G. Huang, L. Wang, J. R. Varcoe, P. A. Kohl, and E. Mustain, *J. Power Sources*, **467**, 228350 (2020).

55. K. N. Grew, X. Ren, and D. Chu, *Electrochem. Solid-State Lett*, **14**, B127 (2011).

56. Y. Zheng, L. N. Irizarry Colón, N. Ul Hassan, E. R. Williams, M. Stefik, J. M. LaManna, D. S. Hussey, and W. E. Mustain, *Membranes (Basel).*, **11** (2021) https://www.mdpi.com/2077-0375/11/2/102.

57. C. G. Arges and L. Zhang, *ACS Appl. Energy Mater.*, **1**, 2991–3012 (2018).

58. A. P. Muroyama, A. Beard, B. Pribyl-Kranewitter, and L. Gubler, *ACS ES&T Eng.*, **1**, 905–916 (2021).

59. K. N. Grew and W. K. S. Chiu, *J. Electrochem. Soc.*, **157**, B327 (2010).

60. T. D. Myles, K. N. Grew, A. A. Peracchio, and W. K. S. Chiu, *J. Power Sources*, **296**, 225–236 (2015).

61. Z. Siroma, S. Watanabe, K. Yasuda, K. Fukuta, and H. Yanagi, *ECS Trans.*, **33**, 1935–1943 (2010).

62. H.-S. Shiau, I. V. Zenyuk, and A. Z. Weber, *J. Electrochem. Soc.*, **164**, E3583–E3591 (2017).

63. M. R. Gerhardt, L. M. Pant, H.-S. Shiau, and A. Z. Weber, *ECS Trans.*, **86**, 15–24 (2018).

64. S. D. Poynton, R. C. T. Slade, T. J. Omasta, W. E. Mustain, R. Escudero-Cid, P. Ocón, and J. R. Varcoe, *J. Mater. Chem. A*, **2**, 5124–5130 (2014).

65. J. Ponce-Gonzalez, D. K. Whelligan, L. Wang, R. Bance-Soualhi, Y. Wang, Y. Peng, H. Peng, D. C. Apperley, H. N. Sarode, T. P. Pandey, A. G. Divekar, S. Seifert, A. M. Herring, L. Zhuang, and J. R. Varcoe, *Energy Environ. Sci.*, **9**, 3724–3735 (2016).

66. L. Wang, J. J. Brink, Y. Liu, A. M. Herring, J. Ponce-González, D. K. Whelligan, and J. R. Varcoe, *Energy Environ. Sci.*, **10**, 2154–2167 (2017).

67. R. Zeng, S. D. Poynton, J. P. Kizewski, R. C. T. Slade, and J. R. Varcoe, *Electrochem. commun.*, **12**, 823–825 (2010).

68. T. P. Pandey, A. M. Maes, H. N. Sarode, B. D. Peters, S. Lavina, K. Vezzù, Y. Yang,

S. D. Poynton, J. R. Varcoe, S. Seifert, M. W. Liberatore, V. Di Noto, and A. M. Herring, *Phys. Chem. Chem. Phys.*, **17**, 4367–4378 (2015).

69. M. L. Disabb-Miller, Y. Zha, A. J. DeCarlo, M. Pawar, G. N. Tew, and Michael A. Hickner, *Macromolecules*, **46**, 9279–9287 (2013).

70. J. A. Wrubel, A. A. Peracchio, B. N. Cassenti, T. D. Myles, K. N. Grew, and W. K. S. Chiu, *J. Electrochem. Soc.*, **164**, F1063–F1073 (2017).

71. Y. Wang, L. Li, L. Hu, L. Zhuang, J. Lu, and B. Xu, *Electrochem. commun.*, **5**, 662–666 (2003).

72. K. Fukuta, in *AMFC Workshop*, (2011) https://www.energy.gov/sites/prod/files/2014/03/f11/amfc_050811_fukuta.pdf.

73. J. A. Vega, S. Smith, and W. E. Mustain, *J. Electrochem. Soc.*, **158**, B349–B354 (2011).

74. Y. Matsui, M. Saito, A. Tasaka, and M. Inaba, *ECS Trans.*, **25**, 105–110 (2010).

75. T. A. Greszler, T. E. Moylan, and H. A. Gasteiger, in *Handbook of Fuel Cells-Fundenmentals, Technology and Applications*,, vol. 6, p. 729–748 (2009).

76. T. Greszler, T. Moylan, and H. Gasteiger, in *The Electrochemical Society Meeting Abstracts*,, vol. 11, p. 955–955 (2008).

77. B. Kienitz, B. Pivovar, T. Zawodzinski, and F. H. Garzon, *J. Electrochem. Soc.*, **158**, B1175–B1183 (2011).

78. B. Kienitz, thesis, Case Western Reserve University (2009).

79. Y. A. Gomez, A. Oyarce, G. Lindbergh, and C. Lagergren, *J. Electrochem. Soc.*, **165**, F189–F197 (2018).

80. M. Inaba, Y. Matsui, M. Saito, A. Tasaka, K. Fukuta, S. Watanabe, and H. Yanagi, *Electrochemistry*, **5**, 322–325 (2011).

81. H. Yanagi and K. Fukuta, *ECS Trans.*, **16**, 257–262 (2008).

82. W. A. Rigdon, T. J. Omasta, C. Lewis, M. A. Hickner, J. R. Varcoe, J. N. Renner, K. E. Ayers, and W. E. Mustain, *J. Electrochem. Energy Convers. Storage*, **14**, 1–8 (2017).

83. J. X. Wang, F. A. Uribe, T. E. Springer, J. Zhangc, and R. R. Adzic, *Faraday Discuss.*, **140**, 347–362 (2008).

84. H. Xu, Y. Song, H. R. Kunz, and J. M. Fenton, *J. Electrochem. Soc.*, **152**, A1828 (2005).

85. B. Pivovar, D. Ruddy, M. Sturgeon, and H. Long, *FY 2013 Annu. Prog. Rep. DOE Hydrog. Fuel Cells Progr.*, v235–v237 (2013).

86. J. Wang, Y. Zhao, B. P. Setzler, S. Rojas-Carbonell, C. Ben Yehuda, A. Amel, M. Page, L. Wang, K. Hu, L. Shi, S. Gottesfeld, B. Xu, and Y. Yan, *Nat. Energy*, **4**, 392 (2019).

87. J. A. Vega, C. Chartier, and W. E. Mustain, *J. Power Sources*, **195**, 7176–7180 (2010).

88. J. A. Wrubel, A. A. Peracchio, B. N. Cassenti, K. N. Grew, and W. K. S. Chiu, *J. Electrochem. Soc.*, **166**, 810–820 (2019).

89. T. J. Omasta, X. Peng, and W. E. Mustain, in *The Electrochemical Society Meeting Abstracts*,, vol. 30, p. 1754–1754 (2018).

90. B. P. Setzler and Y. Yan, in *The Electrochemical Society Meeting Abstracts*,, vol. 01, p. 1654 (2017).

91. G. Huang, M. Mandal, X. Peng, A. C. Yang-Neyerlin, B. S. Pivovar, W. E. Mustain, P. A. Kohl, J. E. Soc, G. Huang, M. Mandal, X. Peng, A. C. Yang-Neyerlin, B. S. Pivovar, W. E. Mustain, and P. A. Kohl, *J. Electrochem. Soc.*, **166**, F637–F644 (2019).

92. J. Hu, C. Zhang, X. Zhang, L. Chen, L. Jiang, Y. Meng, and X. Wang, *J. Power Sources*, **272**, 211–217 (2014).

93. H. C. Lee, K. L. Liu, L. D. Tsai, J. Y. Lai, and C. Y. Chao, *RSC Adv.*, **4**, 10944 (2014).

94. G. Merle, A. Chairuna, E. Van De Ven, and K. Nijmeijer, *J. Appl. Polym. Sci.*, **129**, 1143–1150 (2013).

95. X. Ren, S. C. Price, A. C. Jackson, N. Pomerantz, and F. L. Beyer, *ACS Appl. Mater. Interfaces*, **6**, 13330–13333 (2014).

96. L. Jheng, S. L. Hsu, B. Lin, and Y. Hsu, *J. Memb. Sci.*, **460**, 160–170 (2014).

97. Z. Li, X. He, Z. Jiang, Y. Yin, B. Zhang, G. He, Z. Tong, H. Wu, and K. Jiao, *Electrochim. Acta*, **240**, 486–494 (2017).

98. X. He, J. Liu, H. Zhu, Y. Zheng, and D. Chen, *RSC Adv.*, **5**, 63215–63225 (2015).

99. X. Lin, M. Gong, Y. Liu, L. Wu, Y. Li, X. Liang, Q. Li, and T. Xu, *J. Memb. Sci.*, **425**–**426**, 190–199 (2013).

100. W. Lu, Z. G. Shao, G. Zhang, Y. Zhao, J. Li, and B. Yi, *Int. J. Hydrogen Energy*, **38**, 9285–9296 (2013).

101. K. H. Lee, D. H. Cho, Y. M. Kim, S. J. Moon, J. G. Seong, D. W. Shin, J.-Y. Sohn, J. F. Kim, and Y. M. Lee, *Energy Environ. Sci.*, **10**, 275–285 (2017).

102. B. P. Tripathi, M. Kumar, and V. K. Shahi, *J. Memb. Sci.*, **360**, 90–101 (2010).

103. L. Wang, X. Peng, W. E. Mustain, and J. R. Varcoe, *Energy Environ. Sci.*, **12**, 1575–1579 (2019).

104. M. Mandal, G. Huang, and P. A. Kohl, *J. Memb. Sci.*, **570**–**571**, 394–402 (2019).

105. W. Chen, M. Mandal, G. Huang, X. Wu, G. He, and P. A. Kohl, *ACS Appl. Energy Mater.*, **2**, 2458–2468 (2019).

106. J. Lamanna, D. S. Hussey, E. Baltic, and D. L. Jacobson, *Rev. Sci. Instrum.*, **88**, 113702 (2017).

107. D. S. Hussey, J. M. Lamanna, E. Baltic, and D. L. Jacobson, *Nucl. Inst. Methods Phys. Res. A*, **866**, 9–12 (2017).

108. D. S. Hussey, D. L. Jacobson, M. Arif, P. R. Huffman, R. E. Williams, and J. C. Cook, *Nucl. Instruments Methods Phys. Res. A*, **542**, 9–15 (2005).

109. Y. Zhou, K. Jiao, Q. Du, Y. Yin, and X. Li, *Int. J. Hydrogen Energy*, **38**, 12891–12903 (2013).

110. W. Lu, Z. G. Shao, G. Zhang, Y. Zhao, and B. Yi, *J. Power Sources*, **248**, 905–914 (2014).

111. M. Liu, Z. Wang, J. Mei, J. Xu, L. Xu, H. Han, H. Ni, and S. Wang, *J. Memb. Sci.*, **505**, 138–147 (2016).

112. Y. Zheng, U. Ash, R. P. Pandey, A. G. Ozioko, J. Ponce-gonzález, M. Handl, T. Weissbach, J. R. Varcoe, S. Holdcroft, W. Matthew, R. Hiesgen, and D. R. Dekel, *Macromolecules*, **51**, 3264–3278 (2018).

113. M. K. Mondal, H. K. Balsora, and P. Varshney, *Energy*, **46**, 431–441 (2012).

114. M. E. Boot-Handfor, J. C. Abanades, E. J. Anthony, M. J. Blunt, S. Brandani, N. Mac Dowell, J. R. Fern´andez, M.-C. Ferrari, R. Gross, J. P. Hallett, R. S. Haszeldine, P. Heptonstall, A. Lyngfelt, Z. Makuch, E. Mangano, R. T. J. Porter, M. Pourkashanian, G. T. Rochelle, N. Shah, et al., *Energy Environ. Sci*, **7**, 130 (2014).

115. K. Li, W. K. Teo, and R. Hughes, *Underw. Technol.*, **20** (1994).

116. K. Li and N. Li, *Sep. Sci. Technol.*, **28**, 1085–1090 (1993).

117. H. W. Pennline, E. J. Granite, D. R. Luebke, J. R. Kitchin, J. Landon, and L. M. Weiland, *Fuel*, **89**, 1307–1314 (2010).

118. J. Landon and J. R. Kitchin, *J. Electrochem. Soc.*, **157**, B1149 (2010).

119. M. Eisaman, D. Schwartz, S. Amic, D. Larner, J. Zesch, F. Torres, and K. Littau, *Tech. Proc. 2009 NSTI Nanotechnol. Conf. Expo, NSTI-Nanotech 2009*, **3** (2009).

120. W. A. Rigdon, T. J. Omasta, C. A. Lewis, and W. E. Mustain, *ECS Trans.*, **69**, 1–9

(2015).

121. H. Xie, Y. Wu, T. Liu, F. Wang, B. Chen, and B. Liang, *Appl. Energy*, **259**, 114119 (2020).

122. A. P. Muroyama, A. Pătru, and L. Gubler, *J. Electrochem. Soc.*, **167**, 133504 (2020).

123. Y. Yan, B. Setzler, Y. Zhao, M. S. R. Carbonell, and S. Gottesfeld, U.S. Patent No. 10,811,711. 20 Oct. 2020.

124. B. P. Setzler, L. Shi, T. Wang, and Y. Yan, in *The Electrochemical Society Meeting Abstracts*,, vol. 34, p. 1824 (2019).

125. S. T. Thompson, D. Peterson, D. Ho, and D. Papageorgopoulos, *J. Electrochem. Soc.*, **167**, 084514 (2020).

126. X. Wu, X. Wang, G. He, and J. Benziger, *J. Polym. Sci. Part B Polym. Phys.*, **49**, 1437–1445 (2011).

127. X. Li, Y. Yu, Q. Liu, and Y. Meng, *Int. J. Hydrogen Energy*, **38**, 11067–11073 (2013).

128. V. Detallante, D. Langevin, C. Chappey, M. Métayer, R. Mercier, and M. Pinéri, *J. Memb. Sci.*, **190**, 227–241 (2001).

129. Y. Katayama, K. Yamauchi, K. Hayashi, T. Okanishi, H. Muroyama, T. Matsui, Y. Kikkawa, T. Negishi, S. Watanabe, T. Isomura, and K. Eguchi, *ACS Appl. Mater. Interfaces*, **9**, 28650−28658 (2017).

130. M. Chen, C. Zhao, F. Sun, J. Fan, H. Li, and H. Wang, *eTransportation*, **5**, 100075 (2020).

131. M. Breitwieser, T. Bayer, A. Büchler, R. Zengerle, S. M. Lyth, and S. Thiele, *J. Power Sources*, **351**, 145–150 (2017).

132. L. Cindrella and A. M. Kannan, *J. Power Sources*, **193**, 447–453 (2009).

133. R. B. Kaspar, M. P. Letterio, J. A. Wittkopf, K. Gong, S. Gu, and Y. Yan, *J. Electrochem. Soc.*, **162**, F483–F488 (2015).

134. A. Carlson, P. Shapturenka, B. Eriksson, G. Lindbergh, C. Lagergren, and R. Wreland Lindström, *Electrochim. Acta*, **277**, 151–160 (2018).

135. G. Zhang and K. Jiao, *J. Power Sources*, **391**, 120–133 (2018).

136. L. Zhang and Z. Shi, *Alexandria Eng. J.*, **60**, 421–433 (2021).

137. M. Sauermoser, N. Kizilova, B. G. Pollet, and S. Kjelstrup, *Front. Energy Res.*, **8**, 1–20 (2020).

138. P. J. Hamilton and B. G. Pollet, *Fuel cells*, **10**, 489–509 (2010).

139. Y. Yoon, W. Lee, G. Park, T. Yang, and C. Kim, *Electrochim. Acta*, **50**, 709–712 (2004).